



HAL
open science

Genetically encoded reporters of actin filament organization in living cells and tissues

Carla Silva Martins, Francois Iv, Shashi Kumar Suman, Thomas Panagiotou, Clara Sidor, Maria Ruso-Lopez, Camille Plancke, Shizue Omi, Maxime Gomes, Alexander Llewellyn, et al.

► **To cite this version:**

Carla Silva Martins, Francois Iv, Shashi Kumar Suman, Thomas Panagiotou, Clara Sidor, et al.. Genetically encoded reporters of actin filament organization in living cells and tissues. 2024. hal-04563732

HAL Id: hal-04563732

<https://cnrs.hal.science/hal-04563732>

Preprint submitted on 30 Apr 2024

HAL is a multi-disciplinary open access archive for the deposit and dissemination of scientific research documents, whether they are published or not. The documents may come from teaching and research institutions in France or abroad, or from public or private research centers.

L'archive ouverte pluridisciplinaire **HAL**, est destinée au dépôt et à la diffusion de documents scientifiques de niveau recherche, publiés ou non, émanant des établissements d'enseignement et de recherche français ou étrangers, des laboratoires publics ou privés.

Genetically encoded reporters of actin filament organization in living cells and tissues

Carla Silva Martins^{1,11}, François Iv^{1,11}, Shashi Kumar Suman², Thomas C. Panagiotou³, Clara Sidor⁴, María Ruso-López⁵, Camille N. Plancke², Shizue Omi¹, Maxime Gomes¹, Alexander Llewellyn¹, Sourish Reddy Bandi¹, Laurie Ramond¹, Federica Arbizzani⁶, Caio Vaz Rimoli¹, Frank Schnorrer⁴, François Robin², Andrew Wilde^{3,7}, Loïc LeGoff¹, Jean-Denis Pedelacq⁸, Stéphanie Cabantous⁹, Sergio A. Rincon⁵, Cristel Chandre¹⁰, Sophie Brasselet^{1,*}, Manos Mavrikis^{1,12,*}

¹Institut Fresnel, CNRS UMR7249, Aix Marseille Univ, Centrale Med, 13013 Marseille, France

²Sorbonne Université, CNRS, Institut de Biologie Paris Seine, Laboratoire de Biologie du Développement/UMR7622, 75005 Paris, France

³Department of Molecular Genetics, University of Toronto, Toronto, ON M5S 1M1, Canada

⁴Aix Marseille Univ, CNRS, IBDM, Turing Centre for Living Systems, 13009 Marseille, France

⁵Instituto de Biología Funcional y Genómica and Departamento de Microbiología y Genética, Consejo Superior de Investigaciones Científicas (CSIC) / Universidad de Salamanca, Salamanca 37007, Spain

⁶Institut Curie, PSL University, CNRS UMR 144, 75005 Paris, France

⁷Department of Biochemistry, University of Toronto, Toronto, ON M5S 1M1, Canada

⁸Institut de Pharmacologie et de Biologie Structurale, IPBS, Université de Toulouse, CNRS, UPS, 31077 Toulouse, France

⁹Centre de Recherche en Cancérologie de Toulouse (CRCT), Inserm, Université Paul Sabatier-Toulouse III, CNRS, 31037 Toulouse, France

¹⁰CNRS, Aix Marseille Univ, I2M, Marseille 13009, France

¹¹These authors contributed equally

¹²Lead contact

*Correspondence: sophie.brasselet@fresnel.fr (S.B.), manos.mavrikis@fresnel.fr (M.M.)

SUMMARY

The cytoskeletal protein actin is crucial for cell shape and integrity throughout eukaryotes. Actin filaments perform essential biological functions, including muscle contraction, cell division and tissue morphogenesis. These diverse activities are achieved through the ability of actin filaments to be arranged into diverse architectures, but a detailed appreciation of the dynamic organizational state of the actin filaments has been hindered by available tools. Fluorescence polarization microscopy is uniquely placed for measuring actin organization by exploiting the sensitivity of polarized light excitation to the orientation of fluorophores attached to actin filaments. By engineering constrained fluorescent protein fusions to widely used actin localization reporters, we have succeeded in developing novel genetically-encoded reporters for non-invasive, quantitative measurements of actin filament organization in living cells by fluorescence polarization microscopy. We show examples of actin organization measurements in living mammalian cells in culture, as well as *in vivo* in fission yeast, *C. elegans* and *Drosophila*.

KEYWORDS

actin filaments, molecular organization, molecular order, molecular orientation, filament alignment, fluorescence polarization microscopy, morphogenesis, GFP mobility

55 INTRODUCTION

56
57 Actin is one of the most abundant and conserved proteins throughout eukaryotes,
58 including structural homologs in bacteria. Actin monomers polymerize through non-
59 covalent association to generate filaments. These filaments perform a wide range of
60 essential biological functions, such as muscle contraction, cell division, cell adhesion, cell
61 motility, tissue morphogenesis and intracellular pathogen movement (Pollard and
62 Cooper, 2009). These various activities are achieved through dozens of actin binding
63 proteins which configure actin into a diverse set of organization states (Pollard, 2016).
64 The precise geometrical organization of actin filament assemblies, i.e. how actin filaments
65 are physically oriented in space and to what extent they are aligned to each other
66 (collectively referred to as filament *organization*, hereafter), is crucial to biological function
67 (Blanchoin et al., 2014; Fletcher and Mullins, 2010; Heisenberg and Bellaiche, 2013;
68 Lappalainen et al., 2022; Paluch and Heisenberg, 2009). Typically, multiple actin-binding
69 proteins populate actin filament (F-actin) assemblies in cells, and predicting actin filament
70 organization and its effect on function remains elusive.

71 Much progress has been made in defining the proteome of the actin cytoskeleton
72 and their dynamics, but a detailed appreciation of the dynamic organizational state of the
73 actin filaments themselves has been hindered by available tools. Cryo-electron
74 tomography emerges as a very powerful method to visualize the nanoscale organization
75 of actin filaments in cells (Chakraborty et al., 2020), but it is not applicable to living
76 samples. The most widely used approach for imaging actin filaments in living cells uses
77 fluorescence microscopy and either one of the following three actin filament-binding
78 probes: (1) small (~1 kDa) organic fluorescent dye conjugates of the F-actin-binding drugs
79 phalloidin (Barak et al., 1980; Wulf et al., 1979) and jasplakinolide (Lukinavicius et al.,
80 2014); such examples are AlexaFluor488 (AF488)-phalloidin and silicon rhodamine (SiR)-
81 jasplakinolide, the latter known with the misleading name "SiR-actin", (2) GFP fusions to
82 G-actin (Ballestrem et al., 1998; Choidas et al., 1998; Doyle and Botstein, 1996;
83 Verkhusha et al., 1999; Westphal et al., 1997), and (3) GFP fusions to actin-binding
84 peptides or protein domains (for example, the actin-binding domain of moesin (Edwards
85 et al., 1997)). The intensity and distribution of the fluorescent pixels in the images inform
86 us on the relative localization and levels of filamentous actin within the cell. However, how
87 actin filaments are organized at a given image pixel, within the optical resolution of the
88 microscope (typically ~200 nm), cannot be deduced from the fluorescence intensity alone,
89 nor from the pattern of fluorescent pixel distribution. Quantitative imaging tools that enable
90 real-time measurements of filament organization are currently limiting.

91 Fluorescence polarization microscopy (hereafter, polarimetry) is ideally placed for
92 measuring actin filament organization in living cells by exploiting the sensitivity of
93 polarized light excitation to the orientation of fluorophores attached to actin filaments.
94 Fluorescence is maximized when polarized light is aligned with the excitation dipoles of
95 the fluorophores (Forkey et al., 2000). Thus, an ensemble of fluorophores will be excited
96 more efficiently in preferred directions depending on the organization of the fluorophores.
97 By measuring the modulation of fluorescence induced by the rotation of light polarization
98 in the sample plane, we can extract independently two angles per image pixel: the mean
99 orientation of the fluorophores within the focal volume (Figure 1A, angle ρ , ρ) and the
100 in-plane projection of the angle explored by these fluorophores, (Figure 1A, angle ψ , ψ)
101 (Brasselet et al., 2013). If the fluorophores are linked to actin filaments in a constrained
102 manner, the measured parameters reflect directly the molecular-scale organization of the
103 labeled filaments in living cells at each pixel location, with ρ their mean orientation, and
104 ψ their degree of alignment; the higher the filament alignment, the lower the ψ (see
105 methods for details).

106 Fluorophore conjugates to phalloidin and jasplakinolide have been used
107 successfully for polarimetry in fixed cells (Juanes et al., 2019; Loison et al., 2018;

108 Mavrakis et al., 2014; Spira et al., 2017; Swaminathan et al., 2017). However, their use
109 in living cells is far from ideal given that these drugs stabilize actin filaments (Bubb et al.,
110 1994; Cramer, 1999; Dancker et al., 1975; Wieland, 1977). Introducing these drugs into
111 tissues is also experimentally challenging, while controlling their intracellular
112 concentration spatiotemporally is practically impossible, rendering their use in living
113 tissues very limited. The goal of our study is to extend the potential of polarimetry to living
114 cells and tissues by generating minimally perturbative, genetically-encoded, fluorescent
115 protein-based reporters for live-cell measurements of actin filament organization. To this
116 end, we tailor GFP fusions to widely used F-actin localization reporters by constraining
117 the mobility of the GFP in order to render them usable for organization measurements by
118 polarimetry. We use stress fibers in cultured mammalian cells as a model system of
119 known F-actin organization to identify constrained GFP fusions that report faithfully the
120 orientation and alignment of actin filaments in live cells. We further validate the
121 functionality and use of the novel reporters in three genetically tractable *in vivo* model
122 systems, the fission yeast *Schizosaccharomyces pombe*, the nematode *Caenorhabditis*
123 *elegans* and the fruit fly *Drosophila melanogaster*.

124 125 RESULTS

126 127 **Widely used genetically encoded actin localization reporters are not suitable for** 128 **organization measurements with polarimetry.**

129
130 For the sake of illustrating how we display and interpret polarimetry measurements in
131 cells throughout our study, Figure 1B shows an example of polarimetry in fixed
132 mammalian cells stained with AF488-phalloidin or SiR-jasplakinolide. We focus on the
133 analysis of pixels containing stress fibers (SFs), which electron microscopy (EM) has
134 shown to form bundles of actin filaments highly parallel to each other (Heuser and
135 Kirschner, 1980; Svitkina et al., 1995). The angles ρ and ψ are represented as orientation
136 and organization maps, respectively. The distribution of ψ angles for multiple SFs in tens
137 of cells is shown in Figure 1C. The analysis reveals three key findings. First, AF488 and
138 SiR fluorophore dipoles are, on the average, parallel and perpendicular to actin filaments,
139 respectively, in line with previous reports (Juanes et al., 2019; Loison et al., 2018;
140 Mavrakis et al., 2014; Mehta et al., 2016; Rimoli et al., 2022; Swaminathan et al., 2017;
141 Valades Cruz et al., 2016). Second, actin filaments are oriented along the axis of the SFs:
142 SFs oriented differently in the cell show distinct ρ stick colors according to their precise
143 orientation, allowing for an easy visual tracking of changes in mean filament orientation
144 (Figure 1B). Third, actin filaments within SFs are highly aligned. Single AF488
145 fluorophores wobble by $\sim 90\text{-}100^\circ$ with a tilt angle of $\sim 20^\circ$ off the actin filament axis (Rimoli
146 et al., 2022; Valades Cruz et al., 2016) thus measured ψ of $\sim 120\text{-}130^\circ$ (Figure 1C and
147 1D,iii) reflect that the contained filaments at the image pixels of SFs are highly parallel to
148 each other. The visual inspection of the color-coded ψ maps reveals that all SFs share
149 very similar filament organization despite their different orientations (Figure 1B). Given
150 the precision of only a few degrees for ρ and ψ angle measurements (Kress et al., 2013),
151 the very narrow distribution of ρ and ψ angles within a region of interest in a given SF (for
152 example, standard deviation= $3\text{-}5^\circ$ for ROI5 of AF488, Figure 1B) further reveals a very
153 homogeneous population of orientations and aperture angles explored at an image pixel,
154 in full line with what one expects from EM. This analysis showcases the potential of
155 polarimetry for organization measurements in cells: even though one cannot resolve
156 individual filaments, their molecular-scale organization at a given image pixel is
157 detectable and can be quantified as shown. This said, the reason why such
158 measurements are possible in these examples is because AF488 and SiR are sufficiently
159 constrained in their conjugates with phalloidin and jasplakinolide, respectively.

160 To assess the usability of available genetically-encoded F-actin localization
161 reporters for organization measurements in living cells using polarimetry, we measured
162 actin filament orientation and alignment on stress fibers (SFs) of live U2OS cells
163 expressing either of five widely used F-actin-binding EGFP fusions: the F-actin binding
164 peptides Lifeact (Riedl et al., 2008) and F-tractin9-52 (Johnson and Schell, 2009), the
165 actin-binding domain of human Utrophin Utr1-261 (Burkel et al., 2007), the synthetic actin-
166 binding Affimer, Affimer6 (Lopata et al., 2018), and human non-muscle beta G-actin
167 (Ballestrem et al., 1998). The measured ψ angles on SFs were very high ($>160^\circ$) in all
168 cases (Figure 1E). Given that actin filaments in stress fibers are highly aligned to each
169 other, the high ψ values cannot result from disordered actin filaments, but they rather
170 reflect the high rotational mobility of EGFP in the respective fusions (Figure 1D,i),
171 rendering the latter not suitable for organization measurements.

172

173 **Design of GFP-based reporters with constrained GFP mobility**

174

175 Tailoring the available F-actin localization reporters for organization measurements
176 requires that GFP mobility is constrained. We reasoned that there are three main sources
177 that contribute to the flexibility of the EGFP. The first source is the presence of an amino
178 acid linker between the actin-binding moiety (ABD) and the fused EGFP. All the widely
179 used EGFP fusions tested above have been generated by standard restriction-ligation
180 cloning using the multiple cloning sites of the EGFP-C1 and EGFP-N1 vectors from
181 Clontech (Zhang et al., 1996) and thus inevitably introducing several amino acid residues
182 in between the EGFP terminus and the ABD. Although the presence of such a linker is
183 reasonably assumed to be important for minimizing interference with protein folding and
184 interactions with actin-binding proteins, we hypothesized that it also contributes to the
185 rotational mobility of the fused EGFP. The second source is the flexibility of the terminus
186 of the ABD to which EGFP is fused. Thus, shortening or removing altogether the linker
187 and/or flexible stretches from the terminus of the ABD could be promising approaches for
188 constraining the GFP, assuming that protein folding, F-actin binding and interactions with
189 actin-binding partners are not compromised.

190 The third source of flexibility are the N- and C-termini of EGFP themselves. The
191 crystal structures of GFP (Ormo et al., 1996; Yang et al., 1996), EGFP (Royant and
192 Noirclerc-Savoie, 2011) and practically all fluorescent protein (FP) variants with the same
193 termini show that the C-terminus after the end of the β_{11} strand comprises 11 residues
194 that are unstructured and most of which are absent from the respective crystal structures
195 due to their flexibility (Figure 1F,G). The N-terminal stretch preceding the β_1 strand
196 comprises 12 residues, with residues 5-9 forming a 3_{10} helix (in red in Figure 1F,G), while
197 the first 4 amino acid residues are similarly unstructured and often not visible in the crystal
198 structures. Shortening of the N-terminus by 4-6 residues has indeed been shown to
199 constrain the mobility of GFPS65T and EGFP in C-terminal fusions to septins and
200 nucleoporins (DeMay et al., 2011a; Kampmann et al., 2011; Vrabioiu and Mitchison,
201 2006). However, more extensive truncation of the termini has not been explored to date.
202 This is probably due to early studies with wild-type GFP, GFPS65T or EGFP that showed
203 that removing more than six N-terminal or more than nine C-terminal residues significantly
204 impairs or abolishes GFP fluorescence altogether (Dopf and Horiagon, 1996; Kim and
205 Kaang, 1998; Li et al., 1997).

206 Prompted by the recent finding that better-folded variants of GFP tolerate more
207 extensive terminal truncations (Raghunathan et al., 2012), we made a side-by-side
208 comparison of truncation mutants of EGFP and the exceptionally stable superfolder GFP
209 (sfGFP) (Pedelacq et al., 2006) to determine to what extent we can shorten their termini
210 without compromising fluorescence. To this end, we expressed truncation mutants in
211 U2OS cells and assessed their fluorescence both by fluorescence-activated cell sorting
212 (FACS) and by spinning disk confocal fluorescence microscopy imaging. Both FACS and

213 imaging confirmed the sensitivity of EGFP to terminal truncations, and showed, at the
214 same time, that sfGFP missing either the entire N- (Δ N12) or C- terminus (Δ C11), or both
215 N- and C-termini (Δ N12 Δ C11), retains its fluorescence and is usable for fluorescence
216 imaging (Figure 1G,H).

217 We hypothesized that engaging both GFP termini could also constrain GFP
218 mobility. Intramolecular GFP fusions, with GFP placed within a protein structure, for
219 example within a loop, or between a transmembrane and extracellular domain, could
220 reduce its rotational mobility. Such constructs have notably been used to constrain GFP
221 mobility in fusions with the integral membrane proteins integrin (Swaminathan et al.,
222 2017) and the major histocompatibility complex class I (MHC I) protein (Kress et al.,
223 2011). Alternatively, circularly permuted GFP (cpGFP) (Akemann et al., 2001; Baird et
224 al., 1999; Topell et al., 1999) with the original termini connected via an ABD (Figure 1J)
225 could also act to constrain GFP mobility. Given that better-folded variants of GFP also
226 behave much better in intramolecular fusions in terms of functionality (Bendezu et al.,
227 2015; Osawa and Erickson, 2005) and that they can be beneficial for the folding and
228 stability of circular permutants (Carlson et al., 2010), we considered the use of sfGFP as
229 the best choice for GFP fusion engineering. To suppress GFP dimerization-related
230 artifacts, we further introduced the V206K mutation to generated monomeric sfGFP
231 (msfGFP) (Costantini et al., 2012; Cranfill et al., 2016; Zacharias et al., 2002) which we
232 used for all subsequent screening (Figure 1I).

233 Besides the use of full-length msfGFP for fusions with ABDs, we employed two
234 additional approaches for intramolecular G-actin fusions. Instead of the full-length GFP,
235 we used the 16-residue GFP fragment, β 11, that we complemented with co-expressed
236 GFP1-10 in a bipartite split-GFP complementation assay-like manner (Cabantous et al.,
237 2005) (Figure 1K). We finally employed the tetracysteine-biarsenical system, which uses
238 among the smallest genetically encoded tags for fluorescent labeling and which
239 resembles conceptually the bifunctional rhodamine approach (Figure 1K). To this end, we
240 genetically fused a short peptide sequence containing 4 cysteines to G-actin. Upon
241 addition of the membrane-permeable, nonfluorescent biarsenical dye FIAsH (fluorescein
242 arsenical hairpin binder) and its specific binding to the tetracysteine motif, the dye
243 becomes fluorescent *in situ* in live cells (Griffin et al., 1998; Martin et al., 2005). Both the
244 increased functionality due to the small size of the genetic tag (Andresen et al., 2004) and
245 the rigidity of the peptide-fluorophore complex suggested by nuclear magnetic resonance
246 (NMR) (Madani et al., 2009) prompted us to generate such fusions for G-actin. Terminal
247 and intramolecular fusions of G-actin with this approach have been successfully used to
248 visualize F-actin in mammalian and fission yeast cells (Chen et al., 2012; Martin et al.,
249 2005).

250 Taking together the above-mentioned points, we embarked on a screen of ABD-
251 GFP fusions using the widely used ABDs tested earlier, namely Lifeact, Utrophin Utr1-
252 261, F-tractin9-52, Affimer6, and human non-muscle beta G-actin. To constrain GFP
253 mobility, we generated terminal, intramolecular and circularly permuted GFP fusions
254 without linker sequences, with shortened GFP termini and shortened termini of the ABD.
255 We expressed fusions transiently in U2OS cells and made polarimetry measurements on
256 SFs, using the latter as a model structure of known actin filament organization. Given that
257 SFs comprise highly aligned actin filaments and if GFP mobility is sufficiently constrained,
258 we expect to measure mean fluorophore dipole orientations (ρ angle values) that are
259 either parallel or perpendicular to the SF axis. The smaller the measured ψ angles are on
260 SFs, the more constrained will be the GFP mobility of the respective fusion and thus the
261 larger the range of changes in F-actin organization that we will be able to detect. With the
262 intention to provide a rational for constraining GFP mobility, we chose to show and
263 discuss the results of all constructs and not only the ones with constrained GFP mobility.
264

265 **Engineering actin filament organization reporters using Lifeact.**

266
267 The N-terminal 17 amino acids of the budding yeast actin-binding protein Abp140 are
268 known as the actin-binding peptide "Lifeact" (Riedl et al., 2008) and are used widely for
269 labeling F-actin in live cells. The original reporter used a C-terminal EGFP (Riedl et al.,
270 2008) but N-terminal EGFP fusions have also been used successfully (Courtemanche et
271 al., 2016). To constrain GFP mobility in fusions with Lifeact, we generated C-terminal
272 fusions (Figure 2A, L1 to L37), N-terminal fusions (Figure 2A, L38 to L53), as well as
273 circular permutants with Lifeact connecting the original N- and C-termini (Figure 2A, L54
274 to L72). To remove flexible stretches, we did not include linkers in the fusions, and we
275 further shortened the N- or/and the C-termini of GFP. At the onset of this study, the crystal
276 structure of Lifeact bound to F-actin (Figure S1C,D and (Belyy et al., 2020; Kumari et al.,
277 2020) was not yet known. Circular dichroism and NMR spectroscopies had suggested
278 that Lifeact forms a helix between residues 2 and 10 (Riedl et al., 2008), though a helix
279 from position 3 to 17, i.e. essentially encompassing the entire Lifeact sequence, was most
280 commonly found with the secondary structure prediction server Robetta (predictions not
281 shown). These findings, the fact that the very C-terminus of Lifeact was not reported to
282 be conserved in fungi (Riedl et al., 2008), and our quest for the minimal actin-binding
283 stretch of Lifeact, prompted us to also shorten Lifeact on either or both its termini, aiming
284 at removing flexible stretches that are not essential for actin binding.

285 We screened the generated fusions with respect to their fluorescent levels, their
286 capacity to bind F-actin, their localization, and the extent to which GFP is constrained
287 based on polarimetry measurements (Figures 2A and S1A). Extensive shortening of the
288 msfGFP termini did not affect fluorescence of terminal fusions, in line with the results of
289 our truncation screen. The fluorescence of cpGFP fusions, on the other hand, was
290 expected to depend on the length and composition of the linker connecting the original
291 termini. Earlier studies suggested that linkers comprising at least 20 residues are needed
292 to connect the GFP barrel ends, i.e. in between the end of β 11 and the beginning of β 1
293 strands, to allow for stable cpGFP folding and fluorescence, and this using flexible
294 glycine-rich linkers (Akemann et al., 2001; Baird et al., 1999; Topell et al., 1999). Not
295 surprisingly, fluorescence was severely compromised or absent for cpGFP fusions when
296 using 11-16 residue-linkers.

297 The capacity of the fusions to bind F-actin, using SF labeling as a readout,
298 depended, as expected, on the length of Lifeact. Shortening of Lifeact on either or both
299 termini when fused to full-length msfGFP showed that (a) Val3 is essential for binding F-
300 actin, (b) Gly2 is not needed *per se* for binding F-actin but that it contributes to the latter,
301 and (c) the six C-terminal residues are also not essential for F-actin binding; these
302 residues are also the least conserved ones among fungi (Figures 2A and S1B-G).
303 Importantly, the proximity of either terminus of Lifeact to the terminus of GFP, notably
304 when combining shortened Lifeact with shortened GFP termini, was critical for F-actin
305 binding. This was particularly evident in cpGFP fusions with shortened GFP termini,
306 whereby F-actin binding was compromised despite the presence of full-length Lifeact,
307 suggesting that a minimum of flexibility is required on either side of the actin-binding
308 moiety to allow for F-actin binding. This latter effect proved eventually to be the bottleneck
309 for constraining efficiently GFP in cpGFP fusions given that even moderate shortening of
310 the GFP termini compromised F-actin binding.

311 Under our low-level expression conditions (see methods for promoter details), all
312 fusions labeled all types of SFs, notably dorsal, ventral, peripheral, perinuclear actin cap
313 and arc SFs, including focal adhesions (FAs), as well as mitochondrial actin (Figure S1H).
314 To exclude that the additional localization of fusions to arc nodes reflected GFP
315 dimerization-related artifacts (Figure S1I), we compared fusions bearing one, two or all
316 three GFP monomerizing mutations (Figure 1I); they all localized to arc nodes excluding
317 such a scenario.

318 Terminal GFP fusions proved to be the most efficient way to constrain GFP mobility
319 (Figures 2A-C and S1A). Polarimetry measurements showed that removing only the linker
320 between full-length Lifeact and full-length GFP did not have any effect on GFP mobility
321 (Figures 2A and S1A). The additional removal of seven residues from the N-terminus of
322 GFP or ten residues from its C-terminus, was necessary to start constraining its mobility.
323 Combining shorter GFP termini with shorter Lifeact termini also proved determinant,
324 notably in N-terminal Lifeact fusions whereby the removal of a single residue, Gly2, from
325 Lifeact, reduced ψ angle values by several tens of degrees (compare L42 with L45 in
326 Figure 2A,C). Altogether, polarimetry measurements showed that we succeeded to
327 immobilize GFP both in N- and C-terminal fusions with Lifeact. We chose to focus on
328 fusions L22 (Lifeact Δ C4-msfGFP Δ N7) and L45 (msfGFP Δ C9-Lifeact Δ N2) as the best
329 performing reporters for further functional characterization and F-actin organization
330 measurements in live cells and tissues.

331 332 **Engineering actin filament organization reporters using the Utrophin Calponin** 333 **Homology Domain.**

334
335 The N-terminal 261 amino acids of human utrophin contain an F-actin-binding calponin
336 homology domain known as Utr-CH or Utr261 (Burkel et al., 2007), which is widely used
337 for visualizing F-actin in live cells and tissues. The original GFP fusion is N-terminal to
338 the Utr-CH domain (Burkel et al., 2007) but C-terminal EGFP fusions have also been
339 used successfully (Belin et al., 2014). To constrain GFP mobility in fusions with Utr261,
340 we generated N-terminal fusions (Figure S2A, U1 to U24), C-terminal fusions (Figure
341 S2A, U25 to U42), as well as circular permutants with Utr261 connecting the original N-
342 and C-termini (Figure S2A, U43 to U63). We did not include linkers in the fusions, and we
343 further shortened the N- or/and the C-termini of GFP. The structure of the utrophin
344 calponin homology domain bound to F-actin (Kumari et al., 2020) was not available at the
345 time of the beginning of this study, but the biochemical and structural data concerning the
346 N-terminal residues 28-261 of human utrophin (Keep et al., 1999; Moores and Kendrick-
347 Jones, 2000) provided already key insights. Although the N-terminal 27 residues of
348 utrophin maximize its affinity for F-actin, they are dispensable for F-actin binding (Moores
349 and Kendrick-Jones, 2000). The susceptibility of these same residues to degradation
350 further suggested that they are not part of a compact structure and might be inherently
351 flexible (Moores and Kendrick-Jones, 2000). This observation aligns with their partial
352 disorder in their complex with F-actin (Kumari et al., 2020). A truncation mutant of Utr261,
353 Utr230-EN (Belin et al., 2013), was also shown to bind cytoplasmic actin filaments. These
354 findings prompted us to also shorten Utr261 on either or both termini.

355 We screened the generated utrophin fusions along the same lines as for the Lifeact
356 fusions (Figures S2B-G). All constructs were fluorescent except the three cpGFP fusions
357 with the shortest N- and C-termini of GFP, suggesting again that a minimum of flexibility
358 is needed to allow connecting the original N- and C-termini of GFP while binding to F-
359 actin. Shortening of Utr261 on either or both termini in terminal fusions with full-length
360 msfGFP confirmed that the N-terminal 27 residues of Utr261 are indeed dispensable for
361 binding F-actin, and further showed that the C-terminal 31 or 39 residues are also not
362 required for binding F-actin (Figures S2A-G). Importantly, the proximity of residues 29-32
363 in the N-terminal helix of Utr261 to the C-terminus of GFP, notably when combining
364 shortened Utr261 with shortened GFP termini, was critical for F-actin binding (Figures
365 S2A and S2E), in line with the structure of the UtrCH-F-actin complex (Kumari et al.,
366 2020). The localization of all fusions was similar to the one of Lifeact fusions (Figure S2C-
367 F).

368 Terminal GFP fusions proved to be the most efficient way to constrain GFP mobility
369 (Figures 3A-C and S2A,B). As expected from the results of the Lifeact fusions, removing
370 only the linker between full-length Utr261 and full-length GFP did not have any effect on

371 GFP mobility. The additional removal of nine residues from the N-terminus of GFP and of
372 the N-terminal 27 residues of Utr261 were necessary to start constraining its mobility. It
373 is noteworthy that the additional removal of a tenth residue from the GFP C-terminus was
374 sufficient to reduce ψ angle values by several tens of degrees (compare U13 with U20 in
375 Figure 3A,B). Interestingly, all C-terminal GFP fusions, including combinations of the
376 shortest C-terminus of Utr261 and the shortest N-terminus of GFP, and the recently
377 reported construct UG7 (Nakai et al., 2019), were flexible, reflecting most likely inherent
378 flexibility in the very C-terminus of Utr261. We decided to focus on fusion U20
379 (msfGFP Δ C10-Utr28-222) as the best performing reporter for further functional
380 characterization and F-actin organization measurements in live cells and tissues.

381

382 **Engineering actin filament organization reporters using F-tractin.**

383

384 The N-terminal residues 9-52 of the rat enzyme inositol triphosphate 3-kinase A (ITPKA),
385 also known as F-tractin-P (P for prototype), were shown to contain an F-actin-binding
386 domain, a C-terminal GFP fusion of which is widely used as a reporter of F-actin
387 localization in live cells (Johnson and Schell, 2009; Yi et al., 2012) (Figure 3D and S3A).
388 A slightly shorter peptide, N9-40, has been shown to retain F-actin binding, was given the
389 name F-tractin (Yi et al., 2012), and is used interchangeably with F-tractin-P for visualizing
390 F-actin in live cells (John Hammer, National Institutes of Health, Bethesda, MD, USA,
391 personal correspondence). To constrain GFP mobility in fusions with F-tractin and F-
392 tractin-P, we generated C-terminal fusions (Figure S3C, F1 to F22), N-terminal fusions
393 (Figure S3C, F23 to F27), as well as circular permutants with the F-tractin peptide
394 connecting the original N- and C-termini (Figure S3C, F28 to F33). We did not include
395 linkers in the fusions, and we further shortened the N- or/and the C-termini of GFP. The
396 structure of F-tractin or F-tractin-P, alone or in complex with F-actin, has not been solved
397 to date. Secondary structure prediction of F-tractin-P using the program JPred3 in the
398 original article suggested that F-actin binding resides in a putative α -helix comprising
399 residues ~30-40 (Johnson and Schell, 2009). Secondary structure prediction using
400 multiple programs, including JPred4, PHD, Phyre2, RaptorX and AlphaFold, suggests
401 that the glycine- and proline-rich N-terminal ~30 residues are unstructured, with residues
402 ~30-50 predicted to form a helix (Figure S3B). These predictions prompted us to also
403 shorten F-tractin on either of its termini.

404 We screened the generated F-tractin fusions similarly to the Lifeact and utrophin
405 fusions (Figures S3C-E). Unlike the previous screens, all constructs were now
406 fluorescent, including cpGFP fusions with the shortest N- and C-termini of GFP, reflecting
407 most likely the fact that the N-terminus of F-tractin is unstructured and does not bind F-
408 actin thus imposing less constraints for connecting the original termini of cpGFP.
409 Shortening of F-tractin and combinations thereof with shortened GFP termini showed (a)
410 that the N-terminal residues 9-14 are dispensable for F-actin binding and (b) that residues
411 37-40 are critical for F-actin binding (Figure S3C and S3E). All fusions localized similarly
412 to Lifeact and utrophin fusions (Figure S3E).

413 C-terminal GFP fusions of F-tractin proved to be the most efficient way to constrain
414 GFP mobility (Figures 3D-F and S3C,D). The additional removal of seven residues from
415 the N-terminus of GFP was necessary to constrain its mobility. In line with our results
416 from the Lifeact and utrophin screens, it was very striking that the additional removal of a
417 single residue from the C-terminus of F-tractin was sufficient to reduce ψ angle values by
418 several tens of degrees (compare F5 with F11 in Figure 3D,E). Interestingly, all C-terminal
419 GFP fusions of F-tractin-P, including combinations with the shortest N-termini of GFP,
420 were flexible; we observed the same behavior for all N-terminal fusions of F-tractin,
421 including combinations with the shortest C-termini of GFP. We interpret both observations
422 as reflecting the inherent flexibility of the respective F-tractin termini. The fusion F11 (F-

423 tractinN9-39-msfGFP Δ N7) turned out to be the best performing reporter for F-actin
424 organization measurements in live cells.

425

426 **Engineering actin filament organization reporters using Affimer6.**

427

428 Affimers, originally named Adhirons (Tiede et al., 2014), are synthetic, non-antibody-
429 based protein binders that can be engineered to bind specific proteins of interest with
430 high affinity and specificity. Among the recently developed Affimers is the F-actin-binding
431 Affimer, Affimer6 (Lopata et al., 2018), an N-terminal GFP fusion of which can be used to
432 monitor F-actin localization in live cells. To constrain GFP mobility in fusions with
433 Affimer6, we generated C-terminal fusions (Figure S3F, Af1 to Af11), N-terminal fusions
434 (Figure S3F, Af12 to Af16), as well as circular permutants with the Affimer scaffold
435 connecting the original N- and C-termini (Figure S3F, Af17 to Af25). We did not include
436 linkers in the fusions, and we further shortened the N- or/and the C-termini of GFP. The
437 structure of the Affimer scaffold revealed a very compact fold, with hardly any flexible
438 unstructured residues at its termini (Tiede et al., 2014) (Figure S3I). Thus, we only
439 attempted to shorten its C-terminus to remove potentially flexible residues that could
440 contribute to GFP mobility in C-terminal GFP fusions. F-actin binding is not expected to
441 be affected since the actin-binding loops are far from the C-terminus (Tiede et al., 2014).

442 We screened the generated Affimer6 fusions in a similar manner to the other ABD
443 fusions (Figure S3F-I). All constructs were fluorescent apart from the three cpGFP fusions
444 with the shortest N- and C-termini of GFP: the highly compact structure of the Affimer
445 scaffold does most likely not provide the flexibility needed to connect the original N- and
446 C-termini of GFP in these cpGFP fusions. F-actin binding was compromised only for
447 shortened Affimer C-termini combined with highly shortened GFP termini; it is possible
448 that the GFP in these fusions adopts a position that interferes with the actin-binding loops.
449 All Affimer6 fusions localized in an indistinguishable manner from the other ABD fusions
450 (Figure S3H).

451 Fusing full-length Affimer6 C-terminally to the shortest N-terminus of GFP proved
452 to be the most efficient way to constrain GFP mobility (Figures 3G-I and S3F,G). It was
453 again remarkable that the presence of an additional single residue at the N-terminus of
454 GFP was sufficient to increase ψ angle values by several tens of degrees (compare Af6
455 with Af7 in Figure S3F,G). N-terminal GFP fusions of Affimer6 with C-terminally truncated
456 GFP also constrained GFP mobility, but much less efficiently, as was the recently
457 reported Affimer6-based construct POLArISact (Sugizaki et al., 2021). We decided to use
458 fusion Af7 (Affimer6-msfGFP Δ N12) as the best performing reporter for further functional
459 characterization and F-actin organization measurements in live cells and tissues. The ψ
460 values we obtained with this reporter are the lowest ones among all reporters, reflecting
461 a highly constrained GFP, and making it the most sensitive one for detecting small
462 changes in actin filament organization.

463

464 **Engineering red FP-based actin filament organization reporters.**

465

466 Having succeeded to generate GFP-based reporters for the different ABDs, we naturally
467 embarked on the making of the red FP fusion counterparts. The fact that robustly folding
468 GFPs tolerate much more extensive terminal truncations without losing fluorescence
469 (Figure 1G,H) prompted us to undertake a similar approach. Thus, we compared side by
470 side the sensitivity of the widely used red FP, mApple (Cranfill et al., 2016; Shaner et al.,
471 2008), and of superfolder Cherry 2 (sfCherry2) (Feng et al., 2017) to terminal truncations.
472 Both FACS and imaging corroborated our results with green FPs: whereas mApple is
473 sensitive to N-terminal truncations, sfCherry2 tolerates missing its entire N- (Δ N12) or C-
474 terminus (Δ C4) (Figure S4A,B), making the latter the best choice for constraining mobility
475 in its fusions to actin-binding domains.

476 We decided to generate selectively sfCherry2-based terminal fusions for Lifeact
477 and Affimer6. The length and composition of the termini of sfCherry2 are not the same as
478 for GFP necessitating a minimum of screening, but the results from our previous screens
479 helped narrow down our efforts to a limited set of constructs. F-actin binding was, as
480 expected, impaired by the proximity of shortened FP termini to shortened Lifeact. Indeed,
481 the best performing constructs were the ones combining full-length Affimer6 and Lifeact
482 with the most extensively truncated sfCherry2 termini (Figure 3J,K), very similarly to the
483 respective best performing GFP-based ones. The fusions Af30 (Affimer6-sfCherry2 Δ N12)
484 and L81 (sfCherry2 Δ C4-Lifeact) were the best performing ones and are ideally placed for
485 F-actin organization measurements in live cells and tissues.

486 487 **Engineering actin filament organization reporters using G-actin.**

488
489 N-terminal GFP fusions of G-actin, with a flexible linker in between the GFP and the G-
490 actin, are widely used for monitoring actin localization in live cells and tissues. Early
491 studies using such fusions to *Dictyostelium discoideum* actin (Westphal et al., 1997), to
492 human non-muscle beta G-actin (Ballestrem et al., 1998) and to the *Drosophila* non-
493 muscle G-actin Act5C (Verkhusha et al., 1999) showed that such fusions are functional,
494 as long as their expression levels are kept low; the choice of an appropriate promoter to
495 keep GFP-actin levels low was shown to be critical for their functionality (Ballestrem et
496 al., 1998). An important finding was that C-terminal tagging of G-actin, even with tags as
497 small as a hexahistidine tag or a dodecapeptide, impairs its incorporation into actin
498 filaments (Brault et al., 1999; Chen et al., 2012). *Drosophila* expressing such C-terminally
499 tagged G-actin have flight muscle with virtually no detectable sarcomeric organization
500 and are flightless, but N-terminal fusions with the same tags restore sarcomeric
501 organization and flight capacity (Brault et al., 1999). Thus, to constrain GFP mobility in
502 fusions with human non-muscle beta G-actin, we generated exclusively N-terminal
503 fusions. We did not include linkers in these fusions, and we additionally shortened the C-
504 termini of GFP (Figure 4A, A1 to A5). We also generated an N-terminal fusion with a
505 tetracysteine peptide (Figure 4A, A6).

506 As an alternative to N-terminal fusions and to maximize our chances to constrain
507 GFP mobility, we also considered generating intramolecular GFP fusions. (Bendezu et
508 al., 2009) succeeded to generate a fully functional intramolecular mCherry fusion of the
509 bacterial actin homolog MreB by inserting mCherry right before helix 7 of MreB (van den
510 Ent et al., 2001). Very interestingly, a second study by (Chen et al., 2012) succeeded to
511 generate a functional intramolecular fusion of fission yeast actin by inserting a
512 dodecapeptide-based tetracysteine tag into Ser233-Ser234 of the loop following helix 7
513 (h7, hereafter), and use FIAsh labeling to monitor F-actin in fission yeast cells. Motivated
514 by these studies, we chose to engineer intramolecular fusions by inserting either full-
515 length GFP (Figure 4A, A7 to A23), the GFP strand β 11 (Figure 4A, A24 to A37), or a
516 tetracysteine peptide (Figure 4A, A38 to A47), either before or after h7 (Figure 4B). We
517 used the exact same insertion site after h7 as in the study by (Chen et al., 2012).
518 Fluorescence imaging showed that only fusions into the loop following h7 incorporated
519 into actin filaments (A8, A25, A40 and A41 in Figure 4A). We thus focused on this insertion
520 site for subsequent screening.

521 As a proof of principle that such intramolecular fusions are functional, we
522 compared the functionality of intramolecular full-length msfGFP fusions (“iGFP” for short)
523 for the two vertebrate non-muscle actin isoforms, namely human beta- and gamma-actin
524 isoforms, using the exact same insertion site after h7, like for construct A8 (Figure 4A).
525 The two isoforms have distinct localizations and functions (Baranwal et al., 2012; Chen
526 et al., 2017; Dugina et al., 2009; Shum et al., 2011), and intramolecular GFP fusions
527 would provide new less-perturbative tools to study actin isoform function given that they
528 differ only by four amino acids at their very N-terminus. To this end, we generated stable

529 inducible HeLa cell lines expressing the iGFP-actin isoform fusions (Figure S4C-M).
530 Quantification of mitotic and multinucleated cells upon depletion of the endogenous
531 isoforms using isoform-specific siRNAs showed that our iGFP fusions rescued these
532 defects (Figure S4C-F). The localization of the iGFP fusions during mitosis and in
533 nondividing cells recapitulated their distinct distributions (Figure S4I-M), corroborating
534 previous studies (Chen et al., 2017; Dugina et al., 2009) and confirming further their
535 functionality. Motivated by these results and in order to constrain fluorophore mobility in
536 intramolecular fusions with human beta G-actin, we generated constructs that did not
537 include linkers and where the N- and C-termini of GFP were shortened (Figure 4A). Three
538 out of four serines within our insertion site are highly conserved across actin sequences
539 (Figure 4B,C): we also generated constructs with differences in the exact number and
540 position of these serines to establish possible effects on fluorophore mobility.

541 We screened the generated G-actin fusions with regard to their fluorescence, their
542 capacity to integrate into F-actin, their localization and the extent to which GFP or FIAsh
543 is constrained based on polarimetry measurements (Figures 4A-E and S4N,O). All
544 terminal and intramolecular fusions with GFP and tetracysteine peptides were
545 fluorescent. However, the only intramolecular β 11-based fusion that was fluorescent was
546 the one that included linkers (fusion A25 in Figure 4A): we reasoned that the absence of
547 linkers and further shortening in the subsequent β 11-based fusions did not provide the
548 flexibility needed for the complementation of β 11 with GFP1-10 (Cabantous et al., 2005).
549 The absence of linkers and the additional shortening of the GFP C-terminus in terminal
550 fusions did not compromise binding to F-actin, but seemed to enrich less these fusions in
551 myosin-II containing SFs (Figures 4A and S4O). Myosin-II interacts with the actin N-
552 terminus providing a possible explanation for the latter observation. The absence of
553 linkers in intramolecular GFP fusions did not compromise binding to F-actin, either. F-
554 actin binding upon additional shortening of both GFP N- and C-termini in intramolecular
555 fusions depended on the extent of shortening, as well as the exact number and position
556 of the serine residues encompassing the insertion site. As expected, the use of a
557 truncated CMV promoter for low-level expression was critical, with the widely used full-
558 strength CMV promoter leading systematically to aggregation (Figure S4O). All G-actin
559 fusions localized similarly to the other ABD-GFP fusions (Figure S4O). Interestingly,
560 intramolecular tetracysteine peptide fusions labeled additionally nuclear F-actin (A41 in
561 Figure S4O), showing nuclear F-actin bundles morphologically very similar to ones
562 detected with the use of a nuclear actin chromobody (Lamm et al., 2020) and an actin-
563 NLS-FLAG construct (Kokai et al., 2014; Lawson et al., 2022). The small size of these
564 peptides compared to the size of GFP could possibly explain this difference: GFP fusions
565 were typically excluded from the nucleus, consistent with such an explanation.

566 Terminal and intramolecular GFP fusions without linkers and with extensively
567 shortened GFP termini were most efficient to constrain GFP mobility (Figures 4A,D-E and
568 S4N). We note that GFP mobility is much less constrained than in fusions with actin-
569 binding peptides and domains: we attribute this increased mobility to the inherent
570 flexibility of the actin N-terminus and of the insertion site loop in terminal and
571 intramolecular fusions, respectively. Despite this difference, constrained GFP fusions
572 directly to G-actin can still be useful for studies focusing on G-actin itself, notably actin
573 isoforms. The fusions A4 (msfGFP Δ C10-actin) and A18 (actin-h7-msfGFP Δ N7 Δ C11-
574 SSSSactin) are the best performing ones for F-actin organization measurements in live
575 cells.

576
577 Comparison of the localization of our organization reporters to different F-actin
578 populations, notably different types of SFs, in U2OS cells did not show any significant
579 differences. At the low-expression levels we used and during the transient expression of
580 the reporters, we did not detect any evident signs of perturbation in terms of SF
581 biogenesis, maintenance or organization. Given that different actin-binding probes have

582 different affinities for F-actin, and that cells and tissues express tens of actin-binding
583 proteins to regulate the dynamics, localization and specific geometries of actin
584 assemblies related to specific functions, it is expected that these same probes behave
585 differently in different cellular contexts. Thus, to gain deeper insights into the functionality
586 of our organization reporters, we chose to test them in a more physiological context,
587 notably in three different genetically tractable *in vivo* model systems: the fission yeast *S.*
588 *pombe*, the nematode *C. elegans* and the fruit fly *Drosophila melanogaster*.
589

590 **Actin filament organization reporters in fission yeast.**

591
592 We generated transgenic fission yeast expressing selected reporters. We focused on the
593 best performing reporters from our screen on SFs, in particular L22, L45, U20 and Af7,
594 and included the respective constructs with unconstrained GFP for comparison, i.e. L2,
595 L38, U7 and Af1, respectively. Cells expressing these reporters under the control of the
596 promoter of the actin cytoskeleton regulator Cdc42, looked healthy, with no signs of
597 vacuolation, and were rod-shaped, suggesting the absence of major polarity defects. We
598 started by comparing the localization of the reporters in populations of actively dividing
599 yeast cells (Figure S5A-D). Actin in fission yeast is found in three distinct structures: actin
600 patches, actin cables and the cytokinetic actomyosin ring (Figure S5B). Although all
601 reporters labeled all three structures, there were dramatic differences in their respective
602 enrichments, as assessed by the differences in labeling intensities of the different
603 structures (Figure S5A,B), as well as in the numbers of patches and cables labeled by
604 each reporter (quantification in Figure S5C,D). Patches and, to a lesser extent, rings,
605 were labeled well with Lifeact constructs, whereas cables and rings, and, to a lesser
606 extent, patches, were most prominent with Affimer6 constructs (Figure S5A-D). Utrophin
607 labeling seemed altogether very inefficient. We attribute these striking differences in
608 localization to differences in the affinities of the reporters for the different actin structures.

609 To assess the functionality of the reporters, we examined their effect in three
610 different contexts: the timing of the different stages of cytokinesis (Figure 5A,B), the
611 growth of cells under sensitized conditions, notably the presence of the Arp2/3 complex
612 inhibitor CK666 and the G-actin sequestering drug latrunculin A (LatA) (Figure 5C), and
613 finally genetic interactions with a profilin mutant (Figure 5D). Quantification of the timing
614 of cytokinesis stages showed that cytokinesis proceeded overall similarly for all reporters
615 with respect to a control strain expressing only cytokinetic markers, with cells completing
616 cytokinesis within ~40-50 minutes in all cases (see mean times for each stage in the
617 legend of Figure 5B). We observed the most important delays for the Affimer6 constructs,
618 which showed increased maturation and constriction times, and for some of the Lifeact
619 constructs, notably L22, which took longer for the assembly (Figure 5B).

620 The dilution assays to assess cell viability and growth in the presence of CK666
621 and LatA led to three observations. First, there was no difference in cell growth upon
622 expression of the reporters with DMSO as a vehicle control, reflecting their overall
623 nonperturbative character. Second, cell growth in the presence of CK666 was slightly
624 impaired upon expression of L22 and the effect was even more significant for the original
625 Lifeact construct, which is expressed at a higher level, from the actin promoter (Huang et
626 al., 2012). Third, the inability of cells to grow in the presence of LatA was significantly
627 reversed for the Affimer6 constructs, as well as the original Lifeact construct and L22
628 (Figure 5C). The main effect of CK666 is on actin patches, for the formation of which
629 Arp2/3 is essential. The CK666 results thus suggest that the original Lifeact and, to a
630 lesser extent, L22 interfere with branched actin formation. LatA, on the other hand, at the
631 low concentration used, impacts primarily the formation of cables, which are not essential
632 for growth, and of cytokinetic rings which are essential for cell division. The LatA results
633 thus reveal a stabilization effect on the rings upon expression of the Affimer6 constructs,
634 the original Lifeact construct and L22. The increased cytokinetic ring maturation and

635 constriction times for Affimer6 and increased ring assembly time for L22 we observed
636 could well be explained by the same mechanisms revealed from the drug assays. Finally,
637 dilution assays in the presence of a thermosensitive profilin mutant did not show any
638 significant difference for the reporters, suggesting that they do not interfere with actin
639 nucleation and polymerization *per se* (Figure 5D). Altogether, these results show that our
640 reporters are largely nonperturbative, however specific reporters can contribute to mild
641 perturbations, notably in the context of sensitized conditions.

642 As an example of the applicability of the reporters *in vivo*, we chose to measure
643 actin filament organization in the constricting cytokinetic ring of live dividing fission yeast
644 cells. We focused on the Affimer6 constructs Af1 and Af7 and the Lifeact constructs L2
645 and L22 which were most efficient in labeling the cytokinetic ring (Figure S5A,B).
646 Measurements of mean actin filament orientation (ρ angles) and alignment (ψ angles) in
647 constricting rings resembled the behavior of the respective constructs on SFs. The
648 unconstrained GFP fusions Af1 and L2 displayed very high ψ values, whereas Af7 and
649 L22 fusions bearing constrained GFP showed statistically significantly lower ψ values
650 (Figure 5E-G). The measured values were comparable to the ones on SFs, suggesting
651 highly aligned actin filaments, with filament alignment persisting throughout ring
652 constriction (Figure S5G). Considering that Af7 and L22 dipoles are parallel to actin
653 filaments (Figures 2B and 3G), the quantification of ρ angle distribution with respect to
654 the division plane showed that actin filaments are parallel to the constricting ring axis
655 (Figure S5E,F). Our results are fully consistent with recent electron cryotomography of
656 dividing fission yeast that revealed straight, overlapping actin filaments running nearly
657 parallel to each other and to the membrane (Swulius et al., 2018). The combination of the
658 organization reporters with mutants promises to further our understanding of the
659 mechanisms that drive actomyosin remodeling in cell division.

660

661 **Actin filament organization reporters in *C. elegans*.**

662

663 Next, we sought to test selected reporters in the context of animal morphogenesis,
664 notably *C. elegans* embryonic elongation (Figure S6A). To this end, we generated
665 transgenic *C. elegans* expressing the organization reporters L22, L45 and Af7 under the
666 control of an epidermal promoter (Figure S6B). To assess their functionality, we quantified
667 embryonic lethality by scoring egg hatching in comparison with wild-type embryos and
668 embryos expressing the original Lifeact-GFP reporter. The measured lethality was
669 comparable to wild-type embryos and lower than the one of Lifeact-GFP expressing
670 embryos (Figure 6A). In a second functionality test, we filmed living elongating embryos
671 and quantified embryonic length until hatching: embryonic elongation proceeded similarly
672 for all strains (Figure 6B), again confirming the minimally perturbative character of the
673 reporters.

674 Elongation of the *C. elegans* embryo proceeds along its anterior-posterior axis,
675 increasing in length about fourfold and decreasing in circumference about threefold, with
676 practically no cell divisions nor cell rearrangements (Priess and Hirsh, 1986). The
677 epidermis comprises three major cell types, namely dorsal, ventral and lateral seam cells.
678 Whereas actin filaments progressively form circumferential bundles in dorsal and ventral
679 epidermal cells (DV cells), actin filaments in seam cells have been reported to stay rather
680 disorganized throughout elongation (Gally et al., 2009; Vuong-Brender et al., 2017).
681 Recent work evidenced an interplay of stress anisotropy in seam cells and stiffness
682 anisotropy in DV cells as critical for elongation through a circumferential squeezing-like
683 mechanism (Vuong-Brender et al., 2017), prompting us to quantify actin filament
684 organization in DV and seam cells as a function of elongation.

685 The localization of L22, L45 and Af7 in the elongating epidermis was in line with
686 phalloidin staining (Priess and Hirsh, 1986) and the localization of a GFP fusion to the
687 actin-binding domain of the spectraplakine VAB-10 (Gally et al., 2009; Vuong-Brender et

688 al., 2017), showing the characteristic circumferential bundles in DV cells and a fuzzier
689 mesh-like distribution in seam cells (Figure S6C,D,F). Considering that Af7 and L22
690 dipoles are parallel to actin filaments (Figures 2B and 3G) and that L45 dipoles are
691 perpendicular to actin filaments (Figure 2C), quantification of actin filament organization
692 in the circumferential bundles of DV cells in >2-fold elongated (>2F) embryos showed that
693 actin filaments are parallel to the circumferential bundles (Figure 6I,J and Figure S6D-G),
694 as expected, with ψ values comparable to the ones on SFs, suggesting highly aligned
695 actin filaments (Figure 6C). Strikingly, quantification of actin filament orientation with
696 respect to the DV/seam boundary showed that the polarization of actin filament
697 orientation was already present in 1.5-fold elongated (1.5F) embryos before the formation
698 of distinct circumferential bundles (Figure 6E,F and Figure S6C), with actin filament
699 alignment increasing as bundles form (Figure 6D). What was, however, even more
700 unexpected was that actin filament organization in seam cells was also polarized: seam
701 cells in 1.5F embryos contained already actin filaments oriented perpendicular to the
702 DV/seam boundary and with regions of actin filament alignment. As elongation proceeds,
703 this polarization becomes progressively more pronounced, with actin filaments oriented
704 essentially perpendicular to the DV/seam boundary, just like in DV cells, and with regions
705 of high actin filament alignment (Figure 6D-J and Figure S6E,G). The experimental
706 demonstration of the polarization of the actin cytoskeleton during *C. elegans* embryonic
707 elongation, a first of its kind, reveals the potential of the new organization reporters, which,
708 combined with mutants and biophysical measurements, promise to uncover the
709 mechanisms that drive animal morphogenesis.

710

711 **Actin filament organization reporters in *Drosophila*.**

712

713 We finally chose to characterize selected organization reporters in *Drosophila*. To this
714 end, we generated transgenic *Drosophila* expressing reporters with the inducible GAL4/
715 UAS expression system, allowing us to express them in the early embryo, the wing and
716 the indirect flight muscle using respective tissue-specific promoters. Actin filament
717 organization measurements in the actomyosin rings of living cellularizing embryos
718 recapitulated earlier polarimetry measurements in fixed phalloidin-stained embryos
719 (Mavrakakis et al., 2014) confirming the arrangement of highly aligned filaments following
720 the contour of the associated membrane front (Figure 7A and Figure S7A). Apicolaterally
721 to this front and at the basal-most part of the lateral membranes, a basal adherens
722 junction has been reported to form (Hunter and Wieschaus, 2000). In this junction, actin
723 filaments were found to be highly aligned to each other, following the junction contour in
724 line with a belt-like arrangement (Figure 7B).

725 We assessed the functionality of the reporters in two systems that depend on the
726 integrity of the actin cytoskeleton, namely the adult wing and the adult flight muscle. To
727 measure their effect on wing growth, we compared the wing area in wings expressing the
728 reporters with the one in wings bearing only the wing-specific promoter (control), wings
729 expressing the original Lifeact-GFP, and wings expressing a dominant-negative form of
730 the insulin receptor expected to reduce wing growth. Wing growth was indeed reduced
731 by ~46% for the latter, but was largely comparable, within less than 8% of change, among
732 the control and the other strains (Figure S7B). As a second functionality test, we
733 performed flight tests to compare the flight ability of strains expressing different reporters
734 with the one of strains bearing only the muscle-specific promoter (control) and strains
735 expressing two widely used actin localization reporters: the actin-binding domain of
736 moesin (GFP-GMA) and Lifeact-GFP (Figure 7C). Although all reporters localized largely
737 as expected in the muscle sarcomeres (Figure S7C), flight tests showed significant
738 differences among the strains. The flight ability of flies expressing L45 and U20 was
739 comparable to the one of control and GFP-GMA flies. However, flies expressing either
740 L22 or the original Lifeact-GFP, performed very poorly, with Af7 expressing flies being

741 entirely flightless (Figure 7C); the development of the flight muscle in the latter strain was
742 altogether impaired (Figure S7C). The muscle-specific promoter being active in all
743 embryonic, larval and adult muscle, we attributed this dramatic effect to the expression of
744 the reporters throughout muscle development, and reasoned that their limited expression
745 after muscle development could be less perturbative. In support of this scenario, and with
746 the use of the temperature-sensitive GAL80ts system to express the reporters only in a
747 narrow time window of a few days in adult muscle, the flight ability of all strains was
748 improved, including the strains expressing the original Lifeact-GFP, L22, and Af7 (Figure
749 7C). Muscle morphology and sarcomere localization were comparable to the control in all
750 cases, including now for Af7 (Figure S7D). Importantly, despite their limited temporal
751 expression, the fluorescence levels of the reporters rendered them usable for polarimetry
752 measurements in the flight muscle.

753 To this end, we dissected live flight muscle expressing L22, L45 and Af7, and the
754 original Lifeact-GFP for comparison, and measured actin filament organization in the
755 respective myofibrils. Not surprisingly, ψ values in the original Lifeact-GFP were too high
756 to render this fusion usable for organization measurements, but L22, L45 and Af7
757 behaved as expected, with Af7 further displaying the lowest ψ values i.e., the highest
758 filament alignment, from all systems (Figure 7D), in line with the crystal-like arrangement
759 of actin filaments in sarcomeres reported by EM (Loison et al., 2018). Considering the
760 GFP dipole orientations of L22, L45 and Af7 with respect to actin filaments, actin filament
761 orientation and alignment maps revealed the expected high order within and across
762 different myofibrils in the muscle (Figure 7E-G). The potential of the reporters to quantify
763 actin filament organization in live muscle, combined with the genetically-tractable
764 character of *Drosophila* and its use as model for studying muscle biogenesis and
765 pathophysiology, promises to contribute novel insights into the regulation of muscle
766 structure and function.

767 768 **DISCUSSION**

769
770 Despite the established contribution of the actin cytoskeleton to cell and tissue integrity
771 and function in a wide range of biological processes, and its direct link to animal
772 pathophysiology, measuring its organization in real time in living cells remains a
773 challenge. Polarimetry exploits the interaction between fluorophore dipoles and polarized
774 light for probing molecular organization. However, fluorophore mobility must be
775 constrained to allow for such measurements. Our novel genetically-encoded reporters
776 bearing constrained fluorescent proteins enable the quantification of actin filament
777 orientation and alignment, and dynamical changes thereof, in living cells. We succeeded
778 in engineering constrained GFP fusions to widely used actin localization reporters,
779 namely Lifeact, the Utrophin calponin homology domain, F-tractin, Affimer6 and G-actin
780 itself, thus providing the possibility to correlate any biological process of interest with live
781 measurements of actin filament organization by polarimetry. We further provide reference
782 angle values for each reporter in SFs that can be used for comparison and interpretation
783 of organization measurements in any F-actin population of interest with no need for any
784 *a priori* knowledge of its organization.

785 Even though ensemble measurements cannot resolve individual filaments, their
786 molecular-scale organization at a given image pixel is detectable and can be quantified
787 by polarimetry. Moreover, the mesh size of the actin network is typically on the order of
788 100 nm or less (Chugh and Paluch, 2018), making it so far only attainable in a fixed cell
789 context with EM and single molecule localization microscopy. Thus, the capacity to obtain
790 quantitative measurements of actin filament orientation and alignment per image pixel in
791 a living cellular context is of significant added value. Cells continuously and dynamically
792 remodel actin filaments in order to accomplish specific biological functions, and do so
793 through the complex regulation of actin filament architecture and dynamics. Bottom-up

794 approaches with purified proteins are key for assigning specific functions, for example
795 filament branching, to distinct actin-binding proteins (Mullins and Hansen, 2013).
796 However, whether and how these assigned functions account for F-actin organization in
797 cells, in the presence of tens of other actin interactors, can now be formally tested by
798 combining live cell organization measurements with mutants or treatments affecting one
799 or several interactors.

800 The use of the reporters in the context of cell and tissue morphogenesis, including
801 during embryogenesis and organogenesis, promises to uncover how specific geometries
802 of actin filaments contribute to function. Organization measurements with the novel
803 reporters in the presence of mutants will further provide new insights into the
804 developmental regulation of F-actin organization. The genetically-encoded character of
805 the reporters renders them also fully compatible with animal disease models, enabling *in*
806 *vivo* studies on the role of any gene of interest in F-actin organization in the context of
807 pathophysiology, for example in muscle development, maintenance and repair, in health
808 and disease. Being able to measure changes in filament organization in real-time will
809 additionally help generate accurate biophysical models with experimentally testable
810 predictions regarding how F-actin organization impacts function.

811 The novel F-actin organization reporters are compatible with all fluorescence
812 microscopy techniques routinely used for live ensemble imaging that can be coupled with
813 polarized fluorescence imaging, such as transmission polarized microscopy
814 (Abrahamsson et al., 2015; DeMay et al., 2011b), wide-field (Vrabiou and Mitchison,
815 2006), confocal (Kress et al., 2013) and spinning disk confocal microscopy (Wang et al.,
816 2013), total internal reflection microscopy (Sund et al., 1999) and two-photon microscopy
817 (Benninger et al., 2005; Ferrand et al., 2014; Gasecka et al., 2009; Lazar et al., 2011).
818 The reporters are also compatible with super-resolution imaging techniques, either based
819 on polarized structured illumination microscopy employing standard FPs (Hafi et al.,
820 2014; Zhanghao et al., 2019), or based on single molecule orientation and localization
821 microscopy using photoactivatable or photoconvertible FPs (Brasselet and Alonso, 2023).
822 It is important to note that the introduction of a single point mutation to sfGFP or of a few
823 point mutations to sfCherry2 are sufficient to generate the respective photoactivatable
824 versions (Feng et al., 2017; Slocum and Webb, 2017). Given that these mutations are
825 within the barrel structure, we do not expect them to alter the mobility of the FP. Our
826 strategy can thus be simply adapted to the context of single-molecule organization
827 measurements using, for example, single-particle tracking PALM coupled to polarization
828 splitting (Rimoli et al., 2022; Valades Cruz et al., 2016) or Point Spread Function
829 engineering (Brasselet and Alonso, 2023). The ultimate choice of the technique will
830 depend on the desired spatial and temporal resolution, optical sectioning and imaging
831 depth, as well as on the requirement for capturing the actin filament organization
832 dynamics under study. Thus, the use and interpretation of the organization
833 measurements using the reporters must take into account the specificities and limitations
834 of each technique. All measurements in this study have used a spinning disk confocal
835 microscope with polarized excitation for second-scale measurements of F-actin
836 organization. If higher temporal resolution is needed, for example for monitoring
837 fluctuating filaments or rapidly remodeling cells, a wide-field microscope with polarization
838 splitting would allow for subsecond-scale measurements using the exact same reporters
839 (Kampmann et al., 2011; Mattheyses et al., 2010; Mehta et al., 2016; Nordenfelt et al.,
840 2017; Swaminathan et al., 2017; Vrabiou and Mitchison, 2006). Our open-source
841 software, PyPOLAR, for analyzing polarimetry data generated by a range of different
842 techniques has been designed explicitly for use by biologists and biophysicists, and
843 promises to further facilitate the use of the novel molecular tools.

844 The genetically-encoded character of the reporters makes them particularly useful
845 for live cell and tissue studies, both *in vitro* and *ex vivo*, as well as *in vivo* in the context
846 of genetically-tractable model organisms, as exemplified by their use in fission yeast,

847 *C.elegans* and *Drosophila*. The use of specific promoters and inducible expression
848 systems can control their spatial and temporal expression, as well as their levels. As
849 expected for any actin-binding protein, there is an inevitable risk for competition and
850 interference with endogenous actin-binding interactors, more so the higher the levels of
851 the reporters. The regulation of their expression is thus a key advantage, as shown by
852 the mitigation of the effects we observed on *Drosophila* flight capacity and flight muscle
853 integrity by Af7 when lowering its levels. In addition to the controls and functional readouts
854 we provide in our study for the specific models we use, additional or different readouts
855 related to a given question under study might be important to consider.

856 As already reported in the literature and also shown in our study, different actin-
857 binding probes have different affinities for F-actin and for distinct actin filament
858 assemblies depending on the density and geometry of the latter, as well as on the
859 presence of competing actin-binding proteins (tropomyosins, myosins, formins). The
860 availability of constrained GFP fusions to five widely used F-actin localization reporters,
861 including G-actin itself, increases the chances that one is able to label and consequently
862 measure the organization of the F-actin pools of interest. Constrained Cherry fusions for
863 F-actin organization measurements provide additional experimental flexibility, notably for
864 two-color imaging with GFP fusions to any protein of interest while measuring F-actin
865 organization. Our red FP fusions are also compatible with the standard CFP/YFP-like
866 donor/acceptor pairs used for FRET-based force measurements (Gayraud and Borghi,
867 2016), enabling a direct correlation between F-actin organization and mechanical
868 properties.

869 Finally, our results from the engineering of constrained FP fusions to ABDs
870 informed us at different levels with respect to the mechanisms of FP immobilization. First,
871 shortening of the N- and C-termini in terminal fusions seems to be the most efficient way
872 to constrain sfGFP and sfCherry2 mobility without compromising their fluorescence.
873 Second, shortening of the FP termini might compromise F-actin binding if the fused ABD
874 terminus is shortened at the same time; our results suggest that two residues between
875 the end of the FP barrel and the ABD are typically needed so as not compromise F-actin
876 binding. Third, circularly permuted sfGFP fusions can constrain GFP mobility, but not
877 nearly as efficiently as terminal fusions because cpGFP fusions tolerate poorly the
878 shortening of the GFP termini or/and the shortening of the ABD: fluorescence or/and F-
879 actin binding are rapidly compromised upon such shortening because of the flexibility
880 required to connect the original termini of cpGFP. Fourth, FP immobilization ultimately
881 depends on the flexibility of the terminus of the fused ABD or of the secondary structure
882 of the ABD (e.g. loop) to which it is fused: if the ABD terminus or the secondary structure
883 element is inherently flexible, even the shortest FP will remain mobile. Even though our
884 results relate primarily to sfGFP and sfCherry2 fusions to ABDs, the above-mentioned
885 conclusions can be rationally applied to other FPs, and fusions to proteins other than
886 actin-binding ones, to generate new tools for measuring any protein organization by
887 polarimetry. Structural and cell biology approaches employing FP-based sensors to probe
888 protein proximity, protein-protein interactions and mechanical forces, notably the ones
889 using FRET, are also likely to benefit from using constrained FP fusions.

890 **ACKNOWLEDGMENTS**

892 We thank Louwrens van Dellen (I. Fresnel, Marseille, France) for the development of the
893 image acquisition software. This research has received funding from the French National
894 Research Agency (ANR) grants Equipex+ IDEC (France 2030 investment plan ANR-21-
895 ESRE-0002), 3DPolariSR (ANR-20-CE42-0003), SEPTIMORF (ANR-17-CE13-0014),
896 SEPTISS (ANR-22-CE13-0039), and from the France-BioImaging infrastructure (ANR-
897 10-INBS-04). This research has further received funding from the Excellence Initiative of
898 Aix-Marseille University – A*Midex (A*Midex grant NEUROPOL), a French

899 “Investissements d’Avenir” program, the Fondation pour la Recherche Médicale (FRM
900 grant ING20150531962) and SATT Sud-Est.

901

902 **AUTHOR CONTRIBUTIONS**

903 C.S.M. : Methodology, Investigation, Validation, Formal analysis, Visualization, Writing –
904 original draft, Writing – review & editing; F.I. : Investigation; S.K.S. : Investigation,
905 Validation, Formal analysis, Visualization, Writing – original draft, Writing – review &
906 editing; T.C.P. : Investigation, Validation, Visualization, Formal analysis; C.S. :
907 Investigation, Validation, Formal analysis, Visualization, Writing – original draft, Writing –
908 review & editing; M.R.-L. : Investigation; C.N.P. : Investigation; S.O. : Investigation; M.G. :
909 Investigation; A.L. : Investigation; S.R.B. : Investigation; L.R. : Investigation; F.A. :
910 Investigation; C.V.R. : Investigation; F.S. : Writing – review & editing, Supervision,
911 Resources; F.R. : Writing – review & editing, Supervision, Resources; A.W. : Writing –
912 review & editing, Supervision, Resources; L.L. : Investigation, Validation, Formal analysis,
913 Visualization, Writing – original draft, Writing – review & editing; J.-D.P. : Investigation,
914 Visualization, Writing – original draft, Writing – review & editing; S.C. : Investigation,
915 Validation, Formal analysis, Visualization, Writing – original draft, Writing – review &
916 editing, Resources; S.A.R. : Investigation, Validation, Formal analysis, Visualization,
917 Writing – original draft, Writing – review & editing, Supervision, Resources ; C.C. :
918 Software; S.B. : Conceptualization, Methodology, Investigation, Software, Writing –
919 original draft, Writing – review & editing, Supervision, Resources, Project administration,
920 Funding acquisition; M.M. : Conceptualization, Methodology, Investigation, Software,
921 Validation, Formal analysis, Visualization, Writing – original draft, Writing – review &
922 editing, Supervision, Resources, Project administration, Funding acquisition

923

924 **DECLARATION OF INTERESTS**

925 The authors declare no competing interests.

926

927 **STAR methods**

928

929 **RESOURCE AVAILABILITY**

930

931 **Lead contact**

932 Further information and requests for resources, reagents, and software should be
933 directed to and will be fulfilled by the lead contact, Manos Mavrakis
934 (manos.mavrakis@fresnel.fr).

935

936 **Materials availability**

937 All plasmids and strains generated in this study are available upon request.

938

939 **Data and code availability**

940 The datasets supporting the current study have not been deposited in a public repository
941 but are available from the lead contact upon request. The codes and softwares developed
942 and used in this study are open source and available on GitHub under a BSD license; the
943 software identifiers are listed in the Key Resources Table and the links are provided in
944 the respective method details sections.

945

946 **EXPERIMENTAL MODEL AND SUBJECT DETAILS**

947

948 **Cell lines and cell culture**

949 U2OS osteosarcoma cells were used for the screening of actin organization reporters
950 with respect to their localization and usability for polarimetry measurements. U2OS cells
951 were from ATCC (HTB-96). Cells were maintained in McCoy's medium (Thermo Fisher,
952 Cat#16600082) supplemented with 10% fetal bovine serum (Dominique Dutscher, Cat#
953 S181H), 100 U/mL penicillin and 100 µg/mL streptomycin antibiotics (Sigma-Aldrich,
954 Cat#P4333) in a humidified atmosphere at 37°C containing 5% CO₂. Transfections were
955 performed 16 h prior to live imaging using FuGENE HD Transfection Reagent (Promega,
956 Cat#E2311), following the manufacturer's instructions. To obtain single cells for imaging,
957 25×10³ U2OS cells were typically seeded into a 24-well glass bottom plate (Cellvis,
958 Cat#P24-1.5H-N) a day prior to the day of transfection, for allowing an optimal number of
959 cells to attach and spread. A total of 0.2 µg of DNA and a 4:1 ratio of FuGENE HD (µL) :
960 DNA (µg) were used per reaction. To minimize overexpression, the amount of DNA for
961 pCMV plasmids was reduced to 50 ng, leading to a 16:1 ratio of FuGENE HD (µL) : DNA
962 (µg). Cells were imaged 16h post-transfection.

963 HeLa cells were used for the characterization of intramolecular GFP (iGFP)-beta and -
964 gamma actin fusions. Stable HeLa cell lines with regulated expression of either iGFP-
965 beta actin or iGFP-gamma actin were generated with the Flp-In system (Life
966 Technologies) using HeLa cells that contained a single FRT site according to the
967 manufacturer's instructions (Renshaw et al., 2014). The resulting cell lines were cultured
968 in Dulbecco's Modified Eagle Medium (Wisent Bio Products, Cat#319-030 CL)
969 supplemented with 10% fetal bovine serum (Wisent Bio Products, Cat#080-650), 1%
970 penicillin/streptomycin (Invitrogen Cat#15140122), 5 µg/mL blasticidin (BioShop Canada
971 Inc, Cat#BLA477), and 2 µg/mL puromycin (BioShop Canada Inc, Cat#PUR333).
972 Expression of GFP fusion proteins were induced by addition of 0.25 µg/mL doxycycline
973 to the growth media for 24 h before either fixation or harvesting. Cells were maintained in
974 a Forma Series II incubator (Thermo Scientific) at 37°C in a 5% CO₂ atmosphere.

975

976 **Fission yeast strains, maintenance and genetics**

977 Standard *Schizosaccharomyces pombe* media and genetic manipulations were used
978 (Moreno et al., 1991). All strains used in the study were isogenic to wild-type 972 and
979 their genotypes are described in Table S3. The generation of transgenic strains is
980 described in the method details section. Strains from genetic crosses were selected by
981 random spore germination and replica in plates with appropriate supplements or drugs.
982 Transformations were performed using the lithium acetate-DMSO method as described
983 in (Bahler et al., 1998). Drop assays (Figures 5C,D) were performed by serial dilutions of
984 1/4 from a starting sample of optical density of 1.0 of the indicated strains, which were
985 plated on YE5S medium supplemented with the corresponding drug and incubated for 3
986 days at 28°C unless stated differently.

987

988 **C. elegans strains, maintenance and genetics**

989 Bristol strain N2 was used as the wild-type strain. *C. elegans* strains used in this study
990 and their genotypes are listed in the Key Resources Table and were reared using
991 standard methods (Brenner, 1974). The generation of transgenic strains is described in
992 the method details section. The strains were grown at 20°C and fed *Escherichia coli*
993 OP50. The EG6699 (unc-119(ed3) III) strain, used as the host strain of FBR193, FBR195

994 and FBR196 strains generated in this study, was grown at 15°C and fed *E. coli* HB101
995 before injection (Hochbaum et al., 2010).

996

997 ***Drosophila* strains, maintenance and genetics**

998 *Drosophila melanogaster* strains used in this study and their genotypes are listed in the
999 Key Resources Table. The generation of the transgenic strains UASp–L22, UASp–L45,
1000 UASp–U20, and UASp–Af7 is described in the method details section. Fly stocks were
1001 grown and maintained at 25°C on semi-defined medium
1002 (<https://bdsc.indiana.edu/information/recipes/germanfood.html>). The GAL4/UASp
1003 expression system was used to drive expression in the *Drosophila* embryo using GAL4
1004 expressed under the control of the maternal alphaTub67C promoter (mat- α -tub–GAL4)
1005 (BDSC_80361). Crosses were maintained at 25°C. The GAL4/UAS expression system
1006 was used to drive the expression of actin organization reporters in *Drosophila* indirect
1007 flight muscles. Mef2-GAL4 (BDSC_27390) or tub-GAL80ts ; Mef2-GAL4 (BDSC_7108,
1008 BDSC_27390) females were crossed to males of the following genotypes: w[1118]
1009 (BDSC_3605), UAS–GFP-GMA (BDSC_31776), UAS–Lifeact-EGFP (BDSC_35544),
1010 UASp–L22, UASp–L45, UASp–U20, and UASp–Af7. Crosses with the Mef2-GAL4 driver
1011 were grown at 25°C. Crosses with the tub-GAL80ts ; Mef2-GAL4 driver were grown at
1012 18°C (no GAL4 activity): a few days after eclosion, adults were transferred to a permissive
1013 temperature of 31°C for 5 days prior to flight tests or fixation/staining or to a permissive
1014 temperature of 25°C for 5 days prior to live polarimetry. The GAL4/UAS expression
1015 system was used to drive the expression of actin organization reporters in the *Drosophila*
1016 wing. nub-GAL4 (BDSC_86108) females were collected within 2 days and combined to
1017 create a uniform population. Eight of these females were crossed to three males of the
1018 following genotypes: UAS–dInR-DN (BDSC_8253), sqh–Lifeact-EGFP, UASp–L22,
1019 UASp–L45, UASp–U20, and UASp–Af7. The rearing temperature was maintained at
1020 25°C, and the tubes were flipped daily.

1021

1022 **METHOD DETAILS**

1023

1024 **Generation of mammalian expression plasmids for screening actin organization** 1025 **reporters**

1026 All constructs were designed in silico with SnapGene (Dotmatics) and are listed in Table
1027 S1. To drive expression of the constructs in mammalian cells, we used the immediate
1028 early enhancer and promoter of human cytomegalovirus (CMV promoter, 508 base pairs),
1029 as well as a truncated version (CMV_{trunc}, 54 base pairs) for low-level expression; the latter
1030 was originally generated for reduced expression of EGFP-beta-actin (Watanabe and
1031 Mitchison, 2002). Addgene plasmids #31502 and #54759 were used to obtain the
1032 CMV_{trunc} and CMV backbones, respectively. All constructs screened for actin organization
1033 reporters were driven by CMV_{trunc} apart from the ones labeled with an asterisk in Figures
1034 2A, 3A, 3D, 3G, 4A, S2A, S3A, S3F and the iGFP-beta- and -gamma constructs (Figure
1035 S4E-O). Fluorescent protein constructs screened for fluorescence in the truncation
1036 screens (Figures 1G,H and S4A,B) were driven by CMV. Lifeact-mEGFP and EGFP-beta-
1037 actin cDNAs were a gift from Yannick Hamon (CIML, France). FtrN9-52-mEGFP and
1038 EGFP-Affimer6 cDNAs were a gift from John Hammer (NIH/NHLBI, USA) and Michelle
1039 Peckham (University of Leeds, UK), respectively. Beta- and gamma-actin cDNAs were a

1040 gift from Boris Hinz (University of Toronto, Canada). Synthetic genes for sfGFP, msfGFP,
1041 human beta-actin and GFP11 Δ C8-FtrN10-52-GFP1-10 were from Eurofins Genomics
1042 (Germany). Fluorescent protein fusions were generated using monomeric (A206K) EGFP
1043 (mEGFP) (Zacharias et al., 2002; Zhang et al., 1996), monomeric (V206K) superfolder
1044 GFP (msfGFP) (Costantini et al., 2012; Cranfill et al., 2016; Pedelacq et al., 2006;
1045 Zacharias et al., 2002), monomeric Apple (mApple) (Cranfill et al., 2016; Shaner et al.,
1046 2008) and superfolder Cherry2 (sfCherry2) (Feng et al., 2017). To optimize the
1047 intramolecular self-association of β 11 with the GFP1-10 moiety in our circular permutants,
1048 we have used the sfGFP-evolved sequences, GFP1-10 OPT and GFP11 M3, which have
1049 been optimally engineered to work in bipartite split-GFP complementation assays
1050 (Cabantous et al., 2005). All constructs were generated with seamless cloning (In-Fusion
1051 HD Cloning Plus Kit from Takara Bio, Cat. # 638910) using NheI/BamHI (or AflIII/BamHI
1052 for iGFP constructs) linearized plasmid backbones and the oligonucleotide primer
1053 sequences listed in Table S2. Primers were Cloning Oligo (<60 bp) or EXTREmer (>60
1054 bp) synthesis and purification quality from Eurofins Genomics (Germany). Restriction
1055 enzymes were FastDigest enzymes from Thermo Scientific. All plasmids were verified by
1056 sequencing (Eurofins Genomics, Germany) after each cloning step.

1057 We note the following with respect to residue numbering of EGFP/sfGFP in our study:
1058 although the valine following the initiating methionine is typically numbered 1a to maintain
1059 correspondence between EGFP/sfGFP and wild-type GFP numbering (Tsien, 1998), we
1060 number this valine as 2 in this study to facilitate the naming of N-terminal truncations in
1061 the screen. As a result, the last residue of EGFP/sfGFP is 239, an N-terminally truncated
1062 msfGFP mutant missing the first six residues (Δ N6) starts with ELFTGV..., and a C-
1063 terminally truncated msfGFP mutant missing the last nine residues (Δ C9) ends with
1064 ...AAGI.

1065

1066 **Screening of actin organization reporters in live U2OS cells**

1067 **Confocal fluorescence microscopy and image processing**

1068 For live cell imaging, right before microscopy and due to the absence of CO₂ control on
1069 our microscope setup, the culture medium was exchanged by Leibovitz medium (Thermo
1070 Fisher, Cat#21083027) supplemented with 10% fetal bovine serum and antibiotics. Cells
1071 were kept at 37°C in a heating chamber (OkoLab, Cat#H301-TUNIT-BL). Fluorescence
1072 images were acquired using a custom spinning disk microscope (detailed in the
1073 Polarimetry methods section) with a Nikon Plan Apo \times 100/1.45 NA oil immersion
1074 objective lens, 488- 561- and 641-nm laser lines and an iXon Ultra 888 EMCCD camera.
1075 Z-stacks were acquired with a Δ z interval of 0.5 μ m. Exposure times were in the range of
1076 0.5–2.0 s depending on the exact condition.

1077 Images were processed with the open-source image processing software ImageJ/Fiji.
1078 The images displayed in Figure 1H and Figure S4B are maximum intensity projections of
1079 two consecutive z-planes displayed with the same intensity range to allow for intensity
1080 comparison between the FP truncation mutants. All the other shown images are
1081 maximum intensity projections of two consecutive z-planes contrasted manually in order
1082 to optimize the image display.

1083

1084 **Polarimetry measurements in live U2OS cells**

1085 Polarimetry stacks using 36 polarization angles were recorded in focal planes containing
1086 peripheral stress fibers with a typical exposure time of 0.1-0.2 s per polarized image (see
1087 details for the optical setup and signal processing in the Polarimetry methods section).
1088 Typically, a minimum of five fields of views containing single cells was acquired per
1089 experimental condition. Polarimetry stacks were systematically registered using the
1090 StackReg plugin for ImageJ to correct for x and y axis drift during acquisition. To select
1091 peripheral SF-associated pixels for analysis, binary masks of SF segments were
1092 generated using the open source tool FilamentSensor 0.2.3 (Eltzner et al., 2020), freely
1093 available at <http://www.filament-sensor.de/>. A pre-processing tab in the FilamentSensor
1094 software requires adjustment in the contrast and removal of standalone pixels, followed
1095 by the optional application of filters. A standard and optimized preprocessing was using
1096 Laplace filter, 8 neighbors and factor 4; Gaussian filter, sigma 1; Cross correlation filter,
1097 size 10 and zero 30%; and a directed Gaussian filter, sigma 8. The binarization method
1098 chosen was by area, and filament detection parameters were typically chosen as follows:
1099 minimum mean value 25, sigma 2, minimum standard deviation 5, minimum filament
1100 length 20, minimum angle difference 20, tolerance 5%. The final selection was done
1101 manually, and only identified filaments that were colocalizing with peripheral SFs were
1102 used to generate the binary masks for selecting the pixels for polarimetry analysis.
1103 Polarimetry data were analyzed according to the framework defined by (Kress et al.,
1104 2013) to obtain the ρ and ψ angle per image pixel. Analysis and data representation,
1105 including color-coded stick representations of the measured angles per pixel were done
1106 with the Polarimetry software which is a Matlab App Designer standalone application. The
1107 source code is available at <https://github.com/cchandre/Polarimetry.git>, and the desktop
1108 app can be freely obtained at <https://www.fresnel.fr/polarimetry> under a BSD license. The
1109 Matlab-based Polarimetry software is the precursor of the Python-based app PyPOLAR
1110 used for the analysis of the yeast, *Drosophila* and *C. elegans* polarimetry data (see
1111 respective methods sections). The distributions of the ψ angles are represented in box
1112 plots with overlaid data points. Each data point represents a single actin fiber. If more
1113 than one fibers were identified in the same field of view, measurements for each fiber are
1114 shown as distinct datapoints, which results in more than one measurements per field of
1115 view. On each box, the central mark indicates the median, and the left and right edges of
1116 the box indicate the 25th and 75th percentiles, respectively. The whiskers extend to the
1117 most extreme data points not considered outliers. Boxplots were generated with custom-
1118 written Matlab code (see *Data post-processing with Matlab* in
1119 <https://www.fresnel.fr/polarimetry>). The number of measurements for each construct, the
1120 respective median ψ values and the statistical test used in GraphPad Prism to evaluate
1121 differences are mentioned in the respective legend.

1122

1123 **Polarimetry measurements in fixed U2OS cells**

1124 U2OS cells were fixed for 20 min with 4% paraformaldehyde (Electron Microscopy
1125 Sciences, Cat#15714) in 37°C-prewarmed cytoskeleton buffer (10 mM MES pH 6.1, 150
1126 mM NaCl, 5 mM EGTA, 5 mM MgCl₂, 5 mM glucose), followed by 2 × 5 min wash steps
1127 in phosphate-buffered saline (PBS) solution. Cells were subsequently incubated with
1128 0.165 μ M Alexa Fluor 488-phalloidin (Thermo Fisher Scientific, Cat# A12379) or 0.165
1129 μ M SiR-actin (Spirochrome, Cat#SC006) in PBS containing 0.1% saponin and 1% IgG-
1130 free/protease free bovine serum albumin (Jackson ImmunoResearch, Cat#001-000-161)

1131 for 1 h at RT. Coverslips were mounted with 15 μ L Fluoromount (F4680; Sigma-Aldrich)
1132 for image acquisition.

1133 Polarimetry stacks using 18 polarization angles were recorded in focal planes containing
1134 ventral and peripheral stress fibers with a typical exposure time of 0.1-0.2 s per polarized
1135 image. The pixels of the stress fibers for analysis were selected by a combination of
1136 intensity thresholding and manual selection of the region to analyze. Analysis and data
1137 representation, including color-coded stick representations of the measured angles per
1138 pixel were done with Polarimetry or PyPOLAR softwares. The distributions of the ψ angles
1139 are represented in box plots with overlaid data points as described above for
1140 measurements in live cells. The number of measurements for each dye and the
1141 respective median ψ values are mentioned in the respective legend.

1142 1143 **Flow cytometry analysis of truncation mutants of fluorescent protein variants**

1144 U2OS cells were seeded at a density of 5×10^4 cells per well in 24-well plates. After 24 h,
1145 cells were transfected with 0.5 μ g of corresponding plasmid DNAs in 50 μ L of Jet Prime
1146 Buffer mixed with 1 μ L of jetPRIME reagent (Polyplus, Cat#101000046). Twenty-four
1147 hours after transfection, cells were trypsinized, resuspended in PBS supplemented with
1148 2% fetal bovine serum, then transferred in 96-well conical bottom plates. Cells were fixed
1149 with 3.7% paraformaldehyde for 10 min and resuspended in 1% BSA, PBS buffer. Green
1150 (mEFP, msfGFP) and red (mApple, sfCherry2) fluorescence were collected on 10,000
1151 cells using a MACSQuant VYB flow cytometer (Miltenyi Biotec). The fluorescence
1152 threshold was defined based on the background fluorescence of untransfected U2OS
1153 cells. The percentage of green and red positive fluorescence was analyzed with FlowJo®
1154 software (BD Biosciences). The fluorescence of full-length constructs was normalized to
1155 100% for each independent experiment. Bar graphs of the measured fluorescence were
1156 prepared with GraphPad Prism. The mean values and the statistical test used to evaluate
1157 differences are indicated in the respective legend.

1158 1159 **Characterization of intramolecular GFP (iGFP)-beta and -gamma actin fusions**

1160 **siRNA treatment and rescue experiments**

1161 HeLa cells grown to 40% confluency in 6-well plates were transfected with 100 pmol
1162 double-stranded siRNA targeting *ACTB* (sequence #1:
1163 AAAUAUGAGAUGCGUUGUUACAGGA; sequence #2:
1164 UCCUGUAACAACGCAUCUCAUAAUUUGG) or *ACTG1* (sequence #1:
1165 GCAUGGGUAAUUGAGAAUAGAAAT; sequence #2:
1166 AUUUCUAUUCUCAAUUAACCCAUGCAG) using Lipofectamine 2000 (Invitrogen,
1167 Cat#11668019) following manufacturer's instructions. For rescue experiments, siRNA-
1168 resistant transgenes were expressed 24 h after siRNA transfection and either fixed or
1169 harvested 48 h post-siRNA transfection. All siRNAs were obtained from IDT (Integrated
1170 DNA Technologies).

1171 1172 **Cell harvesting, SDS-PAGE, and western blotting**

1173 HeLa cells grown to near confluency in 6-well dishes were harvested by scraping in 100
1174 μ L RIPA lysis buffer (50 mM Tris pH 7.4, 150 mM NaCl, 1% NP-40, 0.5% sodium
1175 deoxycholate, 0.1% SDS, 1 mM PMSF, 2 μ g/mL aprotinin, 2 μ g/mL leupeptin) on ice.
1176 Lysates were spun at 20,800 g for 20 min, after which supernatants were collected, mixed

1177 with SDS-PAGE sample buffer, and boiled at 95°C for 5 min. Samples were run on a 10%
1178 polyacrylamide gel and subsequently transferred onto nitrocellulose membranes (Bio-
1179 Rad). Membranes were blocked for 1 h in 5% skim milk powder in TBST (TBS with
1180 0.0025% Tween-20), before incubation with either mouse anti-gamma actin antibody
1181 (Bio-Rad, Cat#MCA5776GA; dilution 1:200), mouse anti-beta actin antibody (Bio-Rad,
1182 Cat#MCA5775GA; dilution 1:200), or mouse anti-acetylated alpha tubulin antibody (Santa
1183 Cruz, Cat#sc-23950; dilution 1:2000) for 1 h. Following secondary antibody incubation,
1184 membranes were developed with chemiluminescent solutions (Thermo) for 1-2 min at
1185 room temperature and visualized using a Bio-Rad MP Imager (Bio-Rad).

1186

1187 **Multinucleation and mitotic staging assays**

1188 Stable iGFP-actin HeLa cells were seeded onto glass coverslips in 6-well dishes. At
1189 roughly 40% confluency, cells were transfected with 100 pmol of either control, beta, or
1190 gamma actin-targeting siRNA (Integrated DNA Technologies) with Lipofectamine 2000
1191 (Invitrogen) following manufacturer's instructions. Where indicated, 24 h post-transfection
1192 cells were induced to express either iGFP-beta or -gamma actin by the addition of 0.25
1193 µg/mL doxycycline. Cells were fixed 48 h post-transfection as described below. For
1194 multinucleation assays, cells were classified as either mono- or multi-nucleate by
1195 manually scoring the number of nuclei, as reported by Hoechst staining, within each cell
1196 boundary, as reported by acetylated alpha-tubulin staining, omitting cells fixed mid-
1197 division. For mitotic staging experiments, cells were manually classified as mitotic if the
1198 following features were observed: i) condensed chromosomes by Hoechst staining and/or
1199 b) an intercellular bridge as reported by acetylated alpha-tubulin staining. Early mitotic
1200 cells were further classified into either 'prophase' or 'metaphase' populations based on
1201 the organization of their condensed chromosomes, with 'metaphase' cells exhibiting
1202 sharp alignment with the metaphase plate, and 'prophase' cells exhibiting chromosomal
1203 rosettes or otherwise unaligned chromosomes. Data was entered into GraphPad Prism
1204 to generate bar graphs and perform statistical tests; the number of cells scored for each
1205 condition and details of statistical tests performed are described in the respective figure
1206 legends.

1207

1208 **Immunofluorescence**

1209 To visualize iGFP-tagged actins, HeLa cells were fixed with 3.7% paraformaldehyde in
1210 PHEM buffer (60 mM PIPES pH 7.0, 25 mM HEPES, 10 mM EGTA, 4 mM MgSO₄·7 H₂O)
1211 for 10 min at room temperature and permeabilized by 0.2% Triton-X-100 in PBS for 10
1212 min. Coverslips were blocked for 1 h in 3% BSA in PBS. Where indicated, iGFP-
1213 expressing cells were probed with anti-vinculin antibody (Sigma-Aldrich, Cat#V9131,
1214 1:100) for 16 h at 4°C. Coverslips were subsequently incubated with either Alexa 594 or
1215 Alexa 647 conjugated goat-anti mouse secondary antibody (Invitrogen, 1:400) for 1 h.
1216 For experiments visualizing endogenous beta actin and either iGFP gamma actin or
1217 vinculin, cells were fixed with 3.0% paraformaldehyde in PHEM buffer for 30 min at 37°C,
1218 followed by a second fixation for 5 min in -20°C methanol. Coverslips were blocked with
1219 3% BSA in PBS overnight at 4°C, before incubation for 1 h with mouse anti-beta actin
1220 antibody (Bio-Rad, Cat#MCA5775GA; dilution 1:600), either with or without anti-vinculin
1221 antibody (Sigma-Aldrich, Cat#V9131, 1:100), diluted in 1% BSA in PBS. Coverslips were

1222 subsequently incubated with either Alexa 594 or Alexa 647 conjugated goat-anti mouse
1223 secondary antibody (Invitrogen, 1:400) for 1 h.
1224 For multinucleation and mitotic staging experiments, cells were fixed with -20°C methanol
1225 for 10 min, blocked with 3% BSA in PBS, and subsequently stained with mouse anti-
1226 acetylated alpha tubulin antibody (Santa Cruz, sc-23950, 1:400) for 1 h. Coverslips were
1227 then incubated with Alexa 594 conjugated goat-anti mouse secondary antibody
1228 (Invitrogen, 1:400) for 1 h.
1229 Prior to mounting with Mowiol (Polyvinyl alcohol 4-88, Fluka), coverslips were incubated
1230 in 1 µg/mL Hoechst 33258 (Sigma) for 10 min and rinsed in ddH₂O. Cells were visualized
1231 with either a PerkinElmer UltraView spinning disk confocal scanner mounted on a Nikon
1232 TE2000-E with a 60x/1.4 NA oil-immersion objective lens and 1.515 immersion oil at room
1233 temperature or a Leica SP8 scanning confocal microscope with a 63x/1.4 NA oil-
1234 immersion objective lens and Leica Type F immersion oil. Images were acquired using
1235 METAMORPH software (v.7.7.0.0; Molecular Devices) driving an electron multiplying
1236 charge-coupled device (CCD) camera (ImagEM, Hamamatsu) or LAS-X software
1237 (v.1.4.4; Leica) driving HyD detectors. Z sections (0.2 µm apart) were acquired to produce
1238 a stack that was then imported into AutoQuant X3 (Media Cybernetics) for 3D
1239 deconvolution (5 iterations). Single Z-slices were generated in ImageJ (v2.1.0). Images
1240 were overlaid in Adobe Photoshop (v23.0.2) involving adjustments to brightness and
1241 contrast.

1242 **Characterization of fission yeast strains expressing actin organization reporters**

1243 **Generation of fission yeast strains**

1244 msfGFP-tagged actin organization reporters were expressed from the fission yeast *leu1+*
1245 locus under the control of the *cdc42+* promoter using the integrative vector pJK148
1246 (Keeney and Boeke, 1994). Briefly, around 500 bp from the *cdc42+* promoter were
1247 amplified by PCR and cloned into the pJK148 vector using the *SacI* and *XbaI* sites,
1248 creating pSRP12. The *adh1+* terminator was amplified by PCR and cloned into pSRP12
1249 using the *BamHI* and *Sall* sites, creating pSRP14. Finally, the fragments coding for each
1250 of the actin reporters fused to msfGFP were obtained by digestion with *NheI* and *BamHI*
1251 from the respective mammalian expression plasmids and cloned into pSRP14, between
1252 the *cdc42+* promoter and the *adh1+* terminator, creating the plasmids pSRP16 to
1253 pSRP23, respectively (see Table S1). All oligos used are listed in Table S2. Plasmids
1254 were linearized by *NruI* digestion, before transformation of a wild-type strain. Genetic
1255 crosses were performed to combine the actin reporter-expressing strains to strains
1256 expressing the proper marker to check cytokinesis dynamics, microtubule organization or
1257 to the profilin mutant thermosensitive strain, *cdc3-319* (see Table S3).

1258 **Microscopy and image analysis**

1259
1260 For imaging, fission yeast cells were grown at 28°C (32°C for cells shown in Figure S5A)
1261 in YE5S medium to exponential growth. For time-lapse imaging, 300 µL of early log-phase
1262 cell cultures were placed in a well from a µ-Slide 8 well (Ibidi, Cat#80821) previously
1263 coated with 10 µL of 500 µg/mL soybean lectin (Sigma-Aldrich, Cat#L1395). Cells were
1264 left for 1 min to attach to the bottom of the well and culture media was removed carefully.
1265 Then, cells were washed three times with the same media and finally 300 µL of fresh
1266

1267 media were added (Cortes et al., 2012), before incubation in the microscope chamber at
1268 the same temperature at which cells had been cultured.

1269 Time-lapse images shown in Figure 5A are maximum intensity projections obtained from
1270 z-stacks of 7 slices at 1 μm interval every 2 minutes, acquired using an Olympus IX81
1271 spinning disk confocal microscope with Roper technology controlled by Metamorph 7.7
1272 software (Molecular Devices), equipped with a 100X/1.40 Plan Apo oil lens, a Yokogawa
1273 confocal unit, an EVOLVE CCD camera (Photometrics) and a laser bench with 491-561
1274 nm diode. Exposure time for green or red channels was 0.5 s.

1275 Time-lapse images shown in Figure S5A are maximum intensity projections obtained from
1276 z-stacks of 7 slices at 0.3 μm interval every 6 minutes, acquired using a Dragonfly 200
1277 Nikon Ti2-E spinning disk confocal microscope controlled by Fusion software (Andor),
1278 equipped with a 100X/1.45 Plan Apo oil lens, an Andor confocal unit, an sCMOS Sona
1279 4.2B-11 camera (Andor) and a laser bench with 405-561 nm diode (Andor). Exposure
1280 time was 0.3 s for the green channel and 0.2 s for the red channel. Microscopy images
1281 shown in Figure S5B are maximum intensity projections obtained from z-stacks of 7 slices
1282 at 0.3 μm interval, acquired using the same microscope setup from Nikon. Exposure time
1283 was 0.35 s. For the sake of comparison, images in Figure S5A and S5B are displayed
1284 using the same intensity range with Metamorph 7.7.

1285 Quantification of the time for acto-myosin ring assembly, maturation and constriction was
1286 performed by analyzing the time between the initial recruitment of myosin cortical nodes
1287 and their compaction into a tight ring, the time until the ring starts to constrict and the time
1288 until the myosin signal disappears after final constriction, respectively. Scatter dot plots
1289 of the measured times were prepared with GraphPad Prism. The number of cells used
1290 for each strain, the mean measured times and the statistical test used to evaluate
1291 differences, the latter performed with GraphPad Prism, are indicated in the respective
1292 legend. Actin patch and actin cable number per cell were quantified from maximum
1293 intensity projections obtained from z-stacks of 7 slices at 1 μm from cells in G2 phase
1294 (around 10 μm long). Scatter dot plots of the measured actin cables and patches were
1295 prepared with GraphPad Prism. The number of cells used for each strain and the mean
1296 numbers of cables and patches are indicated in the respective legend.

1297

1298 **Polarimetry measurements in the cytokinetic ring of live fission yeast**

1299 For live polarimetry measurements, strains co-expressing Af1, Af7, L1 or L22 and an
1300 mCherry-tubulin marker (strains SR3.51, SR3.54, SR3.57 and SR3.58 in Table S3) were
1301 incubated at 25°C in YE5S medium. 1 mL of exponentially growing cells were harvested
1302 by centrifugation for 60 s at 800 g, most of the supernatant was discarded and 1 mL of
1303 the cells was deposited onto a 2% YE5S agar pad at the center of a polydimethylsiloxane
1304 slide chamber prepared as described in (Costa et al., 2013).

1305 Three large field-of-view images (66 x 66 μm) typically containing 5-10 dividing cells per
1306 image, were collected for each strain. Before each polarimetry measurement, a two-color
1307 z stack was acquired ($\Delta z = 1.0 \mu\text{m}$) to image both GFP fusions and microtubules; the
1308 distribution of the latter was used in addition to the morphology of the actomyosin ring to
1309 confirm that cells were undergoing cytokinesis. A polarimetry stack using 18 polarization
1310 angles was then recorded for each position within a z stack ($\Delta z = 1.0 \mu\text{m}$) for the GFP
1311 channel, and thus allowed to obtain polarimetry images throughout the cytokinetic rings,
1312 containing both tangential-most views with the ring parallel to the xy plane, and more

1313 equatorial views showing cross-sections that appear as spots on either side of the ring.
1314 An exposure time of 0.5 s was used per polarized image. To minimize bias in the
1315 measured orientations due to the contribution of off-plane orientations we focused on the
1316 tangential-most views for the analysis (Figure 5E-G). One tangential view of the ring was
1317 analyzed per cell; in a few cells where both tangential views were present in the respective
1318 z planes, both were analyzed. Equatorial views were used for measuring the diameter of
1319 the constricting rings (Figure S5G).

1320 Polarimetry stack images were first processed with the open-source image processing
1321 software ImageJ/Fiji. Images within each polarimetry stack were registered using the
1322 StackReg plugin to correct for drift during the acquisition. The z planes containing the
1323 tangential-most views of the ring were identified for each cell. The pixels of the cytokinetic
1324 ring for analysis were selected by a combination of intensity thresholding and manual
1325 selection of the region to analyze. Each region of interest contained typically 40-80
1326 analyzed pixels i.e. 40–80 color-coded sticks in the tangential-most view of the cytokinetic
1327 ring per cell (Figure 5E-F). Analysis and data representation, including color-coded stick
1328 representations of the measured angles per pixel and polar histograms were done with
1329 PyPOLAR. The source code is available at <https://github.com/cchandre/Polarimetry.git>,
1330 and the desktop app can be freely obtained at <https://www.fresnel.fr/polarimetry> under a
1331 BSD license. GraphPad Prism was used to generate scatter plots of the quantified ψ
1332 angle distributions per strain; the number of cells measured for each strain, the respective
1333 median values and the statistical test used to evaluate differences are mentioned in the
1334 respective legend. Considering that Af7 and L22 dipoles are parallel to actin filaments, in
1335 order to assess the extent to which the measured actin filament orientations were more
1336 parallel or more perpendicular with respect to the ring axis, the ring axis angle in each
1337 cell was used as the reference angle in the "reference angle" tool in PyPOLAR to
1338 normalize the angle distributions from 0°–180° to 0°–90° and generate 0°–90° polar
1339 histograms, with 0° and 90° defining orientations parallel and perpendicular to the ring
1340 axis, respectively (Figure S5E-F).

1341

1342 **Characterization of *C. elegans* strains expressing actin organization reporters**

1343 **Plasmid construction for generation of transgenic animals**

1344 Sequences encoding actin organization reporters were codon optimised for optimal
1345 expression in the worms using the *C. elegans* codon adapter web tool (Redemann et al.,
1346 2011) and synthesized by GENEWIZ. Plasmids pFBR101, pFBR102 and pFBR105 (see
1347 Table S1) were constructed in two steps from pML36 (kind gift from Michel Labouesse
1348 lab), which contained a pCFJ151 backbone (ttTi5605 insertion homology arms) with a
1349 dpy-7 promoter for epidermal cell expression and a unc-54 3'UTR (universal 3'UTR for
1350 optimal expression). Briefly, the plasmid pML36 was opened and amplified by PCR using
1351 custom made oligos (Sigma-Aldrich). The sequences encoding organization reporters
1352 were also amplified by PCR and joined using overlapping ends into opened pML36
1353 plasmid using the NEBuilder HiFi DNA Assembly Cloning kit (New England Biolabs,
1354 Cat#E5520S). All PCR reactions were carried out by Phusion High-Fidelity DNA
1355 Polymerase (ThermoFisher Scientific, Cat#F531L). Primers were custom made by
1356 Sigma-Aldrich. The sequences of all oligos are listed in Table S2. The final plasmids were
1357 verified by DNA sequencing (Eurofins Genomics, Germany).

1358

1359 **Transgenic worm construction by MosSCI method**

1360 Worm MosSCI transgenesis was performed by direct microinjection as described in
1361 (Frokjaer-Jensen et al., 2008). Briefly, the injection mix was injected in the arm of both
1362 gonads in the young hermaphrodite animal of EG6699 strain. The injection mix contained
1363 a cocktail of pJL43.1 (50 ng/mL), pCJF90 (2.5 ng/mL), pCFJ104 (5 ng/mL), and an
1364 expression clone (50 ng/mL) in DNase/RNase-free water. All plasmids used for injection
1365 were purified by HiSpeed Plasmid Midi kit (Qiagen, Cat#12643). After injection, transgene
1366 insertion screening was performed as described at <http://www.wormbuilder.org>.
1367 Transgenic animals were verified by PCR genotyping and DNA sequencing.

1368

1369 **Worm embryonic growth and lethality tests**

1370 A few young hermaphrodite animals were picked and fed on freshly seeded Escherichia
1371 coli OP50 for 2h. After 2 h, all animals were transferred on fresh OP50 plates and laid
1372 eggs were counted. This process was redone until sufficient number (>1000) of embryos
1373 were achieved and counted. After 12-16 h, all previously scored embryo-containing plates
1374 were recounted for unhatched embryos (dead eggs) and hatched larvae. For this
1375 experiment, strains were grown at 20°C. The embryonic lethality for each strain, scored
1376 as the percentage of unhatched embryos, is shown in Figure 6A.

1377 Embryonic growth rate was measured by imaging embryos by differential interference
1378 contrast (DIC) microscopy on a Leica DM6000 microscope until they hatch as larvae.
1379 Briefly, embryos were collected by dissecting gravid hermaphrodites in M9 medium and
1380 mounted on a 5% agarose pad for imaging. Z-stack images were acquired with 40-50
1381 planes per embryo and a Δz interval of 1 μm , and with a 10 min interval for 12-14 h at
1382 20°C. Embryonic length was measured manually with the segmented line tool in the
1383 ImageJ/Fiji software and growth curves plotted with Microsoft Excel software (Figure 6B).
1384 The number of embryos measured for each strain is indicated in the respective legend.

1385

1386 **Polarimetry measurements in live *C. elegans* embryos**

1387 More than >30 young gravid hermaphrodite animals were picked and fed on freshly
1388 seeded OP50 *E. coli* overnight. Next day, mixed stage embryos were picked and mounted
1389 on a 5% agarose pad in M9 medium for imaging. Temporary hypoxic conditions were
1390 created by adding OP50 *E. coli*, preventing embryonic muscle activity that usually starts
1391 around 1.7-fold. Embryonic stages were evaluated by brightfield microscopy. Length
1392 measurements were subsequently performed using ImageJ/Fiji. Polarimetry stacks using
1393 18 polarization angles were recorded in the epidermis of 1.5-fold, 1.5-2-fold and >2-fold
1394 stage embryos. The pixels containing dorsal and ventral epidermal cells (DV cells) and
1395 seam cells were selected by a combination of intensity thresholding and manual selection
1396 of the region to analyze. Analysis and data representation, including color-coded stick
1397 representations of the measured angles per pixel and histograms were done with
1398 PyPOLAR. GraphPad Prism was used to generate scatter plots of the quantified ψ angle
1399 distributions per strain and per developmental stage; the number of embryos for each
1400 strain and for each stage and the respective median ψ values are mentioned in the
1401 respective legend. To assess how the measured actin filament orientations in DV and
1402 seam cells distribute with respect to the DV/seam boundary for each developmental
1403 stage, the ρ angle distributions were normalized with respect to the DV/seam boundary
1404 from 0°–180° to 0°–90° to generate 0°–90° polar histograms. The DV/seam boundary for

1405 each embryo was drawn manually with the freehand line selection tool or the elliptical
1406 selection tool in Fiji and converted to a mask which was then used with the "edge
1407 detection" tool in PyPOLAR to define the boundary as the reference for the normalization
1408 of the angles. Considering that Af7 and L22 dipoles are parallel to actin filaments and that
1409 L45 dipoles are perpendicular to actin filaments, the more perpendicular mean actin
1410 filament orientations are to the boundary, the closer the angle values are to 90° (for Af7
1411 and L22) or to 0° (for L45) (Figure 6F,H,J and Figure S6E,G).

1412 **Generation of *Drosophila* expressing selected actin organization reporters**

1413 ***Drosophila* transgenics**

1414 Selected actin organization reporters were subcloned into pUASp plasmids for generating
1415 *Drosophila* transgenics. The respective mammalian expression plasmids were used as
1416 templates to subclone the reporters into *KpnI/BamHI* linearized UASp vectors using
1417 seamless cloning (In-Fusion HD Cloning Plus Kit, Takara Bio, Cat#638910). All primers
1418 were Cloning Oligo synthesis and purification quality from Eurofins Genomics and are
1419 listed in Table S2. Restriction enzymes were FastDigest enzymes from Thermo Fisher
1420 Scientific. All plasmids were verified by sequencing (Eurofins Genomics) after each
1421 cloning step. Midipreps of each UASp construct DNA were sent to BestGene Inc.
1422 (California, USA) for injections into *D. melanogaster* w1118 embryos and generation of
1423 the transformants UASp–L22, UASp–L45, UASp–U20, and UASp–Af7 (see Key
1424 Resources Table and Table S1).

1425 **Preparation of live *Drosophila* embryos for polarimetry measurements**

1426 mat- α -tub–GAL4 females were crossed to UASp–Af7 males, and F2 embryos were
1427 collected and prepared for imaging following standard procedures (Mavrakakis, 2016).
1428 Briefly, F1 progeny was placed in embryo collection cages with fresh yeasted apple juice
1429 agar plates. For live imaging, cellularizing F2 embryos were dechorionated with 50%
1430 bleach, washed with water, transferred onto a heptane glue-coated round coverslip,
1431 covered with halocarbon oil 200 (Tebubio, Cat#25073) and mounted in an Attofluor cell
1432 chamber (ThermoFisher Scientific, Cat#A7816).

1433 **Polarimetry measurements in live cellularizing *Drosophila* embryos**

1434 Polarimetry stacks using 18 polarization angles were recorded in focal planes through
1435 actomyosin rings at the invaginating membrane front (Figure 7A) or in focal planes
1436 apicolaterally to the former through the basal adherens junctions (Figure 7B). An
1437 exposure time of 0.2 s was used per polarized image. The pixels of the actomyosin rings
1438 or basal adherens junctions for analysis were selected by a combination of intensity
1439 thresholding and manual selection of the region to analyze. Analysis and data
1440 representation, including color-coded stick representations of the measured angles per
1441 pixel and polar histograms were done with PyPOLAR. Considering that Af7 dipoles are
1442 parallel to actin filaments, in order to assess how the measured actin filament orientations
1443 distribute with respect to the actomyosin ring contour, the "edge detection" tool in
1444 PyPOLAR was used in combination with intensity thresholding to isolate the ring contour-
1445 associated pixels and normalize the angle distributions from 0°–180° to 0°–90° and
1446 generate 0°–90° polar histograms, with 0° and 90° defining orientations parallel and
1447 perpendicular to the ring contour, respectively (Figure S7A).

1451
1452 **Characterization of actin organization reporters in the *Drosophila* flight muscle**

1453 **Flight tests**

1454 Flight tests were performed as described in (Schnorrer et al., 2010). 3 to 7 day-old males
1455 were dropped into a 1 m long / 15 cm in diameter plexiglass cylinder with marked sections.
1456 Landing in the different sections depends on their flight ability, which was thereby scored
1457 (top 40-cm section: wild type, middle 40-cm section: impaired flight ("weak flier" in Figure
1458 7C), bottom 20-cm section: flightless) (see cartoon in Figure 7C). For each genotype,
1459 flight assays were performed three times with a minimum of ten males per assay. The
1460 total number of flies scored for each genotype is mentioned in the respective figure
1461 legend. GraphPad Prism was used to generate bar graphs of the quantified flight ability
1462 per genotype and the mean percentages are mentioned in the respective legend.

1463
1464 **Preparation of fixed adult flight muscles**

1465 Head, wings and abdomen were cut off the thorax of anaesthetized adult flies with fine
1466 scissors, and the thoraxes were fixed for 30 min in 4% paraformaldehyde in PBST (PBS
1467 + 0.3% Triton X-100). After three 10 min washes in PBST, thoraxes were placed on
1468 double-sided tape and cut sagittally dorsal to ventral with a microtome blade (Feather
1469 C35). The thorax halves were placed in PBST with Alexa 568-phalloidin (Invitrogen,
1470 1:500) and incubated overnight at 4°C on a shaker. Hemithoraxes were then washed 3
1471 times 10 min in PBST at room temperature and mounted in Vectashield with 2 spacer
1472 coverslips on each side.

1473
1474 **Preparation of live flight muscles**

1475 Flight muscles were dissected, mounted in Schneider medium (no fixation), and imaged
1476 within 30 min following dissection. After removal of the head, abdomen and wings, a first
1477 incision was performed through the cuticle with sharp forceps (Dumont #5 forceps, Fine
1478 Science Tools, Cat#11252-20) at the median plane. The thorax was then gently pulled
1479 open into two halves, which were then fully disconnected through cutting of the ventral
1480 connective tissues using fine dissection scissors (Fine Science Tools, Cat#15009-08).
1481 The dissection resulted in relatively intact flight muscles still attached to the tendon cells
1482 of the thorax. Samples were mounted in Schneider medium using two coverslip spacers
1483 and imaged immediately.

1484
1485 **Polarimetry measurements in live *Drosophila* flight muscle**

1486 The polarimetry analysis shown was from flight muscle expressing the reporters
1487 throughout muscle development with the Mef2-GAL4 driver apart from flight muscle
1488 expressing Af7, for which Af7 was expressed only transiently after muscle development
1489 with the tub-GAL80ts ; Mef2-GAL4 driver. One hemithorax per animal was used for
1490 polarimetry measurements, with 4-7 hemithoraces measured for each strain. Polarimetry
1491 stacks using 18 polarization angles were recorded in 1-7 different fields of view for each
1492 hemithorax. Ten myofibrils were analyzed per field of view (red-outlined boxes in Figure
1493 7E-G). The pixels containing individual myofibrils within each field of view were selected
1494 by a combination of intensity thresholding and manual selection of the region to analyze.
1495 Each myofibril contained typically 3,000-10,000 analyzed pixels. Analysis and data
1496 representation, including color-coded stick representations of the measured angles per

1497 pixel and histograms were done with PyPOLAR. The histograms shown in Figure 7E-G
1498 are from single myofibrils. GraphPad Prism was used to generate scatter plots of the
1499 quantified ψ angle distributions per strain; the number of myofibrils measured for each
1500 strain, the respective median values and the statistical test used to evaluate differences
1501 are mentioned in the respective legend.

1502

1503 **Characterization of actin organization reporters in the *Drosophila* wing**

1504 For wing analysis, we anesthetized 50 young adult males from the progeny (using CO₂)
1505 and removed one wing from each fly with fine tweezers. These wings were then directly
1506 mounted between a slide and a coverslip using UV-cured optical adhesive (Thorlabs,
1507 Cat#NOA63). Images of the wings were captured using a digital microscope (Dino-Lite).
1508 For wing size analysis, we utilized landmarks within the wing vein pattern to measure
1509 specific distances. For the long axis, we measured the distance between the proximal
1510 end of L5 and the distal end of L3, following the nomenclature from (De Celis, 2003). For
1511 the short axis, we measured the distance between the distal end of L5 and the intersection
1512 of the opposite side of the wing with a line perpendicular to the long axis, passing through
1513 the distal end of L5. These two distances are represented in Figure S7B. MATLAB was
1514 used to generate box plots of the quantified wing area. The number of wings for each
1515 genotype, the respective median values of L_L-L_S and the statistical test used to evaluate
1516 differences are mentioned in the respective legend.

1517

1518 **Protein structures and protein sequence alignments**

1519 Cartoon representations of protein structures were generated with the open-source
1520 software PyMOL (Schrödinger). The structure shown for cpGFP1-10/11 in Figure 1J
1521 corresponds to the structure of circularly permuted red fluorescent protein Kate (PDB
1522 3RWT) and is used to illustrate the design principle of our circularly permuted. The PDB
1523 IDs for the remaining structures are as follows: 2B3P (sfGFP, Figure 1F, J, K), 1GFL
1524 (wild-type GFP, Figure 1I), 7AD9 (Lifeact-F-actin complex, Figure S1C, D), 1QAG
1525 (Utrophin, Figure S2G), 4N6T (Adhiron/Affimer, Figure S3I) and 5JLF (F-actin-
1526 tropomyosin complex, Figure 4B). The structure of F-tractin (Figure S3E) was generated
1527 using the AlphaFold database at EMBL-EBI. The multiple sequence alignment of Lifeact
1528 sequences (Figure S1B) was generated with Clustal Omega (EMBL-EBI). Graphical
1529 representations illustrating the conservation of residues for Lifeact, F-tractin and G-actin
1530 (Figures S1B, S3D, 4C) were generated using the WebLogo application (University of
1531 California, Berkeley). Interface areas were analyzed using PISA calculations as
1532 implemented on the EMBL-EBI server and visually inspected using PyMOL.

1533

1534 **Polarimetry**

1535 **Optical setup**

1536 Fluorescence images were acquired with a confocal spinning disk unit (CSU-X1-M1,
1537 Yokogawa) connected to the side-port of an inverted microscope (Eclipse Ti2-E, Nikon)
1538 using a x2 magnifier (Yokogawa), a Nikon Plan Apo x100/1.45 NA oil immersion objective
1539 lens and an EMCCD camera with 1024x1024 pixels, 13x13 μ m pixel size (iXon Ultra 888,
1540 Andor) resulting in an image pixel size of 65 nm. Z-stacks were acquired using a piezo
1541 stage (P-736, PI). The lateral position of the sample was controlled with a translation
1542 piezo stage (U-780, PI). The spinning disk is equipped with a multiline dichroic mirror

1543 (Di01-T405/488/568/647-13x15x0.5, Semrock) and an emission filter wheel with filters
1544 adapted to the studied emission: band pass 540/80 for EGFP/sfGFP and AF488 (FF01-
1545 540/80-25, Semrock), band pass 593/46 for sfCherry2 (FF01-593/46-25, Semrock), and
1546 long pass 655 for SiR-actin (Et655lp, Chroma). The laser excitation is provided by
1547 polarized continuous lasers (488-, 561- and 641-nm laser lines, Sapphire, Coherent)
1548 combined with a set of dichroic mirrors, each of the laser being used separately with a
1549 power of typically 0.5 mW at the entrance of the spinning disk. The laser beams are sent
1550 into an electro-optic modulator (EOM) (Pockels cell, No 28-NP; Quantum Technology)
1551 followed by a quarter wave plate (WPQ05M-488; Thorlabs) to create a linear rotating
1552 polarization. The voltages sent to the Pockels cell to provide known polarization rotations
1553 are determined in a preliminary calibration step, using a polarimeter based on the quarter
1554 wave plate method, as described in (Wang et al., 2013). As the whole optical path involves
1555 reflections on mirrors and transmission through a dichroic mirror, the polarization after
1556 the Pockels cell system is likely to be deformed. Polarization distortion compensation of
1557 the spinning disk dichroic mirror is provided by placing an identical dichroic mirror (Di01-
1558 T405/488/568/647-13x15x0.5, Semrock) in the path of the laser line just after the quarter
1559 wave plate, such that s and p polarization components are exchanged at the first and
1560 second dichroic transmissions. This configuration ensures minimization of the
1561 polarization ellipticity and diattenuation produced by the dichroic mirror. The remaining
1562 distortions are characterized following the procedure of (Wang et al., 2013), using a
1563 polarimeter based on the quarter wave plate method. The beam is then expanded using
1564 a 10x telescope (BE10, Thorlabs) and sent directly to the microlens array of the CSU by
1565 reflection on a second entrance mirror. The microlens and pinhole arrays of the CSU
1566 disks rotate synchronously at a speed of 1,800 rpm, while the EMCCD and EOM are
1567 synchronized to ensure a fast stack recording for a given number of incident polarization
1568 (Wang et al., 2013). Exposure times are in the range of 0.1-0.5 s, and 18 polarization
1569 angles are typically measured per polarimetry stack, which leads to a few seconds per
1570 polarimetry stack.

1571

1572 **Signal processing**

1573 Fluorescence is generated from the coupling of fluorophore dipoles with the incident
1574 linearly polarized electric field denoted $E(\alpha)$, whose orientation is an angle α with the
1575 horizontal axis X of the sample plane. Inside the confocal volume, each fluorescent
1576 molecule exhibits an absorption dipole vector μ_{abs} with an orientation (θ, ϕ) in the
1577 macroscopic sample frame. The recorded fluorescence intensity from a single molecule
1578 is proportional to the absorption probability $P_{abs}(\theta, \phi) = |\mu_{abs}(\theta, \phi) \cdot E(\alpha)|^2$. The total
1579 intensity from an ensemble of molecules in the focal volume is therefore the sum of the
1580 intensities from all single molecules present in this volume, whose size is typically 300
1581 nm laterally and 600 nm longitudinally. This results in an averaged intensity: $I(\alpha) =$
1582 $\iint |\mu_{abs}(\theta, \phi) \cdot E(\alpha)|^2 \sin \theta d\theta d\phi$ (Kress et al., 2013). The intensity is thus maximized
1583 when the absorption dipoles of the molecules are aligned with the electric field. We
1584 assume that the orientations explored by molecular dipoles are constrained within an
1585 angular cone of total aperture angle ψ , oriented in the sample plane along the direction ρ
1586 relative to X , the horizontal axis of the sample plane. Physically, ψ is related to a
1587 « molecular order » quantity, which determines the degree of angular variations present
1588 within the focal spot at a given pixel position, averaged over time and space. Note that

1589 when fluorescent molecules are attached to actin with a degree of angular fluctuations
 1590 due to their linker to actin, ψ encompasses three contributions : (1) the mean tilt angle ξ
 1591 of the molecule with respect to the actin filament axis, (2) the angular fluctuations of the
 1592 molecule due to its linker flexibility, and (3) the static organization of the actin filaments.
 1593 The mean orientation ρ , on the other hand, determines the mean direction of the
 1594 molecules. Therefore when the molecules are attached to actin in a constrained manner
 1595 (i.e. angular fluctuations are not isotropic), in an assembly of aligned filaments, ρ can take
 1596 two values : either $\rho = 0^\circ$ when the tilt angle of the molecules ξ is close to the filament
 1597 axis with $\xi < 45^\circ$, or $\rho = 90^\circ$ when the molecules are away from the filament axis with ξ
 1598 $> 45^\circ$. Thus, the angles ρ and ψ quantify the full information on the molecular organization
 1599 at each pixel of an image. We note that the measurements performed in this work are
 1600 limited to a projection of the fluorophores' distribution in the sample plane, which is
 1601 imposed by the manipulation of light polarization in this plane. This 2D projection leads to
 1602 an overestimation of the order angle ψ when the cone distribution is tilted more than 45°
 1603 out of plane (Kress et al., 2013).

1604 The angles ρ and ψ are deduced from the measurement of the intensity modulation $I(\alpha)$,
 1605 which takes the form (Kress et al., 2013; Wang et al., 2013): $I(\alpha) = a_0 + a_2(\rho, \psi) \cos 2\alpha +$
 1606 $b_2(\rho, \psi) \sin 2\alpha$. The coefficients $a_2(\rho, \psi)$ and $b_2(\rho, \psi)$, which can be directly related to the
 1607 parameters (ρ, ψ) (see below), are deduced from the decomposition $I(\alpha)$ into circular
 1608 functions ($\cos 2\alpha, \sin 2\alpha$). In practice, when several input polarization angles α_k are used
 1609 in a polarimetry stack (typically, for 18 polarization angles, $\alpha_k = 0, 10^\circ, \dots, 170^\circ$), we use
 1610 the operations $a_2 = \frac{2}{a_0} \sum I(\alpha_k) \cos 2\alpha_k$ and $b_2 = \frac{2}{a_0} \sum I(\alpha_k) \sin 2\alpha_k$, using $a_0 = \sum I(\alpha_k)$.

1611 To retrieve the angular parameters (ρ, ψ) from the measured quantities $a_2(\rho, \psi)$ and
 1612 $b_2(\rho, \psi)$, the following method is used to account for polarization distortions (Kress et al.,
 1613 2013): The presence of polarization distortions is modelled in the intensity equation
 1614 $I(\alpha) = \iint |\mu_{abs}(\theta, \phi) \cdot E(\alpha)|^2 \sin \theta d\theta d\phi$ by including a distorted $E(\alpha) =$
 1615 $(\cos \alpha, \gamma \sin \alpha e^{i\delta})$, with γ a diattenuation factor, which produces an energy loss between
 1616 the s and p polarization components of an electric field, and δ a birefringence factor,
 1617 which produces a phase difference between the s and p components. In this model, the
 1618 polarization distortions are supposed to originate from an equivalent phase plate whose
 1619 axes coincide with the horizontal and vertical directions of the sample, which is
 1620 reasonable considering that all reflections in the optical path involve s and p directions
 1621 along these axes. Including these distortions allows the construction of a map of the
 1622 dependence of both a_2 and b_2 parameters, as functions of (ρ, ψ) . Without any distortions,
 1623 these maps take the form of disks from which (ρ, ψ) can be unambiguously determined
 1624 by the one-to-one relationship between (ρ, ψ) and (a_2, b_2) (Kress et al., 2013). In the
 1625 presence of distortions, the disks are deformed but the relation stays unambiguous,
 1626 therefore it is possible to find (ρ, ψ) from the measurement of (a_2, b_2) , using a
 1627 minimization method in the $(\rho, \psi) vs (a_2, b_2)$ lookup table for instance. Finally, the
 1628 parameters (ρ, ψ) extracted from the $(\rho, \psi) vs (a_2, b_2)$ disk analysis are represented in a
 1629 single polarimetry image that combines molecular order and orientation, superimposed
 1630 to the fluorescence intensity image built from the total intensity $\sum I(\alpha_k)$.

1631 In experimental measurements, the $I(\alpha)$ modulation is affected by noise, which impacts
 1632 the determination of the (ρ, ψ) parameters. The precision on the determination of (ρ, ψ)
 1633 increases as the inverse square of the total intensity. It has been shown that above 5000

1634 photons per pixel (which is typically the case for GFP imaging), the precision reaches
1635 about 1° for ρ and 3° for ψ , except at extreme high-order conditions ($\psi \sim 0^\circ$) where the
1636 precision in ψ reaches 5° (Kress et al., 2013).

1637 We note that the reasoning for the dependence of absorption probability on the
1638 fluorophore dipole orientation is similar to that for the dependence of emission probability:
1639 the polarized emission scheme exploited in fluorescence anisotropy and polarization
1640 emission analysis (Chen et al., 2020; Forkey et al., 2000) is not exploited in this study,
1641 but could be similarly applied (Kampmann et al., 2011; Mattheyses et al., 2010; Mehta et
1642 al., 2016; Nordenfelt et al., 2017; Swaminathan et al., 2017; Vrabioiu and Mitchison,
1643 2006). Finally, the angle ψ used in this work can also be directly related to other quantities
1644 used to define molecular orientational organization, in particular the generic, distribution-
1645 independent order parameter used in aligned structures such as lipid membranes and
1646 liquid-crystalline polymers (Jahnig, 1979).

1647

1648 **QUANTIFICATION AND STATISTICAL ANALYSIS**

1649 The quantification method for each experiment is described in the respective method
1650 details section. The statistical details of the experiments, including the exact value of n
1651 and what n represents, the definition of center, dispersion and precision measures (mean,
1652 median, SD, SEM) in the plots and graphs, the software and statistical test used to
1653 evaluate statistical significance of differences, and the definition of statistical significance
1654 are mentioned in the method details sections and respective Figure legends.

1655

1656

1657 **REFERENCES**

1658

1659 Abrahamsson, S., McQuilken, M., Mehta, S.B., Verma, A., Larsch, J., Ilic, R., Heintzmann, R., Bargmann,
1660 C.I., Gladfelter, A.S., and Oldenbourg, R. (2015). MultiFocus Polarization Microscope (MF-PolScope) for
1661 3D polarization imaging of up to 25 focal planes simultaneously. *Opt Express* **23**, 7734-7754.

1662 Akemann, W., Raj, C.D., and Knöpfel, T. (2001). Functional characterization of permuted enhanced green
1663 fluorescent proteins comprising varying linker peptides. *Photochem Photobiol* **74**, 356-363.

1664 Andresen, M., Schmitz-Salue, R., and Jakobs, S. (2004). Short tetracysteine tags to beta-tubulin
1665 demonstrate the significance of small labels for live cell imaging. *Mol Biol Cell* **15**, 5616-5622.

1666 Bahler, J., Wu, J.Q., Longtine, M.S., Shah, N.G., McKenzie, A., 3rd, Steever, A.B., Wach, A., Philippsen,
1667 P., and Pringle, J.R. (1998). Heterologous modules for efficient and versatile PCR-based gene targeting in
1668 *Schizosaccharomyces pombe*. *Yeast* **14**, 943-951.

1669 Baird, G.S., Zacharias, D.A., and Tsien, R.Y. (1999). Circular permutation and receptor insertion within
1670 green fluorescent proteins. *Proc Natl Acad Sci USA* **96**, 11241-11246.

1671 Ballestrem, C., Wehrle-Haller, B., and Imhof, B.A. (1998). Actin dynamics in living mammalian cells. *J Cell*
1672 *Sci* **111** (Pt 12), 1649-1658.

1673 Barak, L.S., Yocum, R.R., Nothnagel, E.A., and Webb, W.W. (1980). Fluorescence staining of the actin
1674 cytoskeleton in living cells with 7-nitrobenz-2-oxa-1,3-diazole-phalloidin. *Proc Natl Acad Sci U S A* **77**,
1675 980-984.

1676 Baranwal, S., Naydenov, N.G., Harris, G., Dugina, V., Morgan, K.G., Chaponnier, C., and Ivanov, A.I.
1677 (2012). Nonredundant roles of cytoplasmic beta- and gamma-actin isoforms in regulation of epithelial apical
1678 junctions. *Mol Biol Cell* **23**, 3542-3553.

1679 Belin, B.J., Cimini, B.A., Blackburn, E.H., and Mullins, R.D. (2013). Visualization of actin filaments and
1680 monomers in somatic cell nuclei. *Mol Biol Cell* **24**, 982-994.

1681 Belin, B.J., Goins, L.M., and Mullins, R.D. (2014). Comparative analysis of tools for live cell imaging of actin
1682 network architecture. *Bioarchitecture* **4**, 189-202.

1683 Belyy, A., Merino, F., Sitsel, O., and Raunser, S. (2020). Structure of the Lifeact-F-actin complex. *PLoS*
1684 *Biol* **18**, e3000925.

1685 Bendezu, F.O., Hale, C.A., Bernhardt, T.G., and de Boer, P.A. (2009). RodZ (YfgA) is required for proper
1686 assembly of the MreB actin cytoskeleton and cell shape in *E. coli*. *EMBO J* **28**, 193-204.

1687 Bendezu, F.O., Vincenzetti, V., Vavylonis, D., Wyss, R., Vogel, H., and Martin, S.G. (2015). Spontaneous
1688 Cdc42 polarization independent of GDI-mediated extraction and actin-based trafficking. *PLoS Biol* 13,
1689 e1002097.

1690 Benninger, R.K., Onfelt, B., Neil, M.A., Davis, D.M., and French, P.M. (2005). Fluorescence imaging of two-
1691 photon linear dichroism: cholesterol depletion disrupts molecular orientation in cell membranes. *Biophys J*
1692 88, 609-622.

1693 Blanchoin, L., Boujemaa-Paterski, R., Sykes, C., and Plastino, J. (2014). Actin dynamics, architecture, and
1694 mechanics in cell motility. *Physiol Rev* 94, 235-263.

1695 Brasselet, S., and Alonso, M.A. (2023). Polarization microscopy: from ensemble structural imaging to
1696 single-molecule 3D orientation and localization microscopy. *Optica* 10, 1486-1510.

1697 Brasselet, S., Ferrand, P., Kress, A., Wang, X., Ranchon, H., and Gasecka, A. (2013). Imaging Molecular
1698 Order in Cell Membranes by Polarization-Resolved Fluorescence Microscopy. In *Fluorescent Methods to
1699 Study Biological Membranes*, Y.M.a.G. Duportail, ed. (Springer-Verlag Berlin Heidelberg), pp. 311-338

1700 Brault, V., Sauder, U., Reedy, M.C., Aebi, U., and Schoenenberger, C.A. (1999). Differential epitope tagging
1701 of actin in transformed *Drosophila* produces distinct effects on myofibril assembly and function of the
1702 indirect flight muscle. *Mol Biol Cell* 10, 135-149.

1703 Brenner, S. (1974). The genetics of *Caenorhabditis elegans*. *Genetics* 77, 71-94.

1704 Bubb, M.R., Senderowicz, A.M., Sausville, E.A., Duncan, K.L., and Korn, E.D. (1994). Jasplakinolide, a
1705 cytotoxic natural product, induces actin polymerization and competitively inhibits the binding of phalloidin
1706 to F-actin. *J Biol Chem* 269, 14869-14871.

1707 Burkel, B.M., von Dassow, G., and Bement, W.M. (2007). Versatile fluorescent probes for actin filaments
1708 based on the actin-binding domain of utrophin. *Cell Motil Cytoskeleton* 64, 822-832.

1709 Cabantous, S., Terwilliger, T.C., and Waldo, G.S. (2005). Protein tagging and detection with engineered
1710 self-assembling fragments of green fluorescent protein. *Nat Biotechnol* 23, 102-107.

1711 Carlson, H.J., Cotton, D.W., and Campbell, R.E. (2010). Circularly permuted monomeric red fluorescent
1712 proteins with new termini in the beta-sheet. *Protein Sci* 19, 1490-1499.

1713 Chakraborty, S., Jasnin, M., and Baumeister, W. (2020). Three-dimensional organization of the
1714 cytoskeleton: A cryo-electron tomography perspective. *Protein Sci* 29, 1302-1320.

1715 Chen, A., Arora, P.D., McCulloch, C.A., and Wilde, A. (2017). Cytokinesis requires localized beta-actin
1716 filament production by an actin isoform specific nucleator. *Nat Commun* 8, 1530.

1717 Chen, L., Chen, X., Yang, X., He, C., Wang, M., Xi, P., and Gao, J. (2020). Advances of super-resolution
1718 fluorescence polarization microscopy and its applications in life sciences. *Comput Struct Biotechnol J* 18,
1719 2209-2216.

1720 Chen, Q., Nag, S., and Pollard, T.D. (2012). Formins filter modified actin subunits during processive
1721 elongation. *J Struct Biol* 177, 32-39.

1722 Choidas, A., Jungbluth, A., Sechi, A., Murphy, J., Ullrich, A., and Marriott, G. (1998). The suitability and
1723 application of a GFP-actin fusion protein for long-term imaging of the organization and dynamics of the
1724 cytoskeleton in mammalian cells. *Eur J Cell Biol* 77, 81-90.

1725 Chugh, P., and Paluch, E.K. (2018). The actin cortex at a glance. *J Cell Sci* 131.

1726 Cortes, J.C., Sato, M., Munoz, J., Moreno, M.B., Clemente-Ramos, J.A., Ramos, M., Okada, H., Osumi,
1727 M., Duran, A., and Ribas, J.C. (2012). Fission yeast Ags1 confers the essential septum strength needed
1728 for safe gradual cell abscission. *J Cell Biol* 198, 637-656.

1729 Costa, J., Fu, C., Syrovatkina, V., and Tran, P.T. (2013). Imaging individual spindle microtubule dynamics
1730 in fission yeast. *Methods Cell Biol* 115, 385-394.

1731 Costantini, L.M., Fossati, M., Francolini, M., and Snapp, E.L. (2012). Assessing the tendency of fluorescent
1732 proteins to oligomerize under physiologic conditions. *Traffic* 13, 643-649.

1733 Courtemanche, N., Pollard, T.D., and Chen, Q. (2016). Avoiding artefacts when counting polymerized actin
1734 in live cells with LifeAct fused to fluorescent proteins. *Nat Cell Biol* 18, 676-683.

1735 Cramer, L.P. (1999). Role of actin-filament disassembly in lamellipodium protrusion in motile cells revealed
1736 using the drug jasplakinolide. *Curr Biol* 9, 1095-1105.

1737 Cranfill, P.J., Sell, B.R., Baird, M.A., Allen, J.R., Lavagnino, Z., de Gruiter, H.M., Kremers, G.J., Davidson,
1738 M.W., Ustione, A., and Piston, D.W. (2016). Quantitative assessment of fluorescent proteins. *Nat Methods*
1739 13, 557-562.

1740 Dancker, P., Low, I., Hasselbach, W., and Wieland, T. (1975). Interaction of actin with phalloidin:
1741 polymerization and stabilization of F-actin. *Biochim Biophys Acta* 400, 407-414.

1742 De Celis, J.F. (2003). Pattern formation in the *Drosophila* wing: The development of the veins. *Bioessays*
1743 25, 443-451.

1744 DeMay, B.S., Bai, X.B., Howard, L., Occhipinti, P., Meseroll, R.A., Spiliotis, E.T., Oldenbourg, R., and
1745 Gladfelter, A.S. (2011a). Septin filaments exhibit a dynamic, paired organization that is conserved from
1746 yeast to mammals. *Journal of Cell Biology* 193, 1065-1081.

1747 DeMay, B.S., Noda, N., Gladfelter, A.S., and Oldenbourg, R. (2011b). Rapid and quantitative imaging of
1748 excitation polarized fluorescence reveals ordered septin dynamics in live yeast. *Biophys J* 101, 985-994.

1749 Dopf, J., and Horiagon, T.M. (1996). Deletion mapping of the *Aequorea victoria* green fluorescent protein.
1750 *Gene* 173, 39-44.

1751 Doyle, T., and Botstein, D. (1996). Movement of yeast cortical actin cytoskeleton visualized in vivo. *Proc*
1752 *Natl Acad Sci U S A* 93, 3886-3891.

1753 Dugina, V., Zwaenepoel, I., Gabbiani, G., Clement, S., and Chaponnier, C. (2009). Beta and gamma-
1754 cytoplasmic actins display distinct distribution and functional diversity. *J Cell Sci* 122, 2980-2988.

1755 Edwards, K.A., Demsky, M., Montague, R.A., Weymouth, N., and Kiehart, D.P. (1997). GFP-moesin
1756 illuminates actin cytoskeleton dynamics in living tissue and demonstrates cell shape changes during
1757 morphogenesis in *Drosophila*. *Dev Biol* 191, 103-117.

1758 Eltzner, B., Hauke, L., Huckemann, S., Rehfeldt, F., and Wollnik, C. (2020). A Statistical and Biophysical
1759 Toolbox to Elucidate Structure and Formation of Stress Fibers. *Top Appl Phys* 134, 263-282.

1760 Feng, S., Sekine, S., Pessino, V., Li, H., Leonetti, M.D., and Huang, B. (2017). Improved split fluorescent
1761 proteins for endogenous protein labeling. *Nat Commun* 8, 370.

1762 Ferrand, P., Gasecka, P., Kress, A., Wang, X., Bioud, F.Z., Duboisset, J., and Brasselet, S. (2014). Ultimate
1763 use of two-photon fluorescence microscopy to map orientational behavior of fluorophores. *Biophys J* 106,
1764 2330-2339.

1765 Fletcher, D.A., and Mullins, R.D. (2010). Cell mechanics and the cytoskeleton. *Nature* 463, 485-492.

1766 Forkey, J.N., Quinlan, M.E., and Goldman, Y.E. (2000). Protein structural dynamics by single-molecule
1767 fluorescence polarization. *Prog Biophys Mol Biol* 74, 1-35.

1768 Frokjaer-Jensen, C., Davis, M.W., Hopkins, C.E., Newman, B.J., Thummel, J.M., Olesen, S.P., Grunnet,
1769 M., and Jorgensen, E.M. (2008). Single-copy insertion of transgenes in *Caenorhabditis elegans*. *Nat Genet*
1770 40, 1375-1383.

1771 Gally, C., Wissler, F., Zahreddine, H., Quintin, S., Landmann, F., and Labouesse, M. (2009). Myosin II
1772 regulation during *C. elegans* embryonic elongation: LET-502/ROCK, MRCK-1 and PAK-1, three kinases
1773 with different roles. *Development* 136, 3109-3119.

1774 Gasecka, A., Han, T.J., Favard, C., Cho, B.R., and Brasselet, S. (2009). Quantitative imaging of molecular
1775 order in lipid membranes using two-photon fluorescence polarimetry. *Biophys J* 97, 2854-2862.

1776 Gayrard, C., and Borghi, N. (2016). FRET-based Molecular Tension Microscopy. *Methods* 94, 33-42.

1777 Griffin, B.A., Adams, S.R., and Tsien, R.Y. (1998). Specific covalent labeling of recombinant protein
1778 molecules inside live cells. *Science* 281, 269-272.

1779 Hafi, N., Grunwald, M., van den Heuvel, L.S., Aspelmeier, T., Chen, J.H., Zagrebelsky, M., Schutte, O.M.,
1780 Steinem, C., Korte, M., Munk, A., *et al.* (2014). Fluorescence nanoscopy by polarization modulation and
1781 polarization angle narrowing. *Nat Methods* 11, 579-584.

1782 Heisenberg, C.P., and Bellaiche, Y. (2013). Forces in tissue morphogenesis and patterning. *Cell* 153, 948-
1783 962.

1784 Heuser, J.E., and Kirschner, M.W. (1980). Filament organization revealed in platinum replicas of freeze-
1785 dried cytoskeletons. *J Cell Biol* 86, 212-234.

1786 Hochbaum, D., Ferguson, A.A., and Fisher, A.L. (2010). Generation of transgenic *C. elegans* by biolistic
1787 transformation. *J Vis Exp*.

1788 Huang, J.Q., Huang, Y.Y., Yu, H.C., Subramanian, D., Padmanabhan, A., Thadani, R., Tao, Y.Q., Tang,
1789 X., Wedlich-Soldner, R., and Balasubramanian, M.K. (2012). Nonmedially assembled F-actin cables
1790 incorporate into the actomyosin ring in fission yeast. *Journal of Cell Biology* 199, 831-847.

1791 Hunter, C., and Wieschaus, E. (2000). Regulated expression of *nullo* is required for the formation of distinct
1792 apical and basal adherens junctions in the *Drosophila* blastoderm. *J Cell Biol* 150, 391-401.

1793 Jahrig, F. (1979). Structural order of lipids and proteins in membranes: evaluation of fluorescence
1794 anisotropy data. *Proc Natl Acad Sci U S A* 76, 6361-6365.

1795 Johnson, H.W., and Schell, M.J. (2009). Neuronal IP3 3-kinase is an F-actin-bundling protein: role in
1796 dendritic targeting and regulation of spine morphology. *Mol Biol Cell* 20, 5166-5180.

1797 Juanes, M.A., Isnardon, D., Badache, A., Brasselet, S., Mavrakis, M., and Goode, B.L. (2019). The role of
1798 APC-mediated actin assembly in microtubule capture and focal adhesion turnover. *J Cell Biol* 218, 3415-
1799 3435.

1800 Kampmann, M., Atkinson, C.E., Mattheyses, A.L., and Simon, S.M. (2011). Mapping the orientation of
1801 nuclear pore proteins in living cells with polarized fluorescence microscopy. *Nat Struct Mol Biol* 18, 643-
1802 649.

1803 Keeney, J.B., and Boeke, J.D. (1994). Efficient Targeted Integration at *Leu1-32* and *Ura4-294* in
1804 *Schizosaccharomyces-Pombe*. *Genetics* 136, 849-856.

1805 Keep, N.H., Winder, S.J., Moores, C.A., Walke, S., Norwood, F.L., and Kendrick-Jones, J. (1999). Crystal
1806 structure of the actin-binding region of utrophin reveals a head-to-tail dimer. *Structure* 7, 1539-1546.

1807 Kim, H.K., and Kaang, B.K. (1998). Truncated green fluorescent protein mutants and their expression in
1808 neurons. *Brain Res Bull* 47, 35-41.

1809 Kokai, E., Beck, H., Weissbach, J., Arnold, F., Sinske, D., Sebert, U., Gaiselmann, G., Schmidt, V., Walther,
1810 P., Munch, J., *et al.* (2014). Analysis of nuclear actin by overexpression of wild-type and actin mutant
1811 proteins. *Histochem Cell Biol* 141, 123-135.

1812 Kress, A., Ferrand, P., Rigneault, H., Trombik, T., He, H.T., Marguet, D., and Brasselet, S. (2011). Probing
1813 orientational behavior of MHC class I protein and lipid probes in cell membranes by fluorescence
1814 polarization-resolved imaging. *Biophys J* 101, 468-476.

1815 Kress, A., Wang, X., Ranchon, H., Savatier, J., Rigneault, H., Ferrand, P., and Brasselet, S. (2013).
1816 Mapping the local organization of cell membranes using excitation-polarization-resolved confocal
1817 fluorescence microscopy. *Biophys J* 105, 127-136.

1818 Kumari, A., Kesarwani, S., Javoor, M.G., Vinothkumar, K.R., and Sirajuddin, M. (2020). Structural insights
1819 into actin filament recognition by commonly used cellular actin markers. *EMBO J* 39, e104006.

1820 Lamm, N., Read, M.N., Nobis, M., Van Ly, D., Page, S.G., Masamsetti, V.P., Timpson, P., Biro, M., and
1821 Cesare, A.J. (2020). Nuclear F-actin counteracts nuclear deformation and promotes fork repair during
1822 replication stress. *Nat Cell Biol* 22, 1460-1470.

1823 Lappalainen, P., Kotila, T., Jegou, A., and Romet-Lemonne, G. (2022). Biochemical and mechanical
1824 regulation of actin dynamics. *Nat Rev Mol Cell Biol* 23, 836-852.

1825 Lawson, C.D., Peel, S., Jayo, A., Corrigan, A., Iyer, P., Baxter Dalrymple, M., Marsh, R.J., Cox, S., Van
1826 Audenhove, I., Gettemans, J., *et al.* (2022). Nuclear fascin regulates cancer cell survival. *Elife* 11.

1827 Lazar, J., Bondar, A., Timr, S., and Firestein, S.J. (2011). Two-photon polarization microscopy reveals
1828 protein structure and function. *Nat Methods* 8, 684-690.

1829 Li, X., Zhang, G., Ngo, N., Zhao, X., Kain, S.R., and Huang, C.C. (1997). Deletions of the *Aequorea victoria*
1830 green fluorescent protein define the minimal domain required for fluorescence. *J Biol Chem* 272, 28545-
1831 28549.

1832 Loison, O., Weitkunat, M., Kaya-Copur, A., Nascimento Alves, C., Matzat, T., Spletter, M.L., Luschnig, S.,
1833 Brasselet, S., Lenne, P.F., and Schnorrer, F. (2018). Polarization-resolved microscopy reveals a muscle
1834 myosin motor-independent mechanism of molecular actin ordering during sarcomere maturation. *PLoS Biol*
1835 16, e2004718.

1836 Lopata, A., Hughes, R., Tiede, C., Heissler, S.M., Sellers, J.R., Knight, P.J., Tomlinson, D., and Peckham,
1837 M. (2018). Affimer proteins for F-actin: novel affinity reagents that label F-actin in live and fixed cells. *Sci*
1838 *Rep* 8, 6572.

1839 Lukinavicius, G., Reymond, L., D'Este, E., Masharina, A., Gottfert, F., Ta, H., Guther, A., Fournier, M.,
1840 Rizzo, S., Waldmann, H., *et al.* (2014). Fluorogenic probes for live-cell imaging of the cytoskeleton. *Nat*
1841 *Methods* 11, 731-733.

1842 Madani, F., Lind, J., Damberg, P., Adams, S.R., Tsien, R.Y., and Graslund, A.O. (2009). Hairpin structure
1843 of a biarsenical-tetracysteine motif determined by NMR spectroscopy. *J Am Chem Soc* 131, 4613-4615.

1844 Martin, B.R., Giepmans, B.N., Adams, S.R., and Tsien, R.Y. (2005). Mammalian cell-based optimization of
1845 the biarsenical-binding tetracysteine motif for improved fluorescence and affinity. *Nat Biotechnol* 23, 1308-
1846 1314.

1847 Mattheyses, A.L., Kampmann, M., Atkinson, C.E., and Simon, S.M. (2010). Fluorescence anisotropy
1848 reveals order and disorder of protein domains in the nuclear pore complex. *Biophys J* 99, 1706-1717.

1849 Mavrakis, M. (2016). Visualizing septins in early *Drosophila* embryos. *Methods Cell Biol* 136, 183-198.

1850 Mavrakis, M., Azou-Gros, Y., Tsai, F.C., Alvarado, J., Bertin, A., Iv, F., Kress, A., Brasselet, S., Koenderink,
1851 G.H., and Lecuit, T. (2014). Septins promote F-actin ring formation by crosslinking actin filaments into
1852 curved bundles. *Nat Cell Biol* 16, 322-334.

1853 Mehta, S.B., McQuilken, M., La Riviere, P.J., Occhipinti, P., Verma, A., Oldenbourg, R., Gladfelter, A.S.,
1854 and Tani, T. (2016). Dissection of molecular assembly dynamics by tracking orientation and position of
1855 single molecules in live cells. *Proc Natl Acad Sci U S A* 113, E6352-E6361.

1856 Moores, C.A., and Kendrick-Jones, J. (2000). Biochemical characterisation of the actin-binding properties
1857 of utrophin. *Cell Motil Cytoskeleton* 46, 116-128.

1858 Moreno, S., Klar, A., and Nurse, P. (1991). Molecular genetic analysis of fission yeast
1859 *Schizosaccharomyces pombe*. *Methods Enzymol* 194, 795-823.

1860 Mullins, R.D., and Hansen, S.D. (2013). In vitro studies of actin filament and network dynamics. *Curr Opin*
1861 *Cell Biol* 25, 6-13.

1862 Nakai, N., Sato, K., Tani, T., Saito, K., Sato, F., and Terada, S. (2019). Genetically encoded orientation
1863 probes for F-actin for fluorescence polarization microscopy. *Microscopy (Oxf)* 68, 359-368.

1864 Nordenfelt, P., Moore, T.I., Mehta, S.B., Kalappurakkal, J.M., Swaminathan, V., Koga, N., Lambert, T.J.,
1865 Baker, D., Waters, J.C., Oldenbourg, R., *et al.* (2017). Direction of actin flow dictates integrin LFA-1
1866 orientation during leukocyte migration. *Nat Commun* 8, 2047.

1867 Ormo, M., Cubitt, A.B., Kallio, K., Gross, L.A., Tsien, R.Y., and Remington, S.J. (1996). Crystal structure of
1868 the *Aequorea victoria* green fluorescent protein. *Science* 273, 1392-1395.

1869 Osawa, M., and Erickson, H.P. (2005). Probing the domain structure of FtsZ by random truncation and
1870 insertion of GFP. *Microbiology (Reading)* 151, 4033-4043.

1871 Paluch, E., and Heisenberg, C.P. (2009). Biology and physics of cell shape changes in development. *Curr*
1872 *Biol* 19, R790-799.

1873 Pedelacq, J.D., Cabantous, S., Tran, T., Terwilliger, T.C., and Waldo, G.S. (2006). Engineering and
1874 characterization of a superfolder green fluorescent protein. *Nat Biotechnol* 24, 79-88.

1875 Pollard, T.D. (2016). Actin and Actin-Binding Proteins. *Cold Spring Harb Perspect Biol* 8.

1876 Pollard, T.D., and Cooper, J.A. (2009). Actin, a central player in cell shape and movement. *Science* 326, 1208-1212.

1877

1878 Priess, J.R., and Hirsh, D.I. (1986). *Caenorhabditis elegans* morphogenesis: the role of the cytoskeleton in

1879 elongation of the embryo. *Dev Biol* 117, 156-173.

1880 Raghunathan, G., Soundarajan, N., Sokalingam, S., Yun, H., and Lee, S.G. (2012). Deletional protein

1881 engineering based on stable fold. *PLoS One* 7, e51510.

1882 Redemann, S., Schloissnig, S., Ernst, S., Pozniakowsky, A., Ayloo, S., Hyman, A.A., and Bringmann, H.

1883 (2011). Codon adaptation-based control of protein expression in *C. elegans*. *Nat Methods* 8, 250-252.

1884 Renshaw, M.J., Liu, J., Lavoie, B.D., and Wilde, A. (2014). Anillin-dependent organization of septin

1885 filaments promotes intercellular bridge elongation and Chmp4B targeting to the abscission site. *Open Biol*

1886 4, 130190.

1887 Riedl, J., Crevenna, A.H., Kessenbrock, K., Yu, J.H., Neukirchen, D., Bista, M., Bradke, F., Jenne, D.,

1888 Holak, T.A., Werb, Z., *et al.* (2008). Lifeact: a versatile marker to visualize F-actin. *Nat Methods* 5, 605-607.

1889 Rimoli, C.V., Valades-Cruz, C.A., Curcio, V., Mavrakis, M., and Brasselet, S. (2022). 4polar-STORM

1890 polarized super-resolution imaging of actin filament organization in cells. *Nat Commun* 13, 301.

1891 Royant, A., and Noirclerc-Savoye, M. (2011). Stabilizing role of glutamic acid 222 in the structure of

1892 Enhanced Green Fluorescent Protein. *J Struct Biol* 174, 385-390.

1893 Schnorrer, F., Schonbauer, C., Langer, C.C., Dietzl, G., Novatchkova, M., Schernhuber, K., Fellner, M.,

1894 Azaryan, A., Radolf, M., Stark, A., *et al.* (2010). Systematic genetic analysis of muscle morphogenesis and

1895 function in *Drosophila*. *Nature* 464, 287-291.

1896 Shaner, N.C., Lin, M.Z., McKeown, M.R., Steinbach, P.A., Hazelwood, K.L., Davidson, M.W., and Tsien,

1897 R.Y. (2008). Improving the photostability of bright monomeric orange and red fluorescent proteins. *Nat*

1898 *Methods* 5, 545-551.

1899 Shum, M.S., Pasquier, E., Po'uha, S.T., O'Neill, G.M., Chaponnier, C., Gunning, P.W., and Kavallaris, M.

1900 (2011). gamma-Actin regulates cell migration and modulates the ROCK signaling pathway. *FASEB J* 25,

1901 4423-4433.

1902 Slocum, J.D., and Webb, L.J. (2017). A Double Decarboxylation in Superfolder Green Fluorescent Protein

1903 Leads to High Contrast Photoactivation. *J Phys Chem Lett* 8, 2862-2868.

1904 Spira, F., Cuylen-Haering, S., Mehta, S., Samwer, M., Reversat, A., Verma, A., Oldenbourg, R., Sixt, M.,

1905 and Gerlich, D.W. (2017). Cytokinesis in vertebrate cells initiates by contraction of an equatorial actomyosin

1906 network composed of randomly oriented filaments. *Elife* 6.

1907 Sugizaki, A., Sato, K., Chiba, K., Saito, K., Kawagishi, M., Tomabechi, Y., Mehta, S.B., Ishii, H., Sakai, N.,

1908 Shirouzu, M., *et al.* (2021). POLARIS, a versatile probe for molecular orientation, revealed actin filaments

1909 associated with microtubule asters in early embryos. *Proc Natl Acad Sci U S A* 118.

1910 Sund, S.E., Swanson, J.A., and Axelrod, D. (1999). Cell membrane orientation visualized by polarized total

1911 internal reflection fluorescence. *Biophys J* 77, 2266-2283.

1912 Svitkina, T.M., Verkhovsky, A.B., and Borisy, G.G. (1995). Improved procedures for electron microscopic

1913 visualization of the cytoskeleton of cultured cells. *J Struct Biol* 115, 290-303.

1914 Swaminathan, V., Kalappurakkal, J.M., Mehta, S.B., Nordenfelt, P., Moore, T.I., Koga, N., Baker, D.A.,

1915 Oldenbourg, R., Tani, T., Mayor, S., *et al.* (2017). Actin retrograde flow actively aligns and orients ligand-

1916 engaged integrins in focal adhesions. *Proc Natl Acad Sci U S A* 114, 10648-10653.

1917 Swulius, M.T., Nguyen, L.T., Ladinsky, M.S., Ortega, D.R., Aich, S., Mishra, M., and Jensen, G.J. (2018).

1918 Structure of the fission yeast actomyosin ring during constriction. *Proc Natl Acad Sci U S A* 115, E1455-

1919 E1464.

1920 Tiede, C., Tang, A.A., Deacon, S.E., Mandal, U., Nettleship, J.E., Owen, R.L., George, S.E., Harrison, D.J.,

1921 Owens, R.J., Tomlinson, D.C., *et al.* (2014). Adhiron: a stable and versatile peptide display scaffold for

1922 molecular recognition applications. *Protein Eng Des Sel* 27, 145-155.

1923 Topell, S., Hennecke, J., and Glockshuber, R. (1999). Circularly permuted variants of the green fluorescent

1924 protein. *FEBS Lett* 457, 283-289.

1925 Tsien, R.Y. (1998). The green fluorescent protein. *Annu Rev Biochem* 67, 509-544.

1926 Valades Cruz, C.A., Shaban, H.A., Kress, A., Bertaux, N., Monneret, S., Mavrakis, M., Savatier, J., and

1927 Brasselet, S. (2016). Quantitative nanoscale imaging of orientational order in biological filaments by

1928 polarized superresolution microscopy. *Proc Natl Acad Sci U S A* 113, E820-828.

1929 van den Ent, F., Amos, L.A., and Lowe, J. (2001). Prokaryotic origin of the actin cytoskeleton. *Nature* 413,

1930 39-44.

1931 Verkhusha, V.V., Tsukita, S., and Oda, H. (1999). Actin dynamics in lamellipodia of migrating border cells

1932 in the *Drosophila* ovary revealed by a GFP-actin fusion protein. *FEBS Lett* 445, 395-401.

1933 Vrbioiu, A.M., and Mitchison, T.J. (2006). Structural insights into yeast septin organization from polarized

1934 fluorescence microscopy. *Nature* 443, 466-469.

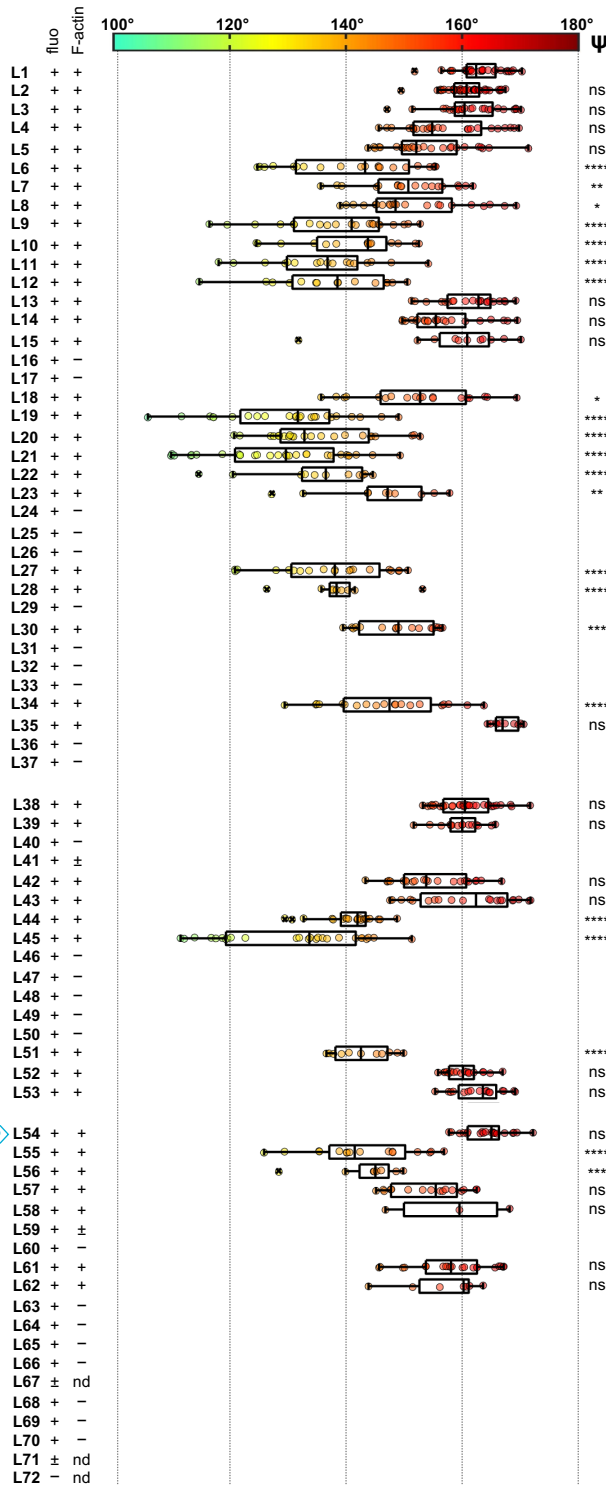
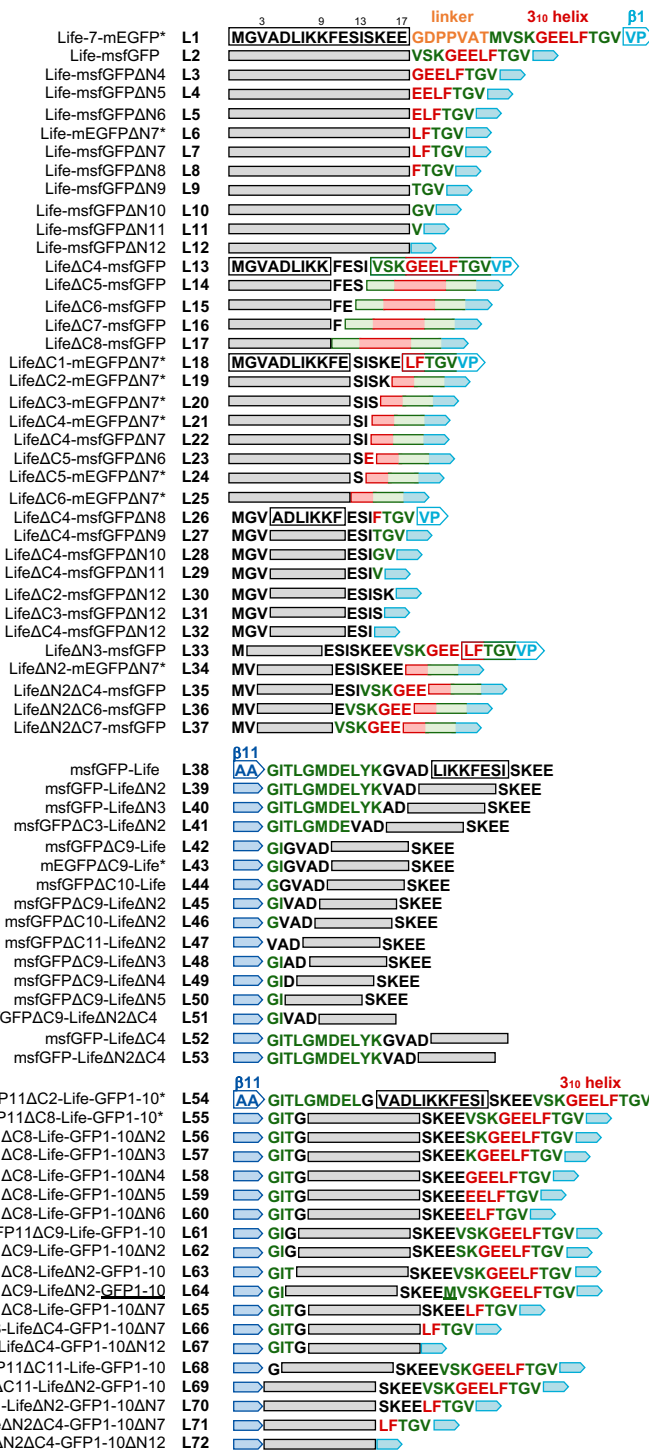
1935 Vuong-Brender, T.T., Ben Amar, M., Pontabry, J., and Labouesse, M. (2017). The interplay of stiffness and

1936 force anisotropies drives embryo elongation. *Elife* 6.

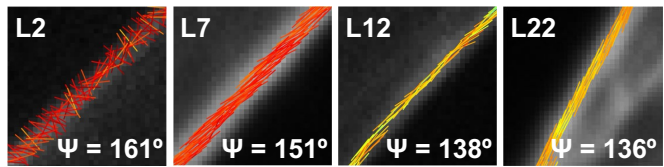
1937 Wang, X., Kress, A., Brasselet, S., and Ferrand, P. (2013). High frame-rate fluorescence confocal angle-
1938 resolved linear dichroism microscopy. *Rev Sci Instrum* 84, 053708.
1939 Watanabe, N., and Mitchison, T.J. (2002). Single-molecule speckle analysis of actin filament turnover in
1940 lamellipodia. *Science* 295, 1083-1086.
1941 Westphal, M., Jungbluth, A., Heidecker, M., Muhlbauer, B., Heizer, C., Schwartz, J.M., Marriott, G., and
1942 Gerisch, G. (1997). Microfilament dynamics during cell movement and chemotaxis monitored using a GFP-
1943 actin fusion protein. *Curr Biol* 7, 176-183.
1944 Wieland, T. (1977). Modification of actins by phallotoxins. *Naturwissenschaften* 64, 303-309.
1945 Wulf, E., Deboben, A., Bautz, F.A., Faulstich, H., and Wieland, T. (1979). Fluorescent phalloxin, a tool for
1946 the visualization of cellular actin. *Proc Natl Acad Sci U S A* 76, 4498-4502.
1947 Yang, F., Moss, L.G., and Phillips, G.N., Jr. (1996). The molecular structure of green fluorescent protein.
1948 *Nat Biotechnol* 14, 1246-1251.
1949 Yi, J., Wu, X.S., Crites, T., and Hammer, J.A., 3rd (2012). Actin retrograde flow and actomyosin II arc
1950 contraction drive receptor cluster dynamics at the immunological synapse in Jurkat T cells. *Mol Biol Cell*
1951 23, 834-852.
1952 Zacharias, D.A., Violin, J.D., Newton, A.C., and Tsien, R.Y. (2002). Partitioning of lipid-modified monomeric
1953 GFPs into membrane microdomains of live cells. *Science* 296, 913-916.
1954 Zhang, G., Gurtu, V., and Kain, S.R. (1996). An enhanced green fluorescent protein allows sensitive
1955 detection of gene transfer in mammalian cells. *Biochem Biophys Res Commun* 227, 707-711.
1956 Zhanghao, K., Chen, X., Liu, W., Li, M., Liu, Y., Wang, Y., Luo, S., Wang, X., Shan, C., Xie, H., *et al.* (2019).
1957 Super-resolution imaging of fluorescent dipoles via polarized structured illumination microscopy. *Nat*
1958 *Commun* 10, 4694.
1959

A

Lifeact



B



C

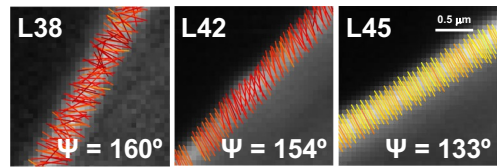
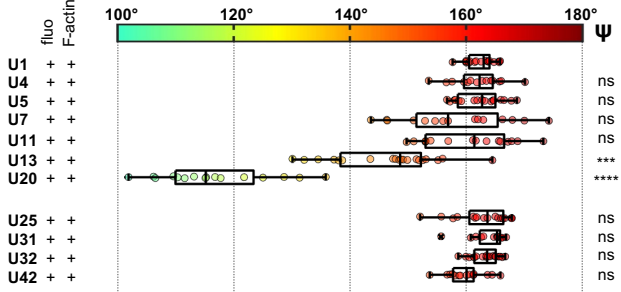
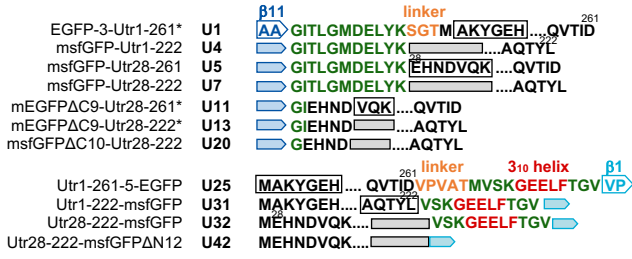
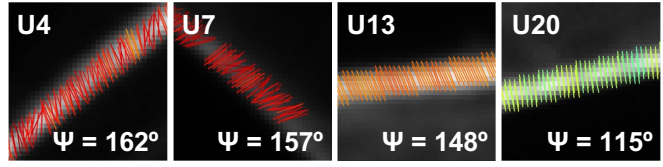
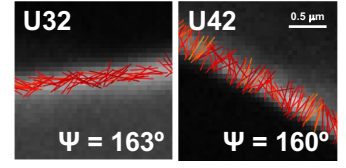
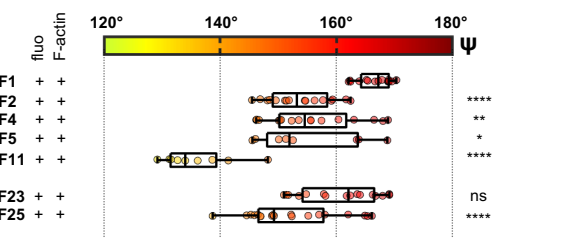
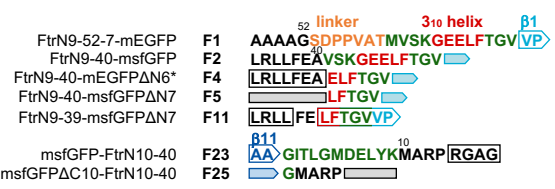
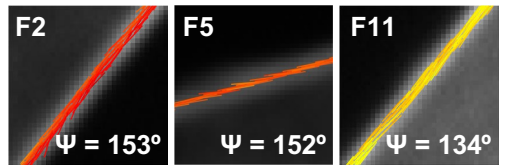
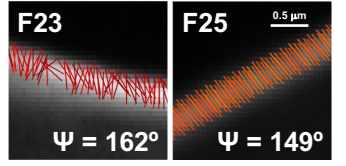
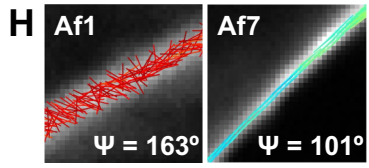
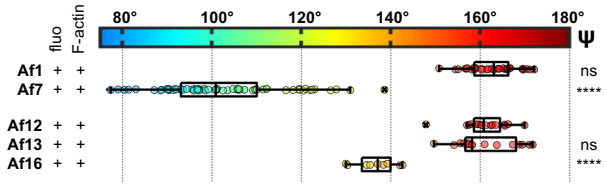
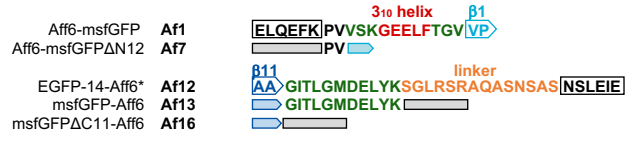
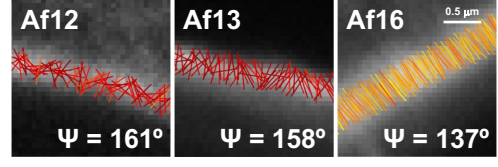
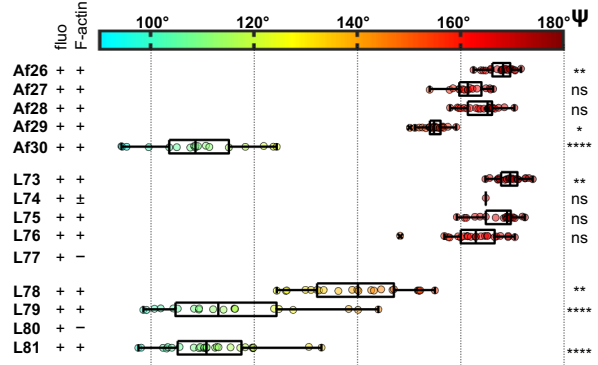
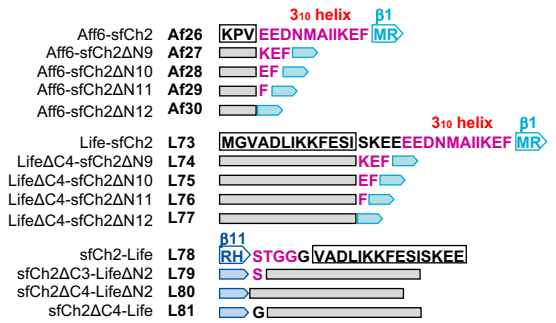
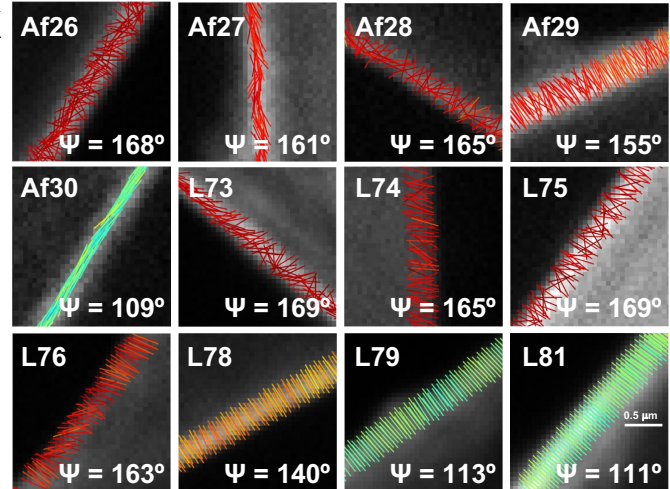


Fig2 Martins et al 2024

A**UtrophinCHD****B****C****D****F-tractin****E****F****G****Affimer6****I****J****Red fluorescent protein****K**

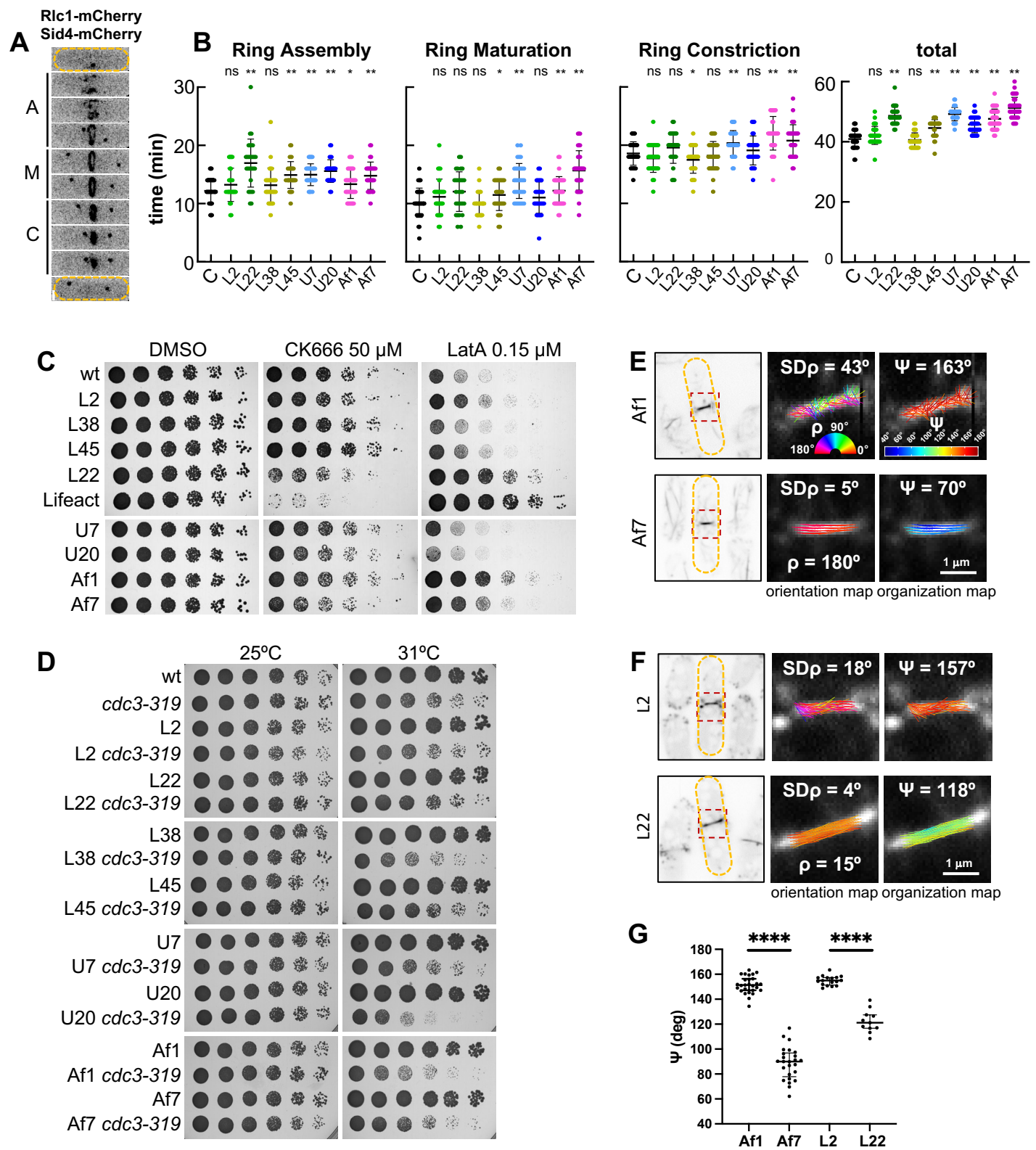


Fig5 Martins et al 2024

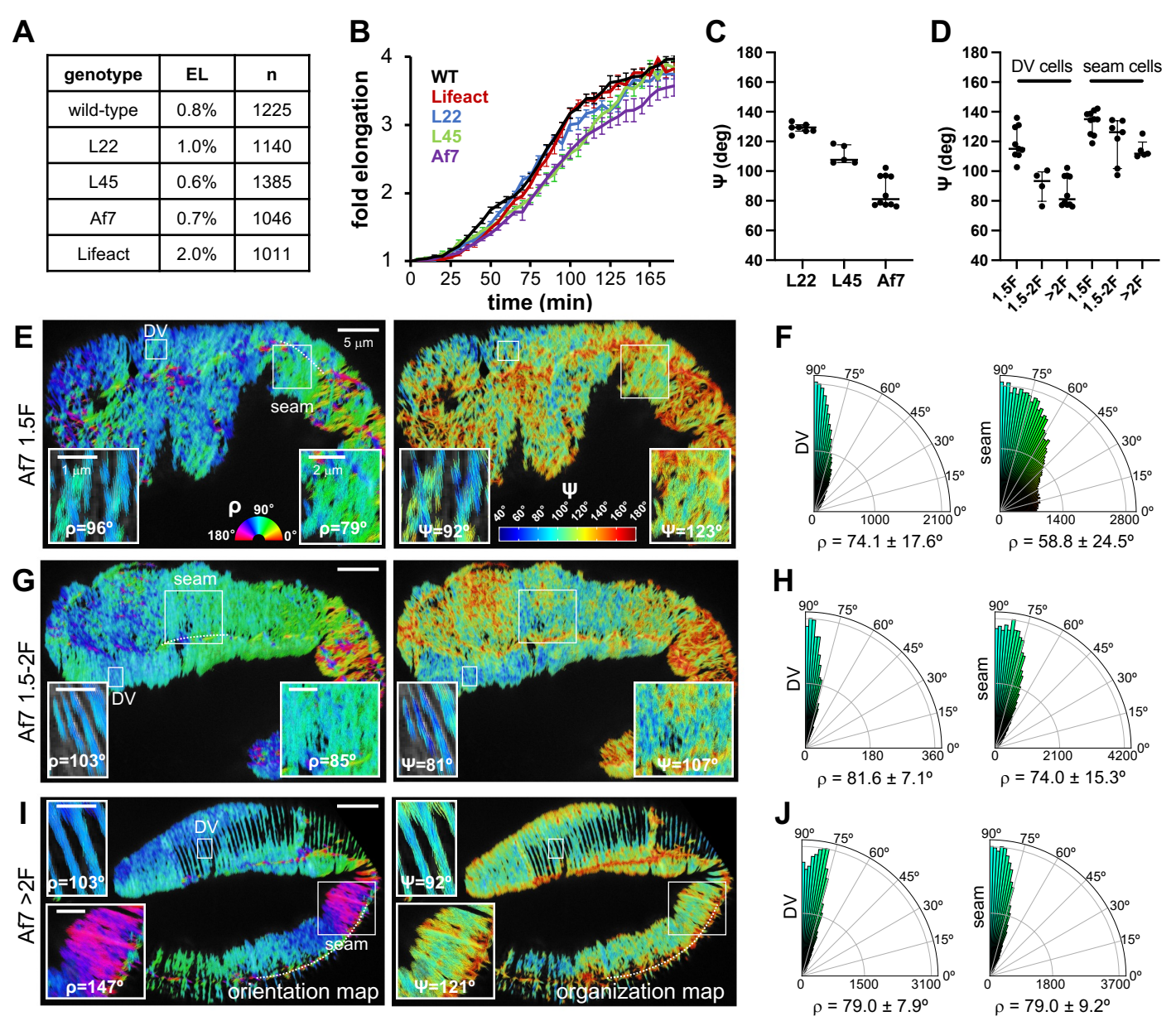


Fig6 Martins et al 2024

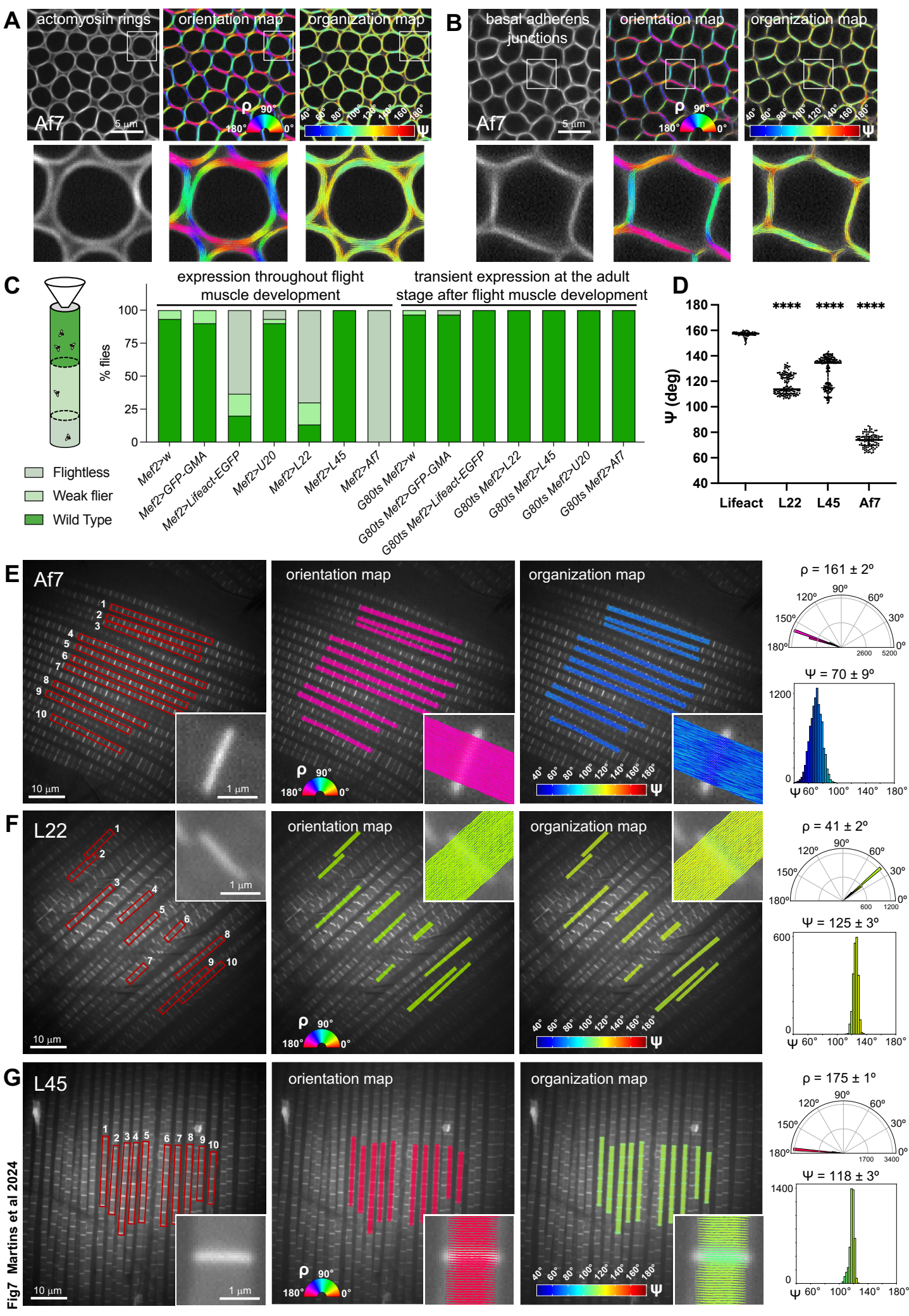


Figure legends

Figure 1. Measuring actin filament organization in cells with polarimetry

(A) Left, example of the polarization response of a sample at a given pixel of the image as obtained from a recorded polarimetry stack. The polarimetry stack is made of 18 polarized fluorescence images acquired using an incident linear polarization angle, α , varying from 0° to 170° with steps of 10° . Raw datapoints are shown as triangles and the theoretical fitting curve as a solid line. Right, schematic of a hypothetical organization of four fluorescently-labeled actin filaments in the confocal volume of the measured pixel, with the different orientations of the fluorophore dipoles shown by green double-headed arrows. The fluorophore dipoles are parallel to the actin filament axis in this example. The angle ρ corresponds to the mean orientation of all dipoles and thus the average orientation of actin filaments in the confocal volume. The ρ value is represented with a purple stick whose orientation and color depict the mean filament orientation in the pixel (see colorbar in (B)). The angle ψ corresponds to the angular aperture explored by all dipoles and is thus a readout of the average actin filament alignment in the confocal volume: the higher the filament alignment, the smaller the ψ angle.

(B) Representative examples of polarimetry measurements of actin filament organization in fixed U2OS cells labeled with AF488-phalloidin (top) or SiR-actin (bottom). The zoomed-out images on the left are summed intensity images of the respective polarimetry stacks. Insets on the right show zoom-ins of selected regions of interest (red outlined boxes) containing actin stress fibers (SFs) in different orientations, with the measured ρ and ψ angles per pixel. The angles ρ are represented as ρ stick maps ("orientation maps"), with a stick per pixel whose orientation and color depict the mean filament orientation in the pixel. The values of ρ , from 0° to 180° , are color-coded according to the colorbar. The angles ψ are represented as ψ stick maps ("organization maps"), with a stick per pixel whose orientation depicts the mean filament orientation (ρ) and whose color corresponds to the mean filament alignment (ψ) in the pixel. The values of ψ , from 40° to 180° , are color-coded according to the colorbar. Given that actin filaments are parallel to the long axis of SFs, the experimental measurements show that AF488 dipoles in the AF488-phalloidin conjugates are parallel to actin filaments (green double-headed arrows in the scheme on the far right), while SiR dipoles in the SiR-actin conjugates are oriented perpendicular to actin filaments (red double-headed arrows in the scheme on the far right).

(C) Box plots depicting the distribution of ψ angle measurements on SFs as shown in (B). The data points, color-coded according to the ψ colorbar, are plotted on top of the respective box plots. On each box, the central mark indicates the median, and the left and right edges of the box indicate the 25th and 75th percentiles, respectively. The whiskers extend to the most extreme data points not considered outliers, and the outliers are plotted individually using the 'x' symbol. The number of measurements in each box plot is $n = 258$ and 45 for AF488-phalloidin and SiR-actin, respectively. The respective median values are 126° and 133° .

(D) Schematics showing the dependence of measured ψ angles on the underlying actin filament organization, the mobility of the fluorophore and the tilt angle, ξ , of the fluorophore with respect to the axis of the actin filament. ψ is color-coded as in (B). The mean filament orientation, ρ , is the same in all cases. Flexible fluorophores will lead to very high ($>160^\circ$) ψ values and thus an overestimation of disorder even for highly aligned actin filaments (i). Constrained fluorophores allow us to detect changes in actin filament organization (ii and iii vs. iv).

(E) Representative ψ stick maps on SFs from measurements in live cells expressing widely used GFP fusions of actin-binding peptides or domains, or G-actin itself. The number shown in orange corresponds to the number of amino acid residues of the linker between the GFP and the actin-binding moiety. Mean ψ values are shown.

(F) Ribbon representation of the crystal structure of superfolder GFP (sfGFP) (PDB 2B3P). The N-terminal 3_{10} helix and beta-strands $\beta 1$ and $\beta 11$ are depicted in red, cyan and blue, respectively. Magenta arrowheads point to the beginning of $\beta 1$ and the end of $\beta 11$.

(G) Top, amino acid sequence of the N- and C-termini of monomeric EGFP (mEGFP) and monomeric sfGFP (msfGFP). The depicted secondary structure elements, color code and arrowheads are as in (F). Residue numbering is as shown. Bottom, screening of N- and C-terminal truncation mutants of mEGFP and msfGFP using fluorescence-activated cell sorting (FACS). Bars (mean + SD) depict the measured percentages of fluorescence-positive (FP+) cells for full-length (FL), N-terminally (ΔN) and C-terminally (ΔC) truncated proteins. The mean values are, from left to right: 100, 100, 74, 94, 53, 100, 42, 85, 4, 72, 9, 63, 0.4, 43, 0.1, 80, 65, 96, 72, 86, 69, 87, 0.2, and 80. Data are from three independent

experiments. Statistical significance was obtained using an unpaired t-test. The different constructs were compared to the respective FL; ns=not significant ($P>0.05$); * $P<0.05$, ** $P<0.01$, *** $P<0.001$, **** $P<0.0001$.

(H) Screening of the GFP constructs used in (G) with spinning disk fluorescence microscopy. Representative images of live cells expressing each construct are shown. For the sake of comparison, images are displayed with the same intensity range. In the case of weakly fluorescent cells, insets show contrast-enhanced images. No fluorescence was detectable for mEGFP Δ N12 Δ C11.

(I) Ribbon representation of the GFP dimerization interface from the crystal structure of GFP (PDB 1GFL). The hydrophobic residues A206 (V206 for sfGFP), L221 and F223 in the dimer interface are shown in brown. The respective monomerizing mutations used for impairing dimerization are shown.

(J-K) Designs used in this study to immobilize genetically-encoded fluorophore fusions to actin-binding domains (ABDs) (J) or G-actin itself (K). ABDs were fused to the N- or C-terminus of msfGFP (J, left) or placed in-between the N- and C-terminus of GFP using a circularly permuted GFP (cpGFP) (J, right). For G-actin terminal fusions, msfGFP or tetracysteine peptides were fused to the N-terminus of G-actin (K, left and right). For G-actin intramolecular fusions, msfGFP, the β 11 strand alone, or tetracysteine peptides were placed intramolecularly within the G-actin structure (K, left, middle and right).

Figure 2. Engineering of Lifeact-based actin filament organization reporters for live-cell polarimetry

(A) List of Lifeact ("Life" for short)-GFP fusions tested for their usability in live polarimetry measurements in U2OS cells expressing each fusion. All constructs were expressed with a CMV_{trunc} promoter except the ones with an asterisk (*) which used a CMV promoter. The left column lists the tested fusions as follows: a short name for each fusion (e.g., Life-msfGFP Δ N6) followed by its designated number ("L5" in this case) and its primary sequence. Secondary structure elements of GFP are color-coded as in Fig.1F. To facilitate the tracking of modifications, only the region of the primary sequence that is modified is shown. Sequences that stay unchanged from one construct to the next one are shown with an outlined box for the first one (e.g. L1) and then represented as gray-filled boxes in subsequent constructs (in this case, L2-L12). Additional columns report whether the construct is fluorescent (column "fluo") and if it binds actin SFs (column "F-actin"). Constructs were classified as fluorescent (+), very weakly fluorescent (\pm), or nonfluorescent (-), and as binding to F-actin (+), very weakly binding to F-actin (\pm), or not binding to F-actin (-). For very weakly fluorescent or nonfluorescent constructs, F-actin binding was not determined (nd). Box plots on the far right depict the distribution of ψ angle measurements on SFs for the respective constructs. Box plots are depicted as in Fig.1C. Polarimetry measurements were not performed for constructs that were weakly fluorescent or weak F-actin binders and thus not usable for routine polarimetry. The number of measurements (see methods for details), from top to bottom, are n= 30, 40, 25, 25, 26, 21, 18, 22, 21, 15, 17, 15, 21, 22, 11, 19, 24, 23, 29, 11, 10, 20, 9, 17, 20, 10, 33, 15, 23, 20, 21, 26, 11, 18, 16, 21, 16, 8, 16, 3, 22, 7. The respective median ψ values are 162, 161, 160, 155, 152, 143, 151, 148, 141, 144, 137, 138, 163, 155, 161, 153, 132, 133, 130, 136, 147, 138, 138, 149, 147, 167, 160, 160, 154, 162, 142, 134, 142, 160, 163, 165, 141, 145, 155, 159, 158, 160°. Statistical significance (right-most column) was obtained using a non-parametric Kruskal-Wallis test followed by a Dunn's multiple comparisons test. The different constructs were compared to L1; ns=not significant ($P>0.05$); * $P<0.05$, ** $P<0.01$, *** $P<0.001$, **** $P<0.0001$.

(B-C) Representative ψ stick maps on SFs from measurements in live cells expressing the shown C-terminal (B) and N-terminal (C) GFP fusions, with mean ψ values indicated. The selected images correspond to median ψ values of the respective distributions. See also Figure S1.

Figure 3. Engineering of Utrophin, F-tractin, Affimer6- and red fluorescent protein-based actin filament organization reporters for live-cell polarimetry

(A) List of selected Utrophin calponin homology domain ("Utr" for short)-GFP fusions tested for their usability in live polarimetry measurements in U2OS cells expressing each fusion. The full screen is shown in Figure S2A. Fusion illustration and classification and box plots are as detailed in Figure 2A. Statistical significance (right-most column) was obtained using a non-parametric Kruskal-Wallis test followed by a Dunn's multiple comparisons test. The different constructs were compared to U1; ns=not significant ($P>0.05$); *** $P<0.001$, **** $P<0.0001$. The number of measurements and the respective median ψ values for each fusion are mentioned in Figure S2A.

(B-C) Representative ψ stick maps on SFs from measurements in live cells expressing the shown N-terminal (B) and C-terminal (C) GFP fusions, with mean ψ values indicated. The selected images correspond to median ψ values of the respective distributions. See also Figure S2.

(D) List of selected F-tractin ("Ftr" for short)-GFP fusions tested for their usability in live polarimetry measurements in U2OS cells expressing each fusion. The full screen is shown in Figure S3C. Fusion illustration and classification and box plots are as detailed in Figure 2A. Statistical significance (right-most column) was obtained using a non-parametric Kruskal-Wallis test followed by a Dunn's multiple comparisons test. The different constructs were compared to F1; ns=not significant ($P>0.05$); * $P<0.05$, ** $P<0.01$, **** $P<0.0001$. The number of measurements and the respective median ψ values for each fusion are mentioned in Figure S3C.

(E-F) Representative ψ stick maps on SFs from measurements in live cells expressing the shown C-terminal (E) and N-terminal (F) GFP fusions, with mean ψ values indicated. The selected images correspond to median ψ values of the respective distributions. See also Figure S3.

(G) List of selected Affimer6 ("Aff6" for short)-GFP fusions tested for their usability in live polarimetry measurements in U2OS cells expressing each fusion. The full screen is shown in Figure S3F. Fusion illustration and classification and box plots are as detailed in Figure 2A. Statistical significance (right-most column) was obtained using a non-parametric Kruskal-Wallis test followed by a Dunn's multiple comparisons test. The different constructs were compared to Af12; ns=not significant ($P>0.05$); **** $P<0.0001$. The number of measurements and the respective median ψ values for each fusion are mentioned in Figure S3F.

(H-I) Representative ψ stick maps on SFs from measurements in live cells expressing the shown C-terminal (H) and N-terminal (I) GFP fusions, with mean ψ values indicated. The selected images correspond to median ψ values of the respective distributions. See also Figure S3.

(J) List of Affimer6- and Lifeact-based sfCherry2 ("sfCh2" for short) fusions tested for their usability in live polarimetry measurements in U2OS cells expressing each fusion. sfCherry2 fusions were either C-terminal (Af26- Af30, L73-L77), or N-terminal (L78-L81). Fusion illustration and classification and box plots are as detailed in Figure 2A. The number of measurements (see methods for details), from top to bottom, are $n=23, 16, 23, 25, 18, 23, 1, 22, 22, 22, 20, 25$. The respective median ψ values are 168, 161, 165, 155, 109, 170, 165, 169, 163, 140, 113, 111°. Statistical significance (right-most column) was obtained using a non-parametric Kruskal-Wallis test followed by a Dunn's multiple comparisons test. The different Affimer6 constructs were compared to Af12; the different Lifeact constructs were compared to L1; ns=not significant ($P>0.05$); * $P<0.05$, ** $P<0.01$, **** $P<0.0001$.

(K) Representative ψ stick maps on SFs from measurements in live cells expressing the shown Affimer6-based (Af) and Lifeact-based (L) sfCherry2 fusions, with mean ψ values indicated. The selected images correspond to median ψ values of the respective distributions.

Figure 4. Engineering of G-actin-based actin filament organization reporters for live-cell polarimetry

(A) List of human β -actin ("act" or "actin" for short) fusions tested for their usability in live polarimetry measurements in U2OS cells expressing each fusion. The fluorophores used were GFP, the β 11 strand alone ("GFP11"), or tetracysteine peptides ("cys6" or "cys12") as shown in Fig.1K. For G-actin terminal fusions, GFP or tetracysteine peptides were fused to the N-terminus of G-actin (A1-A6). For G-actin intramolecular fusions, msfGFP (A7-A23), the β 11 strand alone (A24-A37), or tetracysteine peptides (A38-A47) were placed intramolecularly within the G-actin structure (see (B)). Fusion illustration and classification and box plots are as detailed in Figure 2A. Fusions A6, A40 and A41 localized both to SFs and to nuclear F-actin, and box plots include measurements from both F-actin pools. Measurements for fusions A42 and A47 are from nuclear F-actin. The number of measurements (see methods for details), from top to bottom, are $n=23, 24, 26, 15, 18, 6, 12, 17, 17, 19, 18, 18, 26, 26, 17, 1, 1$. The respective median ψ values are 161, 160, 158, 146, 148, 168, 166, 157, 163, 162, 150, 148, 158, 162, 164, 167, 165°. Statistical significance (right-most column) was obtained using a non-parametric Kruskal-Wallis test followed by a Dunn's multiple comparisons test. The different constructs were compared to A1; ns=not significant ($P>0.05$); *** $P<0.001$, **** $P<0.0001$.

(B-C) Ribbon representation of F-actin with three consecutive G-actin monomers colored in green, magenta and blue (PDB 5JLF) (B, left). Helix h7, used as an insertion site in intramolecular fusions, is shown in red. A close-up view of h7 (dashed box) shows residues in the loops (in cyan) flanking the helix, with arrowheads pointing to the insertion sites used in intramolecular fusions (B, right). (C)

WebLogo3 representation of the conservation of residues in h7 and the flanking residues. Forty-five actin sequences were used for this representation, including organisms as diverse as *Drosophila*, fungi, Dictyostelium, Arabidopsis, and sea animals. Negatively- and positively-charged residues are shown in red and blue, respectively.

(D-E) Representative ψ stick maps on SFs from measurements in live cells expressing the shown N-terminal (D) and intramolecular (E) GFP fusions, with mean ψ values indicated. The selected images correspond to median ψ values of the respective distributions. See also Figure S4.

Figure 5. Polarimetry measurements of actin filament organization in live dividing fission yeast expressing selected reporters

(A) Time-lapse maximum intensity projection images of a fission yeast cell (orange dash outline) expressing an acto-myosin ring marker (Rlc1-mCherry) and a spindle pole body marker (Sid4-mCherry) to monitor major cytokinetic events. The time interval between frames corresponds to 6 minutes. "A" represents the cytokinetic ring assembly stage, "M", the cytokinetic ring maturation stage and "C", the cytokinetic ring constriction stage. Scale bar, 2 μ m.

(B) Quantification of the time taken for ring assembly completion, ring maturation, ring constriction, and the total time for cytokinesis completion in fission yeast strains expressing each actin reporter and the cytokinetic markers. As a control ("C"), a strain expressing only the cytokinetic markers was used. Scatter plots show means \pm SD. The number of cells for each strain is, from left to right: 41, 31, 29, 31, 31, 33, 29, 36, 33. The mean measured times for each strain are, from left to right: 12, 13, 17, 13, 15, 15, 16, 13, 15 min for ring assembly; 10, 11, 12, 10, 11, 14, 11, 12, 16 min for ring maturation; 19, 18, 20, 17, 18, 20, 19, 22, 21 min for ring constriction; and 41, 42, 49, 41, 45, 49, 46, 48, 51 min for total cytokinesis. A t-test was applied to evaluate statistical differences between each strain and the control; ns=not significant, $P > 0.05$; * $0.05 > P > 0.03$; ** $P < 0.03$.

(C) Serial dilution assay showing the sensitivity of the fission yeast strains expressing the corresponding actin reporter to the Arp2/3 complex inhibitor CK666, the G-actin sequestering drug latrunculin A (LatA), and DMSO (vehicle control). As controls, a previously published strain expressing Lifeact under the control of the actin promoter ('Lifeact') (Huang et al., 2012) and a wild-type strain ('wt') were included in the assay.

(D) Serial dilution assay showing the genetic interaction between the profilin mutant *cdc3-319* and the expression of the different actin reporters.

(E-G) Polarimetry measurements of actin filament organization in the cytokinetic ring of living dividing fission yeast cells expressing Affimer6-based (E) and Lifeact-based (F) reporters. Representative measurements are shown for fusions with unconstrained GFPs (Af1, L2) and constrained GFPs (Af7, L22). Left panels in (E), (F) show inverted grayscale summed intensity images of polarimetry stacks for the respective dividing yeast cells (orange dash outlines). ρ and ψ stick maps of actin organization in the cytokinetic ring (red dash box in left panels) are shown in the middle and right panels, respectively. The standard deviation of ρ values (SD ρ), mean ρ and ψ values are shown for each map. Scatter plots in (G) show the quantification of ψ angle distributions for each reporter. Scatter plots show medians with interquartile range. The number of cells for each strain is, from left to right: 26, 20, 17, 9. The respective median ψ values are 151, 90, 155, 121°. Statistical significance was obtained using a non-parametric Mann-Whitney test; **** $P < 0.0001$. See also Figure S5.

Figure 6. Polarimetry measurements of actin filament organization in live elongating *C. elegans* embryos expressing selected reporters

(A) Viability of *C. elegans* strains expressing different reporters assessed by the number of unhatched embryos 12-16 h after egg-laying. EL, embryonic lethality. n=number of scored embryos per genotype. See methods for details of the genotypes.

(B) Embryonic growth curves, showing fold-change of embryonic length until hatching based on differential interference contrast (DIC) filming of the indicated *C. elegans* strains. Curves show means \pm SEM. n=10 embryos were measured for each genotype. See also Figure S6.

(C) Polarimetry measurements of actin filament organization in the circumferential bundles of dorsal and ventral epidermal cells (DV cells) in >2-fold stage embryos expressing the indicated reporters. Scatter plots show the quantification of ψ angle distributions for each reporter. Scatter plots show medians with interquartile range. The number of embryos for each strain is, from left to right: 7, 5, 8. The respective median ψ values are 130, 108, 81°.

(D-J) Polarimetry measurements of actin filament reorganization in the epidermis during embryonic elongation. (D) Scatter plots show the quantification of ψ angle distributions in DV cells and in seam cells in 1.5-fold, 1.5-2-fold and >2-fold stage embryos expressing Af7 as shown in (E), (G), (I). Scatter plots show medians with interquartile range. The number of embryos for each stage is, from left to right: 9, 4, 8, 9, 7, 4. The respective median ψ values are 115, 93, 81, 135, 126, 112°. (E), (G), (I) Representative ρ (left) and ψ (right) stick maps in DV and seam cells in 1.5-fold (E), 1.5-2-fold (G) and >2-fold (I) stage embryos expressing Af7. Insets show zoom-ins of selected ROIs (white outlined boxes) in the respective cell types. Mean ρ and ψ values are shown for each ROI. For all panels, anterior is to the left and dorsal is up. (F), (H), (J) Polar histograms of ρ value distributions in DV and seam cells in 1.5-fold (F), 1.5-2-fold (H) and >2-fold (J) stage embryos expressing Af7. ρ values are represented with respect to the DV/seam boundary (dotted line in (E)): considering that Af7 dipoles are parallel to actin filaments, the more perpendicular mean actin filament orientations are to the boundary, the closer the angle values are to 90° and the narrower the respective distributions. Means \pm SD are shown. The number of embryos for each stage and type of cells is as in (D). See also Figure S6.

Figure 7. Polarimetry measurements of actin filament organization in live cellularizing *Drosophila* embryos and live flight muscle expressing selected reporters

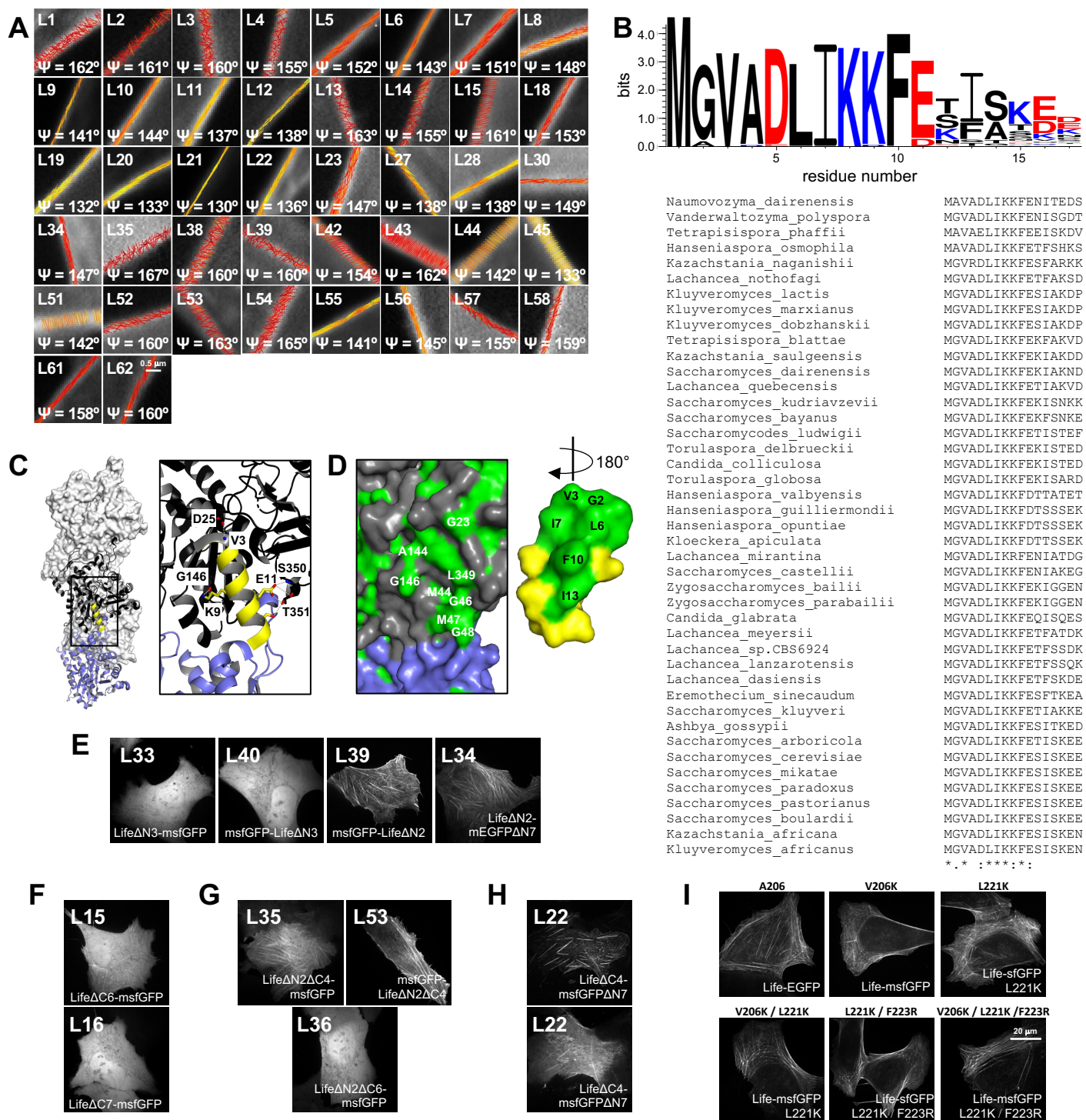
(A-B) Polarimetry measurements of actin filament organization in cellularizing *Drosophila* embryos expressing Af7, in the actomyosin rings associated with the invaginating membrane front (A) and at the basal adherens junctions right apicolaterally to the former (B). The left images are summed intensity images of the respective polarimetry stacks. The middle and right images show the measured ρ and ψ angles per pixel, respectively. Insets show zoom-ins of selected ROIs (white outlined boxes)

(C) Flight tests were performed to compare the flight ability of strains expressing different actin-binding reporters (see methods for the assay and for details of the genotypes). The left scheme depicts the flight test assay: depending on their flight ability, flies were scored as "wild-type", "weak flier" or "flightless". The bar graph on the right quantifies the respective percentages for each strain. Reporters were expressed under the control of a muscle-specific driver, Mef2-GAL4, either throughout muscle development (*Mef2>*), or transiently after muscle development (*G80ts Mef2>*). Thirty flies were scored in total for each strain in three independent experiments. The mean percentages of "wild-type", "weak flier" or "flightless" flies are respectively, from left to right: 93,7,0; 90,10,0; 20,17,63; 90,3,7; 13,17,70; 100,0,0; 0,0,100; 97,3,0; 97,0,3; 100,0,0; 100,0,0; 100,0,0; 100,0,0; 100,0,0.

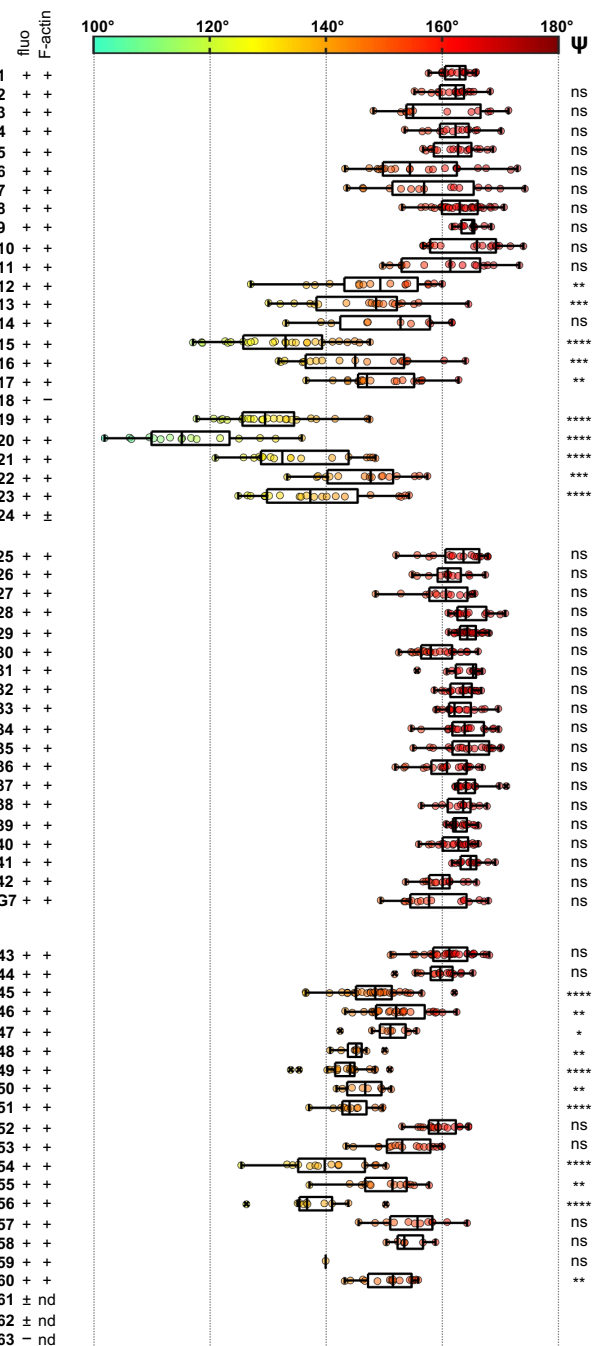
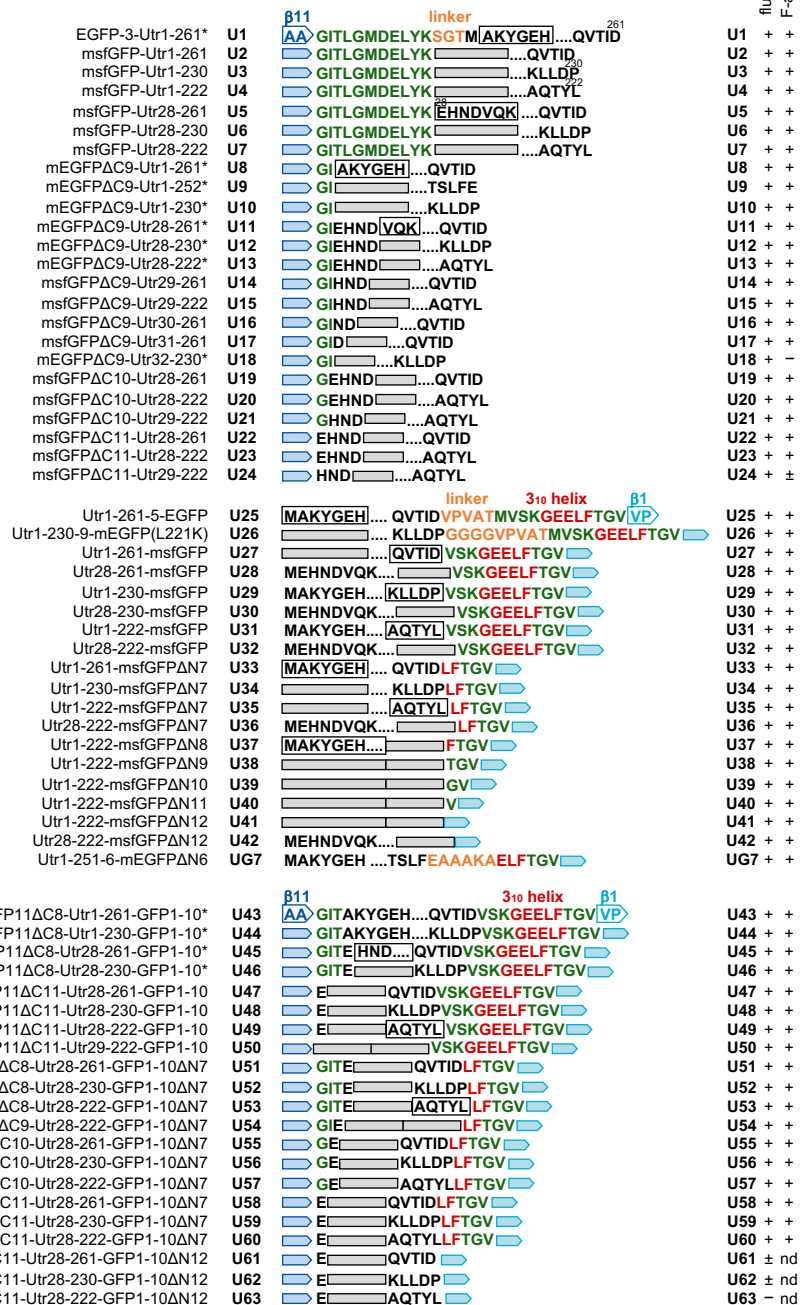
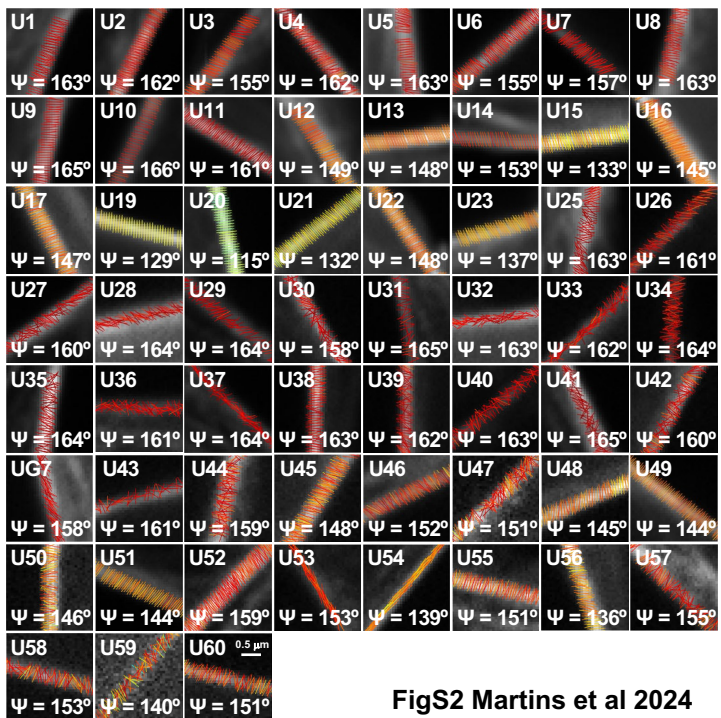
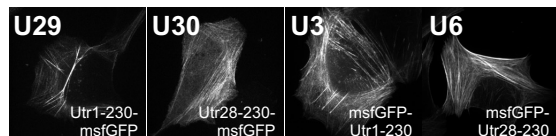
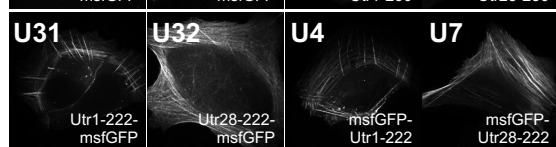
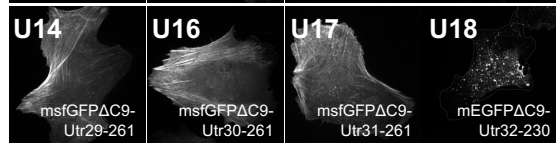
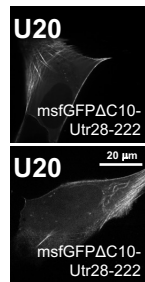
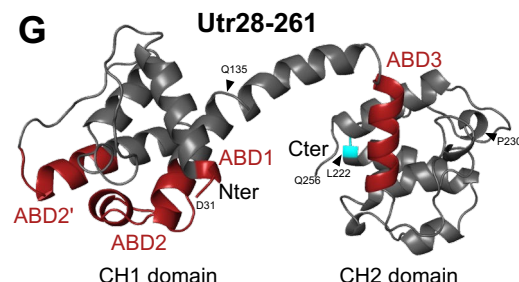
(D-G) Polarimetry measurements of actin filament organization in live flight muscle expressing the indicated reporters. All reporters were expressed throughout flight muscle development except Af7 that was expressed transiently at the adult stage after flight muscle development. Scatter plots in (D) show the quantification of ψ angle distributions for each reporter measured as shown in (E)-(G). Scatter plots show medians with interquartile range. One datapoint represents one myofibril (see methods for details). The number of myofibrils for each strain is, from left to right: 70, 140, 190, 100. The respective median ψ values are 157, 114, 134, 74°. Statistical significance was obtained using a non-parametric Mann-Whitney test. The different constructs were compared to Lifeact; **** P<0.0001. (E)-(G) Left panels are summed intensity images of the respective polarimetry stacks. Middle and right panels are ρ and ψ stick maps in the flight muscle of the shown hemithorax, respectively. Ten myofibrils (red outlined boxes) were quantified in each field of view. Insets show zoom-ins of a selected sarcomere. The rightmost panels for each strain show examples of polar histograms of ρ value distributions and histograms of ψ value distributions for a single myofibril. Means \pm SD are shown. See also Figure S7.

References

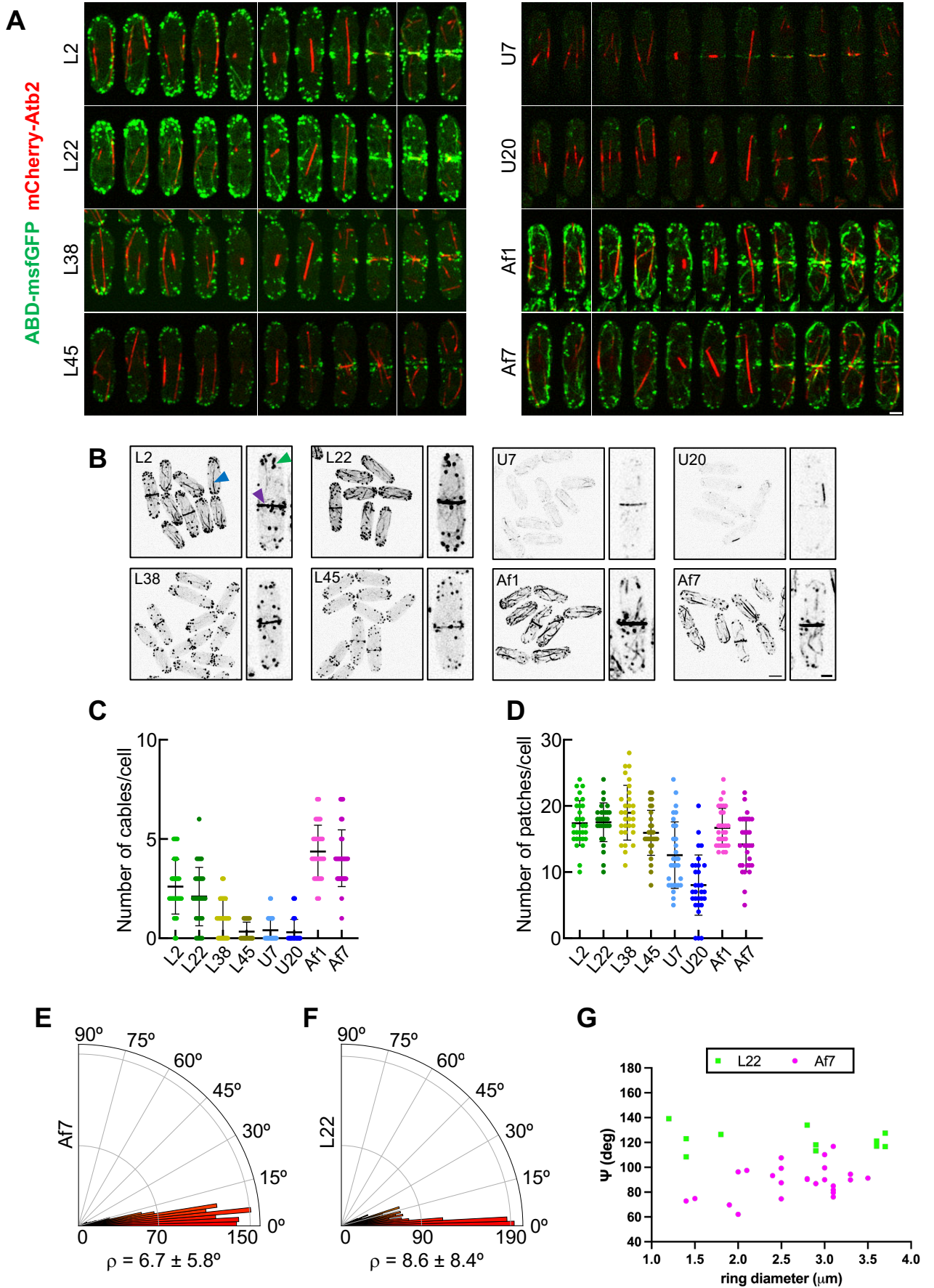
Huang, J.Q., Huang, Y.Y., Yu, H.C., Subramanian, D., Padmanabhan, A., Thadani, R., Tao, Y.Q., Tang, X., Wedlich-Soldner, R., and Balasubramanian, M.K. (2012). Nonmedially assembled F-actin cables incorporate into the actomyosin ring in fission yeast. *Journal of Cell Biology* 199, 831-847.



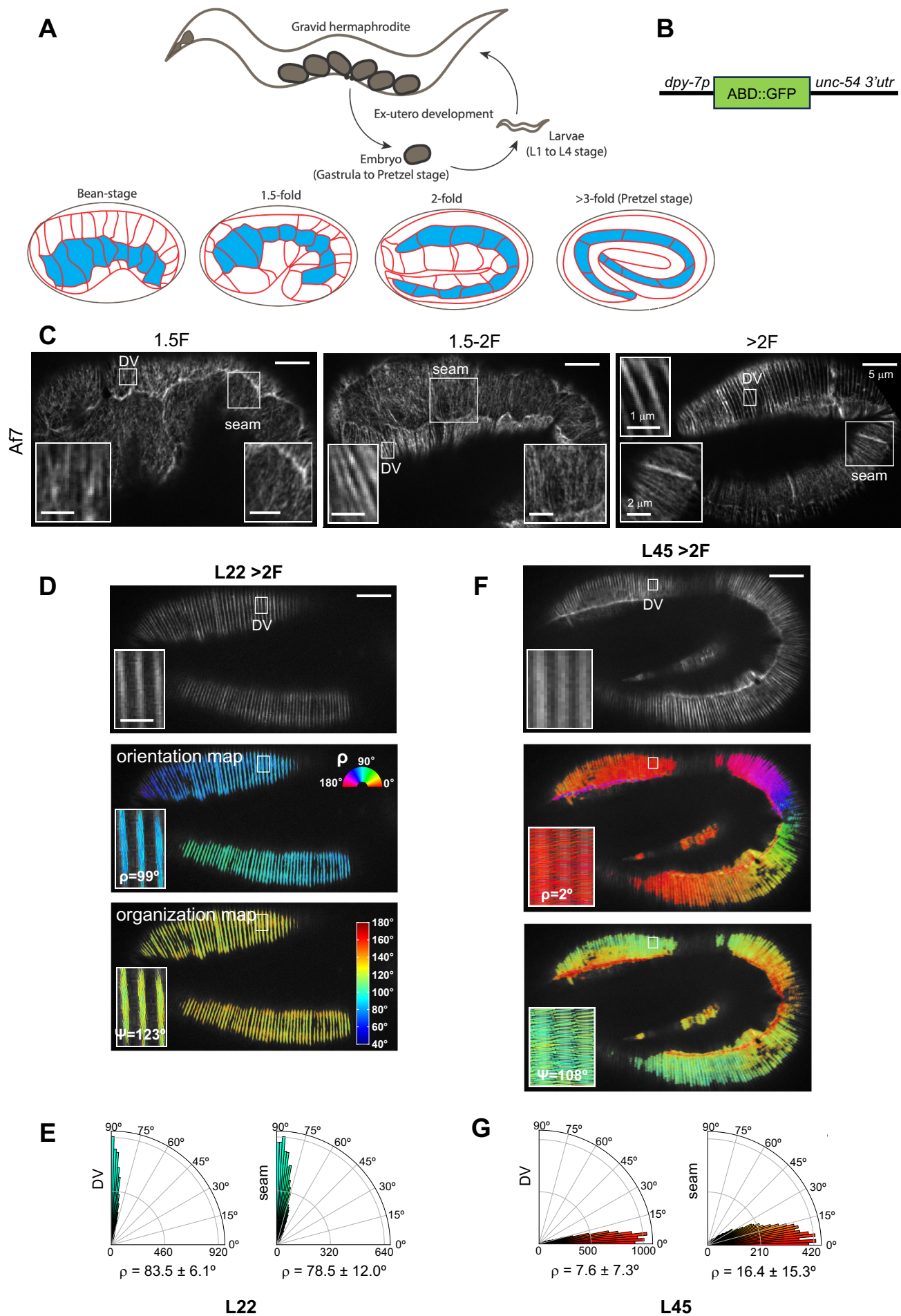
FigS1 Martins et al 2024

A**B****C****D****E****F****G**

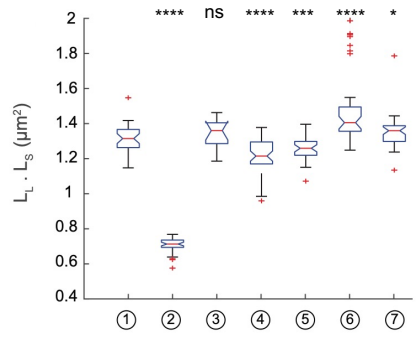
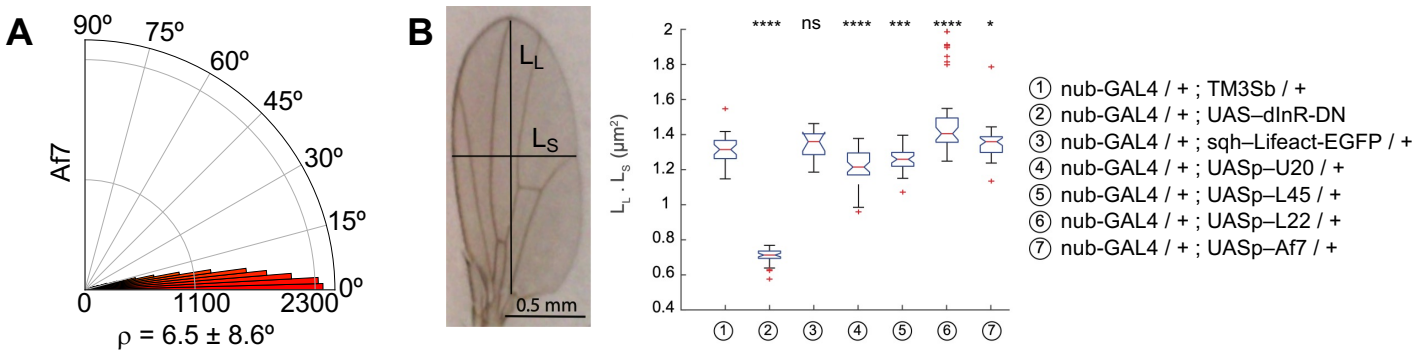
FigS2 Martins et al 2024



FigS5 Martins et al 2024



FigS6 Martins et al 2024



FigS7 Martins et al 2024

Supplemental Figure legends

Figure S1. Engineering of Lifeact-based actin filament organization reporters for live-cell polarimetry, Related to Figure 2.

(A) Representative ψ stick maps on SFs from measurements in live cells expressing the indicated fusions, with mean ψ values indicated. The selected images correspond to median ψ values of the respective distributions.

(B) Top, WebLogo3 representation of the conservation of residues in the Lifeact sequence. Negatively- and positively-charged residues are shown in red and blue, respectively. Bottom, the Lifeact sequences from 43 different budding yeast strains used for the WebLogo representation are shown. The consensus symbols are from the ClustalO multiple sequence alignment: *, fully conserved residue; :, conservation between residues with strongly similar physicochemical properties; ., conservation between residues with weakly similar physicochemical properties.

(C-D) 3D structure of the Lifeact-F-actin complex (Belyy et al., 2020; Kumari et al., 2020). (C) Surface representation (light grey) of three G-actin monomers within an actin filament (PDB 7AD9). Two neighboring actin subunits (n, n+2), colored in black and blue, are shown in ribbon representation, and Lifeact is shown in yellow. A close-up view (black outlined box on the left) illustrates polar interactions at the actin-Lifeact interface, with key residues and their side chains depicted in stick representation. (D) Surface representation of the actin-Lifeact interface shown in the close-up view of (C), highlighting hydrophobic residues in green. Lifeact is rotated by 180° to visualize the hydrophobic residues facing the actin monomer.

(E-G) Representative images of U2OS cells expressing the indicated reporters for assessing the contribution of specific Lifeact residues to actin binding. The localization of the reporters (diffuse cytosolic vs binding to SFs) shows that V3 is essential (E), that the six C-terminal residues are not essential (F), and that G2 is not essential but its absence can compromise actin binding when combined with other truncations (G).

(H) Lifeact-based reporters localize both to SFs and to mitochondria: two different z-planes in the same cell show L22 on SFs (top plane) and mitochondria (bottom plane).

(I) Fluorescence images of U2OS cells expressing Lifeact fusions to EGFP or to sfGFP bearing one, two or three monomerizing mutations. Lifeact localizes to arc nodes in all cases.

Figure S2. Engineering of Utrophin-based actin filament organization reporters for live-cell polarimetry, Related to Figure 3.

(A) List of Utrophin calponin homology domain ("Utr" for short)-GFP fusions tested for their usability in live polarimetry measurements in U2OS cells expressing each fusion. Fusion illustration and classification and box plots are as detailed in Figure 2A. The number of measurements (see methods for details), from top to bottom, are n= 18, 19, 13, 14, 17, 21, 15, 30, 11, 17, 16, 16, 20, 11, 26, 19, 18, 24, 16, 18, 16, 20, 17, 13, 14, 14, 25, 23, 13, 18, 16, 18, 19, 21, 15, 13, 17, 19, 14, 15, 16. 31, 17, 31, 27, 9, 8, 19, 8, 12, 17, 17, 14, 14, 10, 12, 6, 1, 15. The respective median ψ values are 163, 162, 155, 162, 163, 154, 157, 163, 165, 166, 161, 149, 149, 153, 133, 145, 147, 129, 115, 132, 148, 137, 163, 161, 160, 164, 164, 158, 165, 163, 162, 164, 164, 161, 164, 163, 162, 163, 165, 160, 158, 161, 159, 148, 152, 151, 145, 144, 146, 144, 159, 153, 139, 151, 136, 155, 153, 140, 151°. Statistical significance (right-most column) was obtained using a non-parametric Kruskal-Wallis test followed by a Dunn's multiple comparisons test. The different constructs were compared to U1; ns=not significant (P>0.05); * P<0.05, ** P<0.01, *** P<0.001, **** P<0.0001.

(B) Representative ψ stick maps on SFs from measurements in live cells expressing the indicated fusions, with mean ψ values indicated. The selected images correspond to median ψ values of the respective distributions.

(C-E) Representative images of U2OS cells expressing the indicated reporters for assessing the contribution of specific Utrophin residues to actin binding. The localization of these reporters to SFs shows that removing the 27 N-terminal residues of Utrophin or/and shortening its C-terminus to Utr222 or Utr230 do not compromise actin binding (C,D). Proximity of C-terminally truncated GFP to Utr29-32 (E) can impair actin binding (U18).

(F) Utrophin-based reporters localize both to SFs and to mitochondria: two different z-planes in the same cell show U20 on SFs (top plane) and mitochondria (bottom plane).

(G) Ribbon representation of Utrophin structure showing the two calponin-homology (CH) domains and identified actin-binding sites (ABD) in red (PDB 1QAG) (Keep et al., 1999; Kumari et al., 2020). Arrowheads point to specific residues. L222 and P230 relate to Utr222 and Utr230 fusions, respectively. Q135 points to the end of the CH1 domain, which is sufficient for actin binding (Kumari et al., 2020).

Figure S3. Engineering of F-tractin- and Affimer6-based actin filament organization reporters for live-cell polarimetry, Related to Figure 3.

(A-B) WebLogo3 representation illustrating the conservation of residues in the F-tractinN9-52 sequence (A). Sequences from 65 mammals were used for this representation. Negatively- and positively-charged residues are shown in red and blue, respectively. AlphaFold helix prediction for residues 30-52 is shown in (B), with A40 shown in cyan. A40 relates to F-tractinN9-40 fusions.

(C) List of F-tractin ("Ftr" for short)-GFP fusions tested for their usability in live polarimetry measurements in U2OS cells expressing each fusion. Fusion illustration and classification and box plots are as detailed in Figure 2A. The number of measurements (see methods for details), from top to bottom, are n= 15, 16, 16, 16, 8, 9, 11, 14, 16, 19, 19, 12, 19, 14, 18, 18, 16, 14, 19, 17, 19, 23, 18, 11, 19. The respective median ψ values are 167, 153, 164, 154, 152, 134, 137, 165, 162, 163, 156, 152, 159, 158, 159, 163, 162, 159, 149, 156, 152, 159, 160, 164, 163°. Statistical significance (right-most column) was obtained using a non-parametric Kruskal-Wallis test followed by a Dunn's multiple comparisons test. The different constructs were compared to F1; ns=not significant ($P>0.05$); * $P<0.05$, ** $P<0.01$, *** $P<0.001$, **** $P<0.0001$.

(D) Representative ψ stick maps on SFs from measurements in live cells expressing the indicated F-tractin fusions, with mean ψ values indicated. The selected images correspond to median ψ values of the respective distributions.

(E) Representative images of U2OS cells expressing the indicated reporters for assessing the contribution of specific F-tractin residues to actin binding. The localization of the reporters to SFs (diffuse cytosolic vs binding to SFs) shows that residues 37-40 are critical for actin binding. Removing the 14 N-terminal residues does not compromise actin binding (F22). F-tractin-based reporters localize both to SFs and to mitochondria (rightmost panels): two different z-planes in the same cell (F22) show F22 on SFs (top plane) and mitochondria (bottom plane).

(F) List of Affimer6 ("Aff6" for short)-GFP fusions tested for their usability in live polarimetry measurements in U2OS cells expressing each fusion. Fusion illustration and classification and box plots are as detailed in Figure 2A. The number of measurements (see methods for details), from top to bottom, are n= 33, 19, 17, 14, 21, 17, 66, 17, 11, 7, 8, 16, 16, 19, 25, 9, 28, 30, 14, 11, 16. The respective median ψ values are 163, 149, 157, 160, 152, 155, 101, 157, 158, 155, 164, 161, 158, 145, 149, 137, 133, 146, 145, 160, 144°. Statistical significance (right-most column) was obtained using a non-parametric Kruskal-Wallis test followed by a Dunn's multiple comparisons test. The different constructs were compared to Af12; ns=not significant ($P>0.05$); ** $P<0.01$, *** $P<0.001$, **** $P<0.0001$.

(G) Representative ψ stick maps on SFs from measurements in live cells expressing the indicated Affimer6 fusions, with mean ψ values indicated. The selected images correspond to median ψ values of the respective distributions.

(H) Affimer6-based reporters localize both to SFs (Af7, left cell) and to mitochondria (Af7, right cell and Af15).

(I) Ribbon representation of the Affimer structure showing the two actin-binding sites (ABD) in red (PDB 4N6T) (Lopata et al., 2018; Tiede et al., 2014).

Figure S4. Engineering of G-actin- and red fluorescent protein-based actin filament organization reporters for live-cell polarimetry, Related to Figures 3 and 4.

(A) Top, amino acid sequence of the N- and C-termini of monomeric Apple (mApple) and superfolder Cherry2 (sfCherry2). The depicted secondary structure elements of mApple and sfCherry2 and color code are as in Fig.1F. Residue numbering is as shown. Bottom, screening of N- and C-terminal truncation mutants of mApple and sfCherry2 using FACS. Bars (mean + SD) depict the measured percentages of fluorescence-positive (FP+) cells for full-length (FL), N-terminally (Δ N) and C-terminally (Δ C) truncated proteins. The mean values are, from left to right: 100, 100, 57, 99, 79, 89, 60, 99, 54, 113, 40, 95, 83, 102, 9, 117, 0.03, 101, 0.06, 80, 118, 66, 115, 62, 110, 88, 107, 104, 88. Data are from three independent experiments. Statistical significance was obtained using an unpaired t-test. The

different constructs were compared to the respective FL; ns=not significant ($P>0.05$); * $P<0.05$, ** $P<0.01$, *** $P<0.001$, **** $P<0.0001$.

(B) Screening of the same constructs used in (A) with spinning disk fluorescence microscopy. Representative images of live cells expressing each construct are shown. For the sake of comparison, images are displayed with the same intensity range. For weakly fluorescent cells, insets show contrast-enhanced images. No fluorescence was detectable for mApple Δ N15 and mApple Δ N16.

(C-M) Functional characterization of intramolecular GFP (iGFP) fusions showing their usability for labeling specific G-actin isoforms. (C) Quantification of mitotic cells from an asynchronous population of HeLa FRT iGFP-beta-actin expressing cells treated as indicated. $N = 3$ for all conditions; $n = 543$ for 'Control siRNA'; $n = 715$ for 'Beta Actin siRNA - dox'; $n = 321$ for 'Beta Actin siRNA + dox'. ** $p = 0.0052$ by a parametric student's t-test. (D) Quantification of mitotic cells from an asynchronous population of HeLa FRT iGFP-gamma-actin expressing cells treated as indicated. $N = 4$ for all conditions; $n = 439$ for 'Control siRNA'; $n = 451$ for 'Gamma Actin siRNA - dox'; $n = 418$ for 'Gamma Actin siRNA + dox'. * $p = 0.0475$; ** $p = 0.0282$ by a parametric student's t-test. (E) Classification of mitotic cells described in (C) as either prophasic or metaphasic. A total of 22 metaphase cells were scored for 'Control siRNA'; 11 metaphase cells for 'Beta siRNA -dox'; 17 metaphase cells for 'Beta siRNA +dox'. ** $p = 0.0069$; * $p = 0.0104$ by multiple unpaired t-tests with Welch correction. (F) Quantification of multinucleated cells from an asynchronous population of HeLa FRT iGFP-gamma-actin expressing cells treated as indicated. $N = 3$ for all conditions; $n = 690$ cells scored for 'Control siRNA'; $n = 640$ cells for 'Gamma siRNA -dox'; $n = 621$ cells for 'Gamma siRNA +dox'. ** $p = 0.0066$ by a parametric student's t-test. (G) Western blot of cell lysates prepared from stable HeLa FRT iGFP-beta-actin cells treated as indicated. (H) Western blot of cell lysates prepared from stable HeLa FRT iGFP-gamma-actin cells treated as indicated. (I) Micrographs of mitotic and cytokinetic iGFP-beta-actin and iGFP-gamma-actin expressing HeLa FRT cells depleted of the corresponding endogenous actin isoform. Scale bar represents 10 μm . (J) Micrographs of iGFP-beta-actin expressing cells co-stained with vinculin, showing colocalization of iGFP-beta-actin with focal adhesions. iGFP-beta-actin is also visualized in focal adhesion-associated stress fibers and on membrane ruffles that are vinculin-negative. Scale bars represent 5 μm for both whole cell and magnified images. Cells were depleted of endogenous beta actin. (K) Micrographs of HeLa cells co-stained for beta-actin and vinculin, showing colocalization of beta-actin with focal adhesions. Beta-actin is also visualized in focal adhesion-associated stress fibers and on membrane ruffles that are vinculin-negative. Scale bars represent 5 μm for both whole cell and magnified images. Cells were depleted of endogenous beta actin. (L) Micrographs of iGFP-gamma-actin expressing cells co-stained with vinculin, showing colocalization of iGFP-gamma-actin with a subset of focal adhesions. iGFP-gamma-actin is also visualized on membrane ruffles that are vinculin-negative. Scale bars represent 5 μm for both whole cell and magnified images. Cells were depleted of endogenous gamma actin. (M) Micrographs of iGFP-gamma-actin expressing cells co-stained with antibody recognizing beta-actin, showing their distinct localization patterns on stress fibers. Scale bars represent 5 μm for both whole cell and magnified images. Cells were depleted of endogenous gamma actin.

(N) Representative ψ stick maps on SFs from measurements in live cells expressing the indicated G-actin fusions, with mean ψ values indicated. ψ stick maps for A42 and A47 are from nuclear F-actin. The selected images correspond to median ψ values of the respective distributions.

(O) Representative images of U2OS cells expressing the indicated reporters for assessing the contribution of linkers and shortened GFPs to their localization to specific actin populations. Expression is driven by a CMV_{trunc} promoter: the widely used full-strength CMV leads systematically to aggregation (leftmost panel). The absence of linkers and the proximity of GFP to the N-terminus of G-actin do not compromise binding to F-actin but result in lower enrichment of the reporters in myosin-II containing actin pools. G-actin-based reporters localize both to SFs and to mitochondria: two different z-planes in the same cell (A5) show A5 on SFs (left plane) and mitochondria (right plane). Fusions with tetracysteine peptides localized also to nuclear F-actin (A41).

Figure S5. Polarimetry measurements of actin filament organization in live dividing fission yeast expressing selected reporters, Related to Figure 5.

(A) Time-lapse maximum intensity projection images of fission yeast cells co-expressing the tubulin marker mCherry-Atb2 and selected actin organization reporters fused to msfGFP. The time interval between frames corresponds to 6 minutes. Scale bar, 4 μm .

(B) Maximum intensity projection images of fission yeast cells expressing the corresponding actin reporter; scale bar, 4 μm . On the right hand of each panel, a magnified dividing cell is shown to observe details of the actin structures (patches, cables, ring) decorated by the actin reporter. Green, blue and magenta arrowheads point to a patch, cable and ring, respectively. Scale bar, 2 μm .

(C) Quantification of actin cables per cell detected in the fission yeast strains expressing the corresponding actin reporter. Scatter plots show means \pm SD. 30 cells were analyzed for each strain. The mean number of cables per cell for each strain are, from left to right: 2.6, 2.1, 1.0, 0.3, 0.4, 0.3, 4.4 and 4.0.

(D) Quantification of actin patches per cell detected in the fission yeast strains expressing the corresponding actin reporter. Scatter plots show means \pm SD. 30 cells were analyzed for each strain. The mean number of patches per cell for each strain are, from left to right: 17.4, 17.5, 19.0, 15.9, 12.6, 8.0, 16.7 and 14.2.

(E-F) Polar histograms of ρ value distributions in the cytokinetic ring of fission yeast expressing Af7 (E) or L22 (F). ρ values are represented with respect to the ring axis: considering that Af7 and L22 dipoles are parallel to actin filaments, the more parallel mean actin filament orientations are to the ring axis, the closer the angle values are to 0° . Means \pm SD are shown. The number of cells is as in Fig.5G.

(G) Mean actin filament alignment (ψ angle) in the cytokinetic ring of fission yeast expressing Af7 (magenta) or L22 (green) as a function of the constricting ring diameter.

Figure S6. Polarimetry measurements of actin filament organization in live elongating *C. elegans* embryos expressing selected reporters, Related to Figure 6.

(A) Schematic of a *C. elegans* gravid adult worm showing the ex-utero development of embryos (top) and an overview of embryonic elongation (bottom). The length of the embryo is used for staging: 2-fold (2F) stage means 2-fold increase in length from the beginning of elongation. Representative stages are shown; anterior is to the left and dorsal is up.

(B) Schematic of the transgene design. The *dpy-7* promoter drives expression of the actin organization reporters in epidermal cells.

(C) Summed intensity images of the respective polarimetry stacks shown in Fig.6 E, G, I. For all panels, anterior is to the left and dorsal is up.

(D-G) Representative ρ (middle) and ψ (right) stick maps in >2-fold stage embryos expressing L22 (D) or L45 (F). The top images are summed intensity images of the respective polarimetry stacks. Insets show zoom-ins of selected ROIs (white outlined boxes). Mean ρ and ψ values are shown for each ROI.

(E), (G), Polar histograms of ρ value distributions in DV and seam cells in >2-fold stage embryos expressing L22 (E) or L45 (G). ρ values are represented with respect to the DV/seam boundary: considering that L22 dipoles are parallel to actin filaments and that L45 dipoles are perpendicular to actin filaments, the more perpendicular mean actin filament orientations are to the boundary, the closer the angle values are to 90° (for L22) or to 0° (for L45) and the narrower the respective distributions. Means \pm SD are shown. The number of embryos is as in Fig.6C. For all panels, anterior is to the left and dorsal is up.

Figure S7. Functional characterization of actin organization reporters in *Drosophila*, Related to Figure 7.

(A) Polar histogram of ρ value distributions in the actomyosin ring of a cellularizing *Drosophila* embryo expressing Af7. ρ values are represented with respect to the ring contour: considering that Af7 is parallel to actin filaments, the more parallel mean actin filament orientations are to the ring contour, the closer the angle values are to 0° . Mean \pm SD is shown.

(B) Effect of the expression of selected actin organization reporters on *Drosophila* wing growth. The image on the left displays an adult *Drosophila* wing and highlights the landmark points used for measuring the long axis (L_L) and short axis (L_S) of the wing (see methods for details). The product $L_L \cdot L_S$ is utilized as a proxy for wing area. The accompanying graph shows box plots quantifying wing area for the shown genotypes. On each box, the central mark indicates the median, and the bottom and top edges of the box indicate the 25th and 75th percentiles, respectively. The whiskers extend to the most extreme data points not considered outliers, and the outliers are plotted individually using the '+' symbol. The table on the right shows the respective genotypes (see Key Resources Table for details): (1) serves as a positive control, (2) serves as a negative control for a perturbation resulting in reduced wing size (Insulin receptor dominant negative), (3) is a commonly used actin probe, and (4-7) represent the

organization reporters described in this study. The number of wings for each genotype are, from left to right: 33, 40, 21, 46, 36, 37, 43. The respective median values are 1.31, 0.71, 1.36, 1.21, 1.26, 1.40, 1.36. A two-sample t-test was applied to evaluate statistical differences between each genotype and the positive control; ns=not significant, $P>0.05$; * $P<0.05$, *** $P<0.001$, **** $P<0.0001$.

(C-D) Representative micrographs of phalloidin ("F-actin") stainings of *Drosophila* flight muscles expressing selected actin organization reporters ("GFP") as shown (see methods for details of genotypes). Expression was driven throughout flight muscle development (C), or transiently at the adult stage after muscle development (D). Insets show zoom-ins of selected sarcomeres (white outlined boxes). See also Figure 7.

Belyy, A., Merino, F., Sitsel, O., and Raunser, S. (2020). Structure of the Lifeact-F-actin complex. *PLoS Biol* 18, e3000925.

Keep, N.H., Winder, S.J., Moores, C.A., Walke, S., Norwood, F.L., and Kendrick-Jones, J. (1999). Crystal structure of the actin-binding region of utrophin reveals a head-to-tail dimer. *Structure* 7, 1539-1546.

Kumari, A., Kesarwani, S., Javoor, M.G., Vinothkumar, K.R., and Sirajuddin, M. (2020). Structural insights into actin filament recognition by commonly used cellular actin markers. *EMBO J* 39, e104006.

Lopata, A., Hughes, R., Tiede, C., Heissler, S.M., Sellers, J.R., Knight, P.J., Tomlinson, D., and Peckham, M. (2018). Affimer proteins for F-actin: novel affinity reagents that label F-actin in live and fixed cells. *Sci Rep* 8, 6572.

Tiede, C., Tang, A.A., Deacon, S.E., Mandal, U., Nettleship, J.E., Owen, R.L., George, S.E., Harrison, D.J., Owens, R.J., Tomlinson, D.C., *et al.* (2014). Adhiron: a stable and versatile peptide display scaffold for molecular recognition applications. *Protein Eng Des Sel* 27, 145-155.